Phenomenology of sterile neutrino oscillations at a neutrino factory

Ken-ichi Fuki

Department of Physics, Graduate School of Science,
Tokyo Metropolitan University,
1-1 Minami-Osawa, Hachioji, Tokyo 192-0397, Japan

A dissertation submitted to
Graduate School of Science, Tokyo Metropolitan University

September 2009

Acknowledgments

I am grateful to my supervisor, Professor Osamu Yasuda, for bringing me into neutrino physics, his many advices and useful discussions. I acknowledge Dr.Andrea Donini, Mr.Jacobo López-Pavón and Dr.Davide Meloni for many useful discussions through collaboration in research. I also acknowledge Professor H. Minakata for his advices.

Abstract

We investigate the sterile neutrino oscillations at a neutrino factory. First of all, we briefly review the standard three flavor neutrino oscillations. We next review the present status of four flavor neutrino oscillation. After these reviews, we study (3+1) sterile neutrino oscillations at a neutrino factory. We analyze it using the two setups including the backgrounds and the systematic errors: a neutrino factory with 50 GeV (20 GeV) stored muons with two detectors located at L=3000, 7500 km (L=4000, 7500km) from the source. At these neutrino factories, we study sensitivities to the active-sterile mixing angles θ_{24} and θ_{34} using ν_μ disappearance and ν_μ to ν_τ appearance channels. We find that these channels are sensitive to the mixing angles. Furthermore, we study sensitivities to θ_{13} and the active-sterile mixing angle θ_{14} using ν_e to ν_μ and ν_e to ν_τ appearance channels, and also to the combinations $U_{e4}U_{\mu 4}$ and $U_{e4}U_{\tau 4}$ which are relevant to the short baseline oscillation experiments using ν_e to ν_μ and ν_e to ν_τ appearance channels. We find that the 50 GeV (20 GeV) set up can constrain $\sin^2 2\theta_{13} \leq 7 \times 10^{-5} (2 \times 10^{-4})$; $\theta_{34} \leq 12^\circ (14^\circ)$; $\theta_{24} \leq 7.5^\circ (8^\circ)$ at 90% CL. Our results hold for any value of $\Delta m^2_{SBL} \geq 0.1$ eV^2. We also invastigate the discovery potential to discriminate the four flavor neutrino schemes to the three flavor neutrino ones. Furthermore, the dependence of the performance of the ν_μ disappearance and the ν_μ to ν_τ appearance channels on the systematic errors are investigated. Finally, we investigate CP violation in four flavor neutrinos and find that the ν_μ to ν_τ appearance channel is useful.

Contents

Chapter 1

Introduction

The standard model describes the results of almost the experiments for elementary particles. However, the standard model has the problems such as origin of the mass hierarchy of the elementary particles, many free parameters. On the other hand, neutrino oscillations have been observed at Super Kamiokande and other experiments since 1990's. Neutrino oscillations occur if neutrinos have masses and mixings. By contrast, in the standard model neutrinos are massless. Therefore, neutrino oscillations will give us a hint of physics beyond the standard model.

From the combined results from LEP experiments (the ALEPH, DELPHI, L3, and OPAL experiments) [1, 2], we know that only three family (flavor) of neutrinos interact with the Z boson. Two mass square differences and two mixing angles in the framework of three family neutrinos are presently determined; $\Delta m^2_{\rm sol} \simeq 7.7 \times 10^{-5}$ eV^2, $\sin^2\theta_{12} \simeq 0.30 - 0.31$ [3, 4], and from the atmospheric neutrino experiments $|\Delta m^2_{\rm atm}| \simeq 2.4 \times 10^{-3}$ eV^2, $\sin^2 2\theta_{23} \simeq 0.47 - 0.50$ [3, 4]. As for θ_{13}, the reactor data [5, 6, 7] and three-flavor global analysis of the experimental data give an upper bound [1] To determine the remaining parameters, θ_{13} and δ in three flavor neutrino oscillations, long baseline experiments with intense neutrino beams have been proposed [11, 12, 13, 14, 15, 16, 17]. As in the case of the B factories [18, 19], these precision measurements will allow us to look for deviation from the standard three flavor oscillations scenario. Possible scenarios for such deviations include non-standard interactions which affects the neutrino productions and detections [20], those which modify the neutrino propagations [21, 22], light sterile neutrinos [23], unitarity violation due to the effect of heavy fermions [24, 25]. These scenarios in general break unitarity of the PMNS matrix. As in the B physics, test of unitarity is one of the important problems which should be investigated in the future long baseline experiments (see ref. [26] for a review). Among the proposed long baseline experiments with high intense neutrino beams, a Neutrino Factory [16], which uses a muon storage ring to produce neutrino beams from muon decays, is expected to have excellent sensitivity to θ_{13} and δ.

We can search for non-standard interactions or (and) new particles which are not included in the standard model at a Neutrino Factory. The mixing between active and sterile neutrinos is one of the possibilities. Four neutrino mass schemes have attracted much attention since the announcement by the LSND group on evidence for neutrinos

[1] In refs. [8, 4, 9, 10], a global analysis of the neutrino oscillation data has been shown, in which a non-vanishing value for θ_{13} is found. This result, however, is compatible with $\theta_{13} = 0$ at less than 2σ, and as such it cannot be taken as conclusive evidence for $\theta_{13} \neq 0$ yet.

$\bar{\nu}_\mu \to \bar{\nu}_e$ with a mass squared difference $\Delta m^2 \sim \mathcal{O}(1)$ eV^2 [27, 28, 29]. The mass spectra can be classified into two schemes; (3+1) scheme or (2+2) scheme. Because the mass squared difference suggested by the LSND result is much larger than those for the solar and atmospheric neutrino oscillations, in order to explain all these data in terms of neutrino oscillations, it is necessary to introduce *at least* a fourth light neutrino state. From the LEP data, which indicate that the number of weakly interacting light neutrinos is three, the fourth state has to be a sterile neutrino which is a gauge singlet fermion. For this reason, the LSND signal could be considered as an evidence for the existence of a sterile neutrino. Recently the MiniBooNE experiment [30] gave a negative result for neutrino oscillations with the mass squared difference $\Delta m^2 \sim O(1)$ eV^2 which was suggested by the LSND data, and it has become difficult for four neutrino models to explain the LSND data. The so-called (3+2)-scheme with two sterile neutrinos has also been proposed [38] to account for LSND, but also in this case, tension with the disappearance experiments remains, as long as we take into account the LSND data. Adding a third sterile neutrino does not seem to help [39], and in general global analyses seem to indicate that sterile neutrinos alone are not enough to account for all the data in terms of neutrino oscillations. Models with sterile neutrinos and exotic physics have been therefore proposed [42, 43, 44, 45, 46].

The efforts to account for all the data including the LSND in terms of neutrino oscillations have been unsuccessful. However sterile neutrino scenarios which satisfy all the experimental constraints *except* LSND are still possible. Sterile neutrinos with masses at the eV energy scale can participate in the seesaw mechanism to introduce neutrino masses [47] and can also aid in heavy element nucleosynthesis in supernovae [48]. Furthermore, sterile neutrinos can play a role of origin of baryogenesis [49] or/and dark matter etc (see [50]). Light singlet fermions are indeed present in the low-energy spectrum of many theories and models including them represent, for example, phenomenologically natural frameworks to break three family unitarity.

We have extended the analysis of a sterile neutrino oscillation at OPERA [51] to the case of a Neutrino Factory experiment. We have first of all extended the analytic computation of the oscillation probabilities for the $(3+1)$-model at long baseline experiments in matter using the formalism by Kimura-Takamura-Yokomakura (KTY) [52, 53]. Approximated formula in powers of θ_{13}, of the deviations from maximality of θ_{23} ($\delta\theta_{23}$) and of the active-sterile mixing angles, θ_{i4}, have been obtained. On the basis of this analysis, we have found that the greatest sensitivity to the active-sterile mixing angles is achieved using the $\nu_\mu \to \nu_\mu$ and $\nu_\mu \to \nu_\tau$ channels (as it was noticed, for example, in refs. [54, 55] and refs. therein). To take full advantage of these signals, detectors capable of both ν_μ and ν_τ identification are needed. In our numerical analysis we have, thus, assumed a detector of the Hybrid-MIND type [56]: a 50 kton magnetized iron calorimeter next to a 4 kton Emulsion Cloud Chamber with magnetized iron plates. This detector has a greater efficiency to $\nu_\mu \to \nu_\tau$ than the standard OPERA-type ECC, with lead plates acting as target.

We have then extensively analyzed the physics reach of a 50 GeV Neutrino Factory which has 2×10^{20} useful muon decays per year aimed at two detectors of the Hybrid-MIND type located at $L = 3000$ km and $L = 7500$ km from the source, with both polarities running for 4 years each. As a consistency check, we have also studied the case of a 20 GeV Neutrino Factory which has 5×10^{20} useful muon decays per year aimed at the same two detectors of the Hybrid-MIND type located at $L = 4000$ km and $L = 7500$ km,

again with both polarities running for 4 years each. The latter option was the scenario which was suggested in the *International Scoping Study for a future Neutrino Factory and Super-Beam facility* [26].

Four signals have been considered: the "standard" Neutrino Factory channels, the golden channel $\nu_e \to \nu_\mu$ [57] and the silver channel $\nu_e \to \nu_\tau$ [58]; the ν_μ disappearance channel; and the novel signal $\nu_\mu \to \nu_\tau$, that will be named as the discovery channel due to its high-sensitivity to new physics signals in neutrino oscillations [59]. Using the first two channels at the 50 GeV Neutrino Factory, we can extend the three-family θ_{13}-sensitivity plots to the four-family $(\theta_{13}, \theta_{14})$-plane, putting a stringent upper bound on the four-family θ_{13} mixing angle, $\sin^2 2\theta_{13} \lesssim \mathcal{O}(10^{-4})$. Using the combination of the ν_μ disappearance channel and of the discovery channel $\nu_\mu \to \nu_\tau$ at the 50 GeV Neutrino Factory, we are able to constrain the active-sterile mixing angles θ_{34} and θ_{24}, $|\theta_{34}| \lesssim 12^\circ$ and $|\theta_{24}| \lesssim 7.5^\circ$. We have found that the combination of the shortest baseline data with the longest baseline ones significantly improves the sensitivity in both planes, $(\theta_{13}, \theta_{14})$ and $(\theta_{24}, \theta_{34})$.

We have, then, compared our results for the 50 GeV Neutrino Factory with those that can be obtained at the 20 GeV ISS-inspired one, finding that the former setup has a far greater potential than the the latter for sterile neutrino searches, due to the larger τ statistics that can be collected using higher energy muons.

This thesis is organized as follows. In chapter 2.1 the features of neutrinos in the standard model are briefly summarized. In chapter 2.2 neutrino masses and the leptonic mixing matrix are introduced. Theory of neutrino oscillations are then briefly summarized. Recent experimental status of three flavor neutrino oscillations are also summarized in this chapter. In chapter 3 recent status of four flavor neutrino oscillations are summarized. In chapter 4 sensitivity limits of the four family neutrinos, discovery potential to discriminate the four flavor neutrino schemes from the three flavor ones and the dependence of the performance of the ν_μ disappearance and the ν_μ to ν_τ appearance channels on the systematic errors at a neutrino factory are presented. Furthermore, we investigate CP violation in four flavor neutrinos. Finally, we conclude in chapter 5.

We use natural system of units in which each of the reduced Plank constant $\hbar = h/2\pi$ and speed of light c are taken as unity in this thesis.

Chapter 2

Standard scenario of neutrino oscillations

2.1 Neutrinos in the standard model

The standard model describes the strong, weak and electromagnetic interactions of the elementary particles. The standard model is described by the gauge theory based on $\mathrm{SU(3)}_C \times \mathrm{SU(2)}_L \times \mathrm{U(1)}_Y$ gauge symmetry. The left handed quark fields $Q_L^i = (1-\gamma_5)Q^i/2 = (\ u_L^j,\ \ d_L^j\ )$ and left handed lepton fields $L_L^i = (1-\gamma_5)L^i/2 = (\ \nu_L^i,\ \ l_L^i\ )$ are introduced as doublets of $\mathrm{SU(2)}_L$ gauge symmetry in the standard model, on the other hand, the right handed quark fields $u_R^i = (1+\gamma_5)u^i/2,\ d_R^i = (1+\gamma_5)d^i/2$ and lepton fields $l_R^i = (1+\gamma_5)l^i/2$ are introduced as singlets of $\mathrm{SU(2)}_L$ gauge symmetry. The suffixes $i,\ j = 1,\ 2,\ 3$ stand for the generation of quarks and leptons. Their charges and representations of the gauge symmetry are shown in the table 2.1. The gauge symmetry allows the following interactions called Yukawa interaction in the Lagrangian:

$$\mathcal{L} = -y_{ij}^{(l)} \bar{L}_L^i \Phi l_R^j - y_{ij}^{(u)} \bar{Q}_L^i \Phi u_R^j - y_{ij}^{(d)} \bar{Q}_L^i \tilde{\Phi} d_R^j + h.c., \tag{2.1}$$

where $y_{ij}^{(l,u,d)}$ is the Yukawa coupling constant. $\Phi = (\ \phi^{(+)},\ \ \phi^{(0)}\ )$ is the Higgs doublet field which is doublet of $\mathrm{SU(2)}_L$ and $\tilde{\Phi} = i\sigma_2\Phi^*$ is defined by using the Pauli matrix σ_2. The particles are massless because of the gauge symmetries. The masses of the particles can be generated by the Higgs mechanism which spontaneously breaks the gauge symmetries, $\mathrm{SU(2)}_L \times U(1)_Y$, down to the gauge symmetry, $\mathrm{U(1)}_{em}$. As potential terms of the Higgs doublet field in Hamiltonian we can take the form,

$$\begin{aligned} V(\Phi) &= -\mu^2 \Phi^\dagger \Phi + \lambda \left(\Phi^\dagger \Phi\right)^2 \\ &= \lambda \left(\Phi^\dagger \Phi - \frac{v^2}{2}\right)^2 - \frac{\mu^4}{4\lambda}, \end{aligned} \tag{2.2}$$

where μ and λ are real number. $v = \mu/\sqrt{\lambda}$ is introduced to denote the minimum point, which is vacuum, of the potential $V(\Phi)$. Taking a suitable $\mathrm{SU(2)}_L$ phase convention, the vacuum expectation value of the Higgs field is as follows:

$$\Phi = \begin{pmatrix} 0 \\ v/\sqrt{2} \end{pmatrix}. \tag{2.3}$$

	$\mathrm{SU}(3)_C$	$\mathrm{SU}(2)_L$	$\mathrm{U}(1)_Y$
L_L^i	**1**	**2**	$-\frac{1}{2}$
l_R^i	**1**	**1**	-1
Q_L^i	**3**	**2**	$\frac{1}{6}$
u_R^i	**3**	**1**	$\frac{2}{3}$
d_R^i	**3**	**1**	$-\frac{1}{3}$
Φ	**1**	**2**	$\frac{1}{2}$

Table 2.1: The charges and representations of the gauge symmetry of the quark fields, the lepton fields and the Higgs doublet field $\Phi = (\phi^{(+)}, \phi^{(0)})$ in the standard model.

We can give the parametrization of the Higgs filed in this vacuum as follows:

$$\Phi = \frac{1}{\sqrt{2}} \begin{pmatrix} i\chi_1 + \chi_2 \\ v + \phi - i\chi_3 \end{pmatrix}, \tag{2.4}$$

where ϕ, χ_1, χ_2 and χ_3 are hermitian fields. The Yukawa interaction terms eq. (2.1) after the breakdown of $\mathrm{SU}(2)_L \times U(1)_Y$ symmetry are then as follows:

$$\begin{aligned} \mathcal{L} &= -\frac{1}{\sqrt{2}} y_{ij}^{(l)} \begin{pmatrix} \bar{\nu}_L^i, & \bar{l}_L^j \end{pmatrix} \begin{pmatrix} i\chi_1 + \chi_2 \\ v + \phi - i\chi_3 \end{pmatrix} l_R^j - \frac{1}{\sqrt{2}} y_{ij}^{(u)} \begin{pmatrix} \bar{u}_L^i, & \bar{d}_L^i \end{pmatrix} \begin{pmatrix} i\chi_1 + \chi_2 \\ v + \phi - i\chi_3 \end{pmatrix} u_R^j \\ &\quad -\frac{1}{\sqrt{2}} y_{ij}^{(d)} \begin{pmatrix} \bar{u}_L^i, & \bar{d}_L^i \end{pmatrix} \begin{pmatrix} v + \phi + i\chi_3 \\ -i\chi_1 + \chi_2 \end{pmatrix} d_R^j + h.c., \\ &= -m_{ij}^{(l)} \bar{l}_L^i l_R^j - m_{ij}^{(u)} \bar{u}_L^i u_R^j - m_{ij}^{(d)} \bar{d}_L^i d_R^j + \ldots, \end{aligned} \tag{2.5}$$

where $m_{ij}^{(l)} = v y_{ij}^{(l)}/\sqrt{2}$, $m_{ij}^{(u)} = v y_{ij}^{(u)}/\sqrt{2}$ and $m_{ij}^{(l,u,d)} = v y_{ij}^{(l,u,d)}/\sqrt{2}$ are mass matrix elements of the charged leptons (such as a electron, a muon and a tauon), up-sector quarks (such as a up, charm and top quarks) and down-sector quarks (such as a down, strange and bottom quarks), respectively. Note that the neutrinos are massless since there does not exist a right handed neutrino.

If the mass matrices $m_{ij}^{(l,u,d)}$ are diagonalized, the weak interaction terms in quark sector become the following:

$$\begin{aligned} \mathcal{L} &= \frac{g}{\sqrt{2}} W_\mu^+ U_{ij}^{\mathrm{CKM}} \bar{u}_L^i \gamma_\mu d_L^j \\ &\quad + \frac{2g}{\sqrt{2}\cos\theta_W} Z_\mu \left\{ \bar{d}^i \gamma^\mu \left(\frac{1-\gamma_5}{2} - 2Q_i \sin^2\theta_W \right) d^i - \bar{u}^i \left(\frac{1-\gamma_5}{2} + 2Q_i \sin^2\theta_W \right) u^i \right\} \\ &\quad + h.c., \end{aligned} \tag{2.6}$$

where U_{ij}^{CKM} which is called Cabibbo-Kobayashi-Maskawa (CKM) mixing matrix generally give rise to flavor changing processes and CP violation for quarks.

On the other hand, the weak interaction terms in lepton sector become the following:

$$\begin{aligned} \mathcal{L} &= \frac{g}{\sqrt{2}} W_\mu^+ \bar{\nu}_L^i \gamma_\mu l_L^i \\ &\quad + \frac{2g}{\sqrt{2}\cos\theta_W} Z_\mu \left\{ \bar{l}^i \gamma^\mu \left(\frac{1-\gamma_5}{2} - 2Q_i \sin^2\theta_W \right) l^i - \bar{\nu}^i \left(\frac{1-\gamma_5}{2} + 2Q_i \sin^2\theta_W \right) \nu^i \right\} \\ &\quad + h.c., \end{aligned} \tag{2.7}$$

where $\nu_i = \nu_e,\ \nu_\mu$ or ν_τ and $l_i = e,\ \mu$ or τ. Note that there is no mixing matrix in the lepton sector which is an analogue of the CKM mixing matrix because fields of neutrinos can be redefined such as

$$\nu_i = U_{ij}\nu_j. \tag{2.8}$$

Therefore, weak interaction conserve the lepton number and CP invariance in the lepton sector unlike the quark sector.

2.2 Massive neutrino and neutrino oscillations

2.2.1 Neutrino masses and formulation of oscillation probabilities

Recent neutrino oscillation experiments ensure that there exist neutrino masses. However, neutrinos in the standard model are massless. Thus, neutrino masses should be introduced to the standard model. In the filed theory there are two possible neutrino mass terms. One of these is the Dirac mass term. The other is the Majorana mass term. In the case of the Dirac mass term, at least, a right-handed neutrino ν_R which is a new particle must be introduced to the standard model and then the neutrino masses can be introduced as follows:

$$\mathcal{L}_{\nu\text{mass}} = -\bar{\nu}_R m_D \nu_L + h.c. \tag{2.9}$$

where $\nu_L = (\nu_{Le}, \nu_{L\mu}, \nu_{L\tau})^T$ and $\nu_R = (\nu_{Re}, \nu_{R\mu}, \nu_{R\tau})^T$. In contrast, the Majorana mass term consist of the left-handed neutrinos:

$$\mathcal{L}_{\nu\text{mass}} = -\bar{\nu}^c_L m_M \nu_L + h.c., \tag{2.10}$$

where $\nu^c = i\gamma_2\nu^*$ are the charge-conjugated fields of neutrinos and $\nu^c_L = (\nu_L)^c = \frac{1+\gamma_5}{2}\nu^c$ have right-handed chirality. However, these Majorana mass terms are forbidden by $SU(2)_L \times U(1)_Y$ gauge symmetry in the standard model. In order to consist the Majorana mass terms, many models had been proposed. One of these models is the seesaw model [60] and another is Zee model [61]. These models introduce a new particle, a right-handed neutrino or a charged Higgs particle. Therefore, there will exits a new particle because of neutrino masses.

Introducing mass terms of neutrinos, there appears the lepton-mixing matrix, which is called Pontecorvo-Maki-Nakagawa-Sakata matrix (PMNS matrix), and is an analogue of the CKM matrix of quarks. In the case that neutrinos have the Dirac mass term (Dirac neutrinos), taking a basis in which the charged lepton mass term is diagonal, we further diagonalized the neutrino mass term, eq. (2.9), as follows:

$$\nu^\alpha_L = Q_{\alpha i}\nu^i_L, \tag{2.11}$$
$$\nu^\alpha_R = V_{\alpha i}\nu^i_R, \tag{2.12}$$

$$\mathcal{L} = -\bar{\nu}^i_R V^*_{\alpha i}(m_D)_{\alpha\beta}Q_{\beta j}\nu^j_L + h.c. \tag{2.13}$$
$$= -\bar{\nu}^i_R(m_D)_i\nu^i_L + h.c., \tag{2.14}$$

thus,

$$V^\dagger m_D Q = m_{diag}, \tag{2.15}$$

where $\nu_{L(R)}^{i(j)}$ are the field of neutrinos in the mass basis (i,j=1, 2, 3). Using the field in the mass basis, we can rewrite the interaction Lagrangian, eq. (2.7), as follows:

$$\mathcal{L} = \frac{g}{\sqrt{2}} W_\mu^+ (\ \bar{\nu}_{1L},\ \ \bar{\nu}_{2L},\ \ \bar{\nu}_{3L}\ ) U^\dagger \gamma_\mu \begin{pmatrix} e_L \\ \mu_L \\ \tau_L \end{pmatrix} + h.c., \tag{2.16}$$

where U is the PMNS matrix. In the standard parametrization [1], the PMNS matrix can be parametrized as follows:

$$U = \begin{pmatrix} c_{12}c_{13} & s_{12}c_{13} & s_{13}e^{-i\delta} \\ -s_{12}c_{23} - c_{12}s_{23}s_{13}e^{-i\delta} & c_{12}c_{23} - s_{12}s_{23}s_{13}e^{i\delta} & s_{23}c_{13} \\ s_{12}s_{23} - c_{12}c_{23}s_{13}e^{i\delta} & -c_{12}s_{23} - s_{12}c_{23}s_{13} & c_{23c_{13}} \end{pmatrix}, \tag{2.17}$$

where c_{ij} (s_{ij}) $(i,\ j$=1, 2, 3) stand for $\cos\theta_{ij}$ $(\sin\theta_{ij})$. In the case that the CP phase δ is not zero, the interaction term, eq. (2.16), violate CP invariance. In the case that neutrinos have the Majorana mass term (Majorana neutrino), we similarly obtain the PMNS matrix. For Majorana neutrinos, the PMNS matrix can be as follows:

$$U = \begin{pmatrix} c_{12}c_{13} & s_{12}c_{13} & s_{13}e^{-i\delta} \\ -s_{12}c_{23} - c_{12}s_{23}s_{13}e^{-i\delta} & c_{12}c_{23} - s_{12}s_{23}s_{13}e^{i\delta} & s_{23}c_{13} \\ s_{12}s_{23} - c_{12}c_{23}s_{13}e^{i\delta} & -c_{12}s_{23} - s_{12}c_{23}s_{13} & c_{23c_{13}} \end{pmatrix} \begin{pmatrix} e^{iD_1/2} & 0 & 0 \\ 0 & e^{iD_2/2} & 0 \\ 0 & 0 & 1 \end{pmatrix}, \tag{2.18}$$

where the second matrix of the right hand side appears because degrees of freedom of the right handed neutrinos do not exit. That is, there exits the two extra CP phases D_1 and D_2 in the 3 flavor Majorana neutrinos.

Massive neutrinos can give rise to the phenomenon of neutrino oscillations. Next, we will perform the analytic formula of the neutrino-flavor-transition probabilities. The time evolution of the neutrinos in the flavor eigenbasis is as follows:

$$i\frac{d}{dt}\begin{pmatrix} \nu_e \\ \nu_\mu \\ \nu_\tau \end{pmatrix} = \left[U\mathcal{E}U^{-1}\right] \begin{pmatrix} \nu_e \\ \nu_\mu \\ \nu_\tau \end{pmatrix}, \tag{2.19}$$

where we have assumed that the neutrino masses are much smaller than the absolute value of neutrino momenta, $m_{1,2,3} \ll |\mathbf{p}|$ and then $\mathcal{E}$ is

$$\mathcal{E} = \mathrm{diag}\left[0,\ \frac{\Delta m_{21}^2}{2E},\ \frac{\Delta m_{31}^2}{2E}\right] \tag{2.20}$$

and $\Delta m_{21(31)}^2 = m_{2(3)}^2 - m_1^2$. U is PMNS matrix, eq. (2.17). If we observe the neutrino at a distance L from the source, we can derive the transition probabilities of neutrino flavors in vacuum from eq. (2.19):

$$\begin{aligned} P(\nu_\alpha \to \nu_\beta) &= \left| \sum_{j,k} U_{\alpha j} \exp\left(-i\frac{\Delta m_{jk}^2}{2E}L\right) U_{\beta k}^* \right|^2 \\ &= \delta_{\alpha\beta} - 4\sum_{j>k} \mathrm{Re}\left[U_{\alpha j}U_{\beta j}^* U_{\alpha k}^* U_{\beta k}\right] \sin^2\left(\frac{\Delta m_{jk}^2}{4E}L\right) \\ &\quad - 2\sum_{j>k} \mathrm{Im}\left[U_{\alpha j}U_{\beta j}^* U_{\alpha k}^* U_{\beta k}\right] \sin\left(\frac{\Delta m_{jk}^2}{2E}L\right), \end{aligned} \tag{2.21}$$

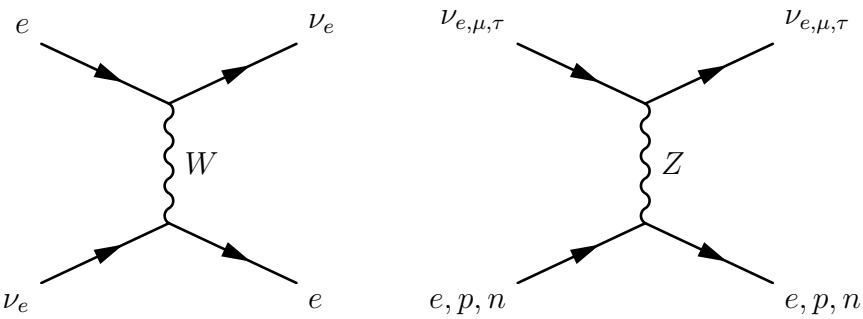

Figure 2.1: Scattering for ν_e, ν_μ and ν_τ in matter of which the Earth or the Sun is composed. e, p and n stand for electron, proton and neutron, respectively.

where we have assumed that speed of neutrinos are nearly equal to speed of light.

Passing in matter, neutrinos interact with matter. Figure 2.1 shows the scattering processes of neutrinos in the matter of which the Earth or the Sun is composed. In this case, the time evolution of the neutrinos in the flavor eigen-basis is as follows:

$$i\frac{d}{dt}\begin{pmatrix}\nu_e\\ \nu_\mu\\ \nu_\tau\end{pmatrix} = \left[U\mathcal{E}U^{-1} + \mathcal{A}(t)\right]\begin{pmatrix}\nu_e\\ \nu_\mu\\ \nu_\tau\end{pmatrix}, \tag{2.22}$$

where

$$\mathcal{A}(t) = \sqrt{2}G_F\mathrm{diag}(\ n_e(t),\ \ 0,\ \ 0\ ) \tag{2.23}$$

is the potential by the interaction with matter, G_F is Fermi constant and $n_e(t)$ is electron density in matter. The effective Hamiltonian $U\mathcal{E}U^{-1} + \mathcal{A}(t)$ can be diagonalized using a unitary matrix $\tilde{U}(t)$:

$$\tilde{U}(t)\tilde{\mathcal{E}}(t)\tilde{U}^{-1}(t) = U\mathcal{E}U^{-1} + \mathcal{A}(t), \tag{2.24}$$

where

$$\tilde{\mathcal{E}}(t) = \mathrm{diag}(\ \tilde{E}_1(t),\ \ \tilde{E}_2(t),\ \ \tilde{E}_3(t)\ ) \tag{2.25}$$

and $\tilde{E}_{1,2,3}(t)$ is the eigenvalue of $U\mathcal{E}U^{-1} + \mathcal{A}(t)$. Using eq. (2.24), We can derive the transition probabilities of neutrino flavors in matter:

$$\begin{aligned} P(\nu_\alpha \to \nu_\beta) &= \left|\sum_{j,k}\tilde{U}_{\alpha j}\exp\left(-i\tilde{E}_{ij}L\right)\tilde{U}^*_{\beta k}\right|^2 \\ &= \delta_{\alpha\beta} - 4\sum_{j>k}\mathrm{Re}\left[\tilde{U}_{\alpha j}\tilde{U}^*_{\beta j}\tilde{U}^*_{\alpha k}\tilde{U}_{\beta k}\right]\sin^2\left(\frac{\tilde{E}_{ij}}{2}L\right) \\ &\quad - 2\sum_{j>k}\mathrm{Im}\left[\tilde{U}_{\alpha j}\tilde{U}^*_{\beta j}\tilde{U}^*_{\alpha k}\tilde{U}_{\beta k}\right]\sin\left(\tilde{E}_{ij}L\right), \end{aligned} \tag{2.26}$$

where $\tilde{E}_{ij} = \tilde{E}_i - \tilde{E}_j$ and we assume that the electron density n_e is constant.

The formula of the transition probabilities (2.26) are complicated. For simplicity, we will consider the transition probabilities in two flavor neutrinos. In case of two flavor neutrinos, the transition probability, eq. (2.26), for $\nu_e \to \nu_\mu$ is as follows:

$$P(\nu_e \to \nu_\mu) = \sin^2 2\tilde{\theta}\sin^2\left(\frac{\Delta\tilde{m}^2}{4E}L\right), \tag{2.27}$$

where

$$\sin^2 2\tilde{\theta} = \frac{\sin 2\theta}{\sqrt{(2EA/\Delta m^2 - \cos 2\theta)^2 + \sin^2 2\theta}}, \quad (2.28)$$

$$\Delta\tilde{m}^2 = \sqrt{(2EA - \Delta m^2 \cos 2\theta)^2 + (\Delta m^2)^2 \sin^2 2\theta}, \quad (2.29)$$

$A = \sqrt{2} G_F n_e$ and $\Delta m^2 = m_2^2 - m_1^2$. The resonance occurs at $2EA/\Delta m^2 = \cos 2\theta$, i.e.,

$$n_{e\ (crit)} = \frac{\Delta m^2 \cos 2\theta}{2\sqrt{2} G_F E}. \quad (2.30)$$

For $n_e \gg n_{e\ (\mathrm{crit})}$, a mixing length in matter,

$$\tilde{L}_0 = \frac{4\pi E}{\Delta\tilde{m}^2} = \frac{4\pi E}{\Delta m^2} \frac{1}{\sqrt{(2EA/\Delta m^2 - \cos 2\theta)^2 + \sin^2 2\theta}}, \quad (2.31)$$

is shorter than a mixing length in vacuum, $L_0 = 4\pi E/\Delta m^2$. At $n_e = n_{e\ (\mathrm{crit})}$, mixing of two neutrinos is maximum, $\tilde{\theta} = \pi/4$.

2.2.2 Recent experimental status of the 3 flavor neutrino scenarios

KamLAND [72] is a an experiment with 1 kton of a liquid scintillator which detects $\bar{\nu}_e$ emitted by reactors located at distances 100-250 km using $\bar{\nu}_e + p \rightarrow e^+ + n$ reaction with a 1.8 MeV threshold. The detector can see both the positron and the 2.2 MeV γ ray from neutron capture on proton. The effect of oscillations is given by

$$P(\bar{\nu} \rightarrow \bar{\nu}) = 1 - \sin^2 2\theta_{12} \sin^2 \left(\frac{\Delta m^2_{21}}{4E} L \right) \quad (2.32)$$

up to minor corrections due to the earth matter effects and to the small θ_{13}. KamLAND spectral data (fig.2.2 [65]) give a 3σ indication for oscillation dips. The first one at $E_{\mathrm{vis}} = E_{\bar{\nu}_e} + m_e \approx 7$ MeV (where statistics is poor) and the second one at $E_{\mathrm{vis}} \approx 4$ MeV. Taking into account the average baseline $L \approx 180$ km, this second dip occurs at $L/E_{\bar{\nu}_e} \approx 45$ km/MeV. This means $\Delta m^2_{21} = 6\pi E_{\bar{\nu}_e}/L \approx 8 \times 10^{-5} \mathrm{eV}^2$.

The Sun shines thanks to nuclear fusion. Around the center of the Sun, energy and neutrinos are produced essentially thought the ^4He reaction:

$$4p + 2e \rightarrow {}^4He + 2\nu_e \quad (2.33)$$

The predicted ν_e spectrum at production is shown in figure 2.3 [64]. The reason of such a complex spectrum is that the overall reaction, eq. (2.33), proceeds in a sequence of the steps following different routes. The main routes give rise to five types of neutrinos [65]. *pp* neutrinos, generated in the first step $pp \rightarrow de^+\nu_e$, have a large and precisely predicted flux. However, their maximal energy is only $E \approx 2m_p - m_d - m_e = 0.42$ MeV, so that it is difficult to detect *pp* neutrinos. *pep* neutrinos, generated in $pep \rightarrow d\nu_e$, have a relatively small flux and low energy, $E \approx 2m_p + m_e - m_d = 1.445$ MeV, but are not totally negligible. Be neutrinos have a relatively well predicted, large flux and relatively high energy, $E \approx m_{^7Be} - m_{^7Li} - m_e \approx 0.863$ MeV. The *pep* and Be neutrinos are almost

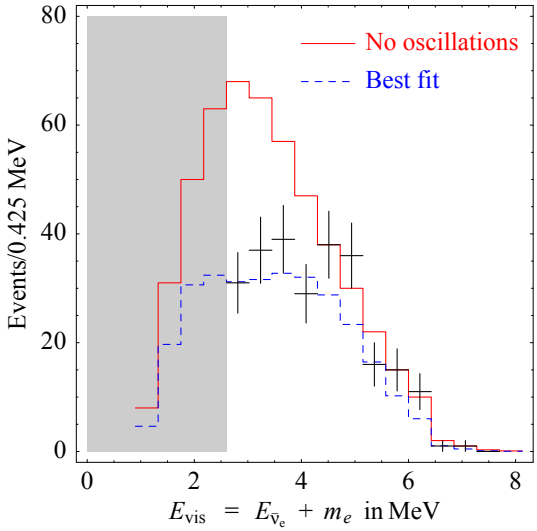

Figure 2.2: The $E_{vis} = E_{\bar{\nu}_e} + m_e$ energy spectrum measured by KamLAND [63].

monochromatic because these are generated by electrons colliding on heavy particles at temperatures $T \ll m_e$. B neutrinos constitute a small fraction of all solar neutrinos, but can have a relatively large energy, up to $E \leq ms_B - 2m_\alpha$. *hep* neutrinos have the highest energy, but have a very small flux.

Homestake is the first experiment which detected solar neutrinos and saw the first hint of the solar neutrino anomaly [66], using a radiochemical technique. Solar ν_e induces the reaction $\nu_e + {}^{37}Cl \rightarrow {}^{37}Ar + e$, producing the isotope ${}^{37}Ar$. Such isotopes were separated using their different chemical behaviors. Observing their later decays back to ${}^{37}Cl$ (the half-life time is 35 days) it was possible to count a few atoms in a tank of few hundred tons. The Cl reaction was employed because its cross section is precisely computable and its energy threshold, $E_{\nu_e} > 0.841$ MeV. The next radiochemical experiments, SAGE and GALLEX/GNU employed the reaction $\nu_e + {}^{71}Ga \rightarrow {}^{71}Ge + e$ which has a lower threshold, $E_{\nu_e} > 0.233$ MeV [67]. SuperKamiokande (SK) [68] is a 50 kton water Čerenkov detector. Solar neutrinos are detected via scattering on electrons $\nu_{e,\mu,\tau} + e \rightarrow \nu_{e,\mu,\tau} + e$. SK can measure the kinetic energy Te and the direction of the scattered electron. The dominant backgrounds to the solar neutrino signal are ${}^{222}Rn$ in the water, external γ rays and muon induced spallation products. As a consequence only data above the cut $T_e > 5.5$ MeV are used. SNO [69] is a water Čerenkov detector. The experiment employs 1 kton of heavy water (D_2O) instead of water (H_2O). By virtue of deuterons, SNO can observe not only the elastic scattering ($\nu_{e,\mu,\tau} + e \rightarrow \nu_{e,\mu,\tau} + e$), but also the charged current reaction ($\nu_e + d \rightarrow 2p + e$) which has an analysis threshold of ~ 5 MeV [70], and the neutral current reaction ($\nu_{e,\mu,\tau} + d \rightarrow \nu_{e,\mu,\tau} + n + p$) which has an energy threshold of 2.2 MeV [70]. The charged current events/the neutral current events discrimination was performed in different ways before (the first phase) and after (the second phase) adding salt to heavy water. After adding salt, SNO could statistically discriminate events from the pattern of photomultiplier-tube hits. NC events produce multiple γ ray and consequently a more isotropic Čerenkov light than the single e produced in the charged current events and the elastic scattering events. In the third phase, by adding ${}^3He$, SNO is able of tagging the neutral current events on an event-by-event basis by detecting neutron via the scattering

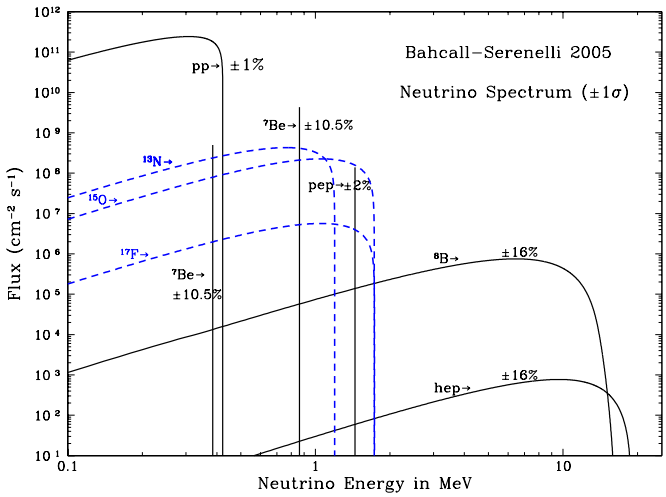

Figure 2.3: The predicted unoscillated spectrum of solar neutrinos [64] .

$n + {}^3He \ \rightarrow \ p + {}^3H$. Borexino [71] is a real time detector which consists of 300 ton of liquid scintillator for low energy, $E_\nu < 4.5$ MeV, solar neutrinos, with the specific goal of measuring the ^7Be neutrino flux from the Sun. Solar neutrinos are detected via scattering on electrons $\nu_{e,\mu,\tau} + e \ \rightarrow \ \nu_{e,\mu,\tau} + e$.

Fig. 2.4 illustrates how the determination of the leading solar oscillation parameters θ_{12} and Δm^2_{21} emerges from the complementarity of solar and reactor neutrinos [3]. From the global three-flavor analysis we find (1σ errors)

$$\sin^2 2\theta_{12} = 0.304^{+0.022}_{-0.016}, \ \Delta m^2_{21} = 7.65^{+0.23}_{-0.20} \times 10^5 \text{ eV}^2. \tag{2.34}$$

Atmosphere neutrino

Next, we will focus on θ_{23} and Δm^2_{31}. Atmospheric neutrinos are generated by collisions of primary cosmic rays. Primary cosmic rays hit the nuclei in the air in the upper part of the earth atmosphere and produce mostly pions. Then, the charged pions decay promptly generating muons and muon neutrinos $\pi^+ \ \rightarrow \ \mu^+\nu_\mu$, $\pi^- \ \rightarrow \ \mu^-\bar{\nu}_\mu$. Finally, the muons produced by the pion decays travel a distance $d \approx c\tau_\mu E_\mu/m_\mu \approx 6\text{km}E_\mu/$ GeV. All muons will decay $\mu^- \ \rightarrow \ e^-\bar{\nu}_e\nu_\mu$, $\mu^+ \ \rightarrow \ e^+\nu_e\bar{\nu}_\mu$. Thus, one would obtain a flux of ν_e and ν_μ in proportional to 2 : 1. SK can detect atmosphere neutrinos through the CC scattering on nucleons as in the case of solar neutrinos. SK can distinguish ν_μ from ν_e by shape of the Čerenkov rings but can not distinguish a neutrino from an anti-neutrino. Measuring the Čerenkov light, SK reconstructs the kinetic energy of a recoiled charged lepton T_l and the scattering angle $\theta_{l\nu}$. However, it is not sufficient to reconstruct the energy of a neutrino because the direction of a neutrino can not be measured. For this reason, their data are collected into big energy bins.

- Fully-contained electron or muon events: the scattered charged lepton is produced and stops inside the detector, so that its energy can be measured.
  - sub-GeV events ($E_l \ \lesssim \ 1.4$ GeV): the sub-GeV events are produced by neutrinos with a energy of about a GeV. The average opening angle between the

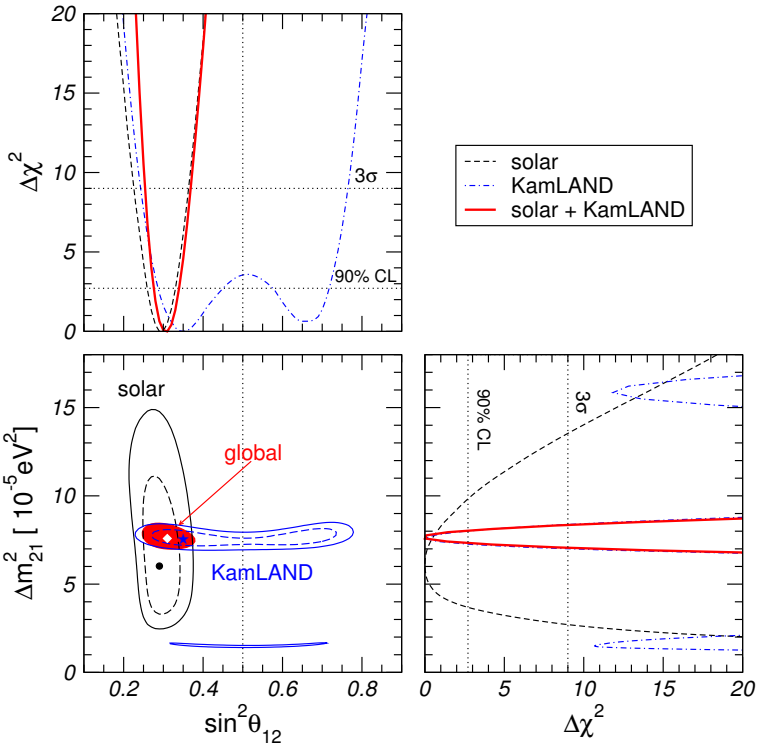

Figure 2.4: Determination of the leading solar oscillation parameters from the interplay of data from artificial and natural neutrino sources. It is shown χ^2-profiles and allowed regions at 90% and 99.73% CL (2 dof) for solar and KamLAND, as well as the 99.73% CL region for the combined analysis. The dot, star and diamond indicate the best fit points of solar data, KamLAND and global data, respectively. χ^2 is minimized with respect to Δm^2_{31}, θ_{23} and θ_{13}, including atmospheric, MINOS, K2K and CHOOZ data [3].

incoming neutrino and the detected charged lepton is $\theta_{l\nu} \sim 60°$. The upper panel of figure 2.5 shows the result of the sub-GeV events at SK.

– multi-GeV events ($E_l \gtrsim 1.4$ GeV): multi-GeV events are produced by neutrinos with a energy of few GeV. The average opening angle between the incoming neutrino and the detected charged lepton is $\theta_{l\nu} \sim 15°$. The middle panel of figure 2.5 shows the result of the multi-GeV events at SK. This figure shows that multi-GeV neutrinos begin to oscillate around the horizontal direction ($\cos\theta_\nu \sim 0$) at a path-length of about $L \sim 1000$km. Therefore, using acceptable neutrino energy of multi-GeV events $E_\nu \sim 3$ GeV, the typical value of the mass squared difference $\Delta m^2_{\rm atm} \sim E_\nu/L \sim 3 \times 10^{-3}$ eV^2.

- Partially contained muons: the muon is scattered inside the detector, but escapes from the detector, so that its energy can not measured. These events originate from neutrinos with a typical energy only slightly higher than those giving rise to multi-GeV muons. Therefore, those two classes of events can be conveniently grouped together. Using the both multi-GeV event and partially contained muon event data, we can find a neutrino anomaly even without relying our knowledge of atmosphere neutrino fluxes. While the zenith-angle distribution of muon events is clearly asymmetric the e-like events show no asymmetry. The flux of the up-ward

going muons is about one half of the flux of down-ward muons. Therefore, the data can be interpreted assuming that nothing happens to ν_e and that ν_μ oscillate into ν_τ. Neglecting the earth matter corrections, we have

$$\begin{aligned} P(\nu_e \to \nu_e) &= 1,\ P(\nu_e \to \nu_\mu) = 0,\ P(\nu_\mu \to \nu_e) = 0, \\ P(\nu_\mu \to \nu_\tau) &= 1 - \sin^2 2\theta_{atm} \sin^2 \left(\frac{\Delta m^2_{\rm atm}}{4E_\nu} L \right). \end{aligned} \tag{2.35}$$

Looking at the zenith-angle dependence we notice that down-ward going neutrinos are almost unaffected by oscillations, while up-ward going neutrinos feel almost averaged oscillations $P(\nu_\mu \to \nu_\tau) = 1 - \sin^2 2\theta_{atm}/2$. This must be equal to the up/down ratio $N_{up}/N_{down} \approx 0.5$, so that $\sin^2 2\theta_{atm} \approx 1$.

- Up-ward-going stopping muons: the scattered muon is produced in the rock below the detector and stops inside the detector. The typical energy of parent neutrinos is $E_\nu \sim 10$ GeV.

- Through-going up muons: the muon is scattered in the rock below the detector and crosses the detector without stopping. These events are produced by neutrinos with the typical energy $E_\nu \sim 10$ GeV $- 10$ TeV.

K2K and The Main Injector Neutrino Oscillation Search

An artificial long-baseline ν_μ pulsed beam was sent in the K2K experiment from KEK to the SK detector, located in Kamioka which is 250 km away from KEK. Since the beam is pulsed, SK can discriminate atmospheric neutrinos from the KEK neutrino beam, both detected using charged-current scattering on nucleons. The neutrino beam was produced by colliding a total of 9×10^{19} accelerated protons on a target. A magnetic field is used to collect and focus the resulting π^+, obtaining from their decays a 98% pure ν_μ beam with an average energy of $E_\nu \sim 1.3$ GeV. The baseline L and the energy E_ν have been chosen such that $\Delta m^2_{\rm atm} L/E_\nu \sim 1$ in order to sit around the first oscillation dip.

Another artificial long-baseline ν_μ pulsed beam has been sent in the MINOS experiment from the Neutrinos at the Main Injector facility (NuMI) at Fermi National Accelerator Laboratory to the near detector located 1 km away and the far one located 735 km away. A near detector, functionally identical to the far detector, allows to predict the non-oscillation rate. The both detectors consist of magnetized steel plates and the mass of the far detector is 5.4 kton. This allows to discriminate particles from anti-particles and to discriminate the neutral current scattering from the charged current one. The average energy of the ν_μ beam is $E_\nu \sim$ a few GeV and their data recorded between May 2005 and July 2007 correspond to a total of 3.36×10^{20} protons on target (POT).

Figure 2.6 illustrates how the determination of the leading atmospheric oscillation parameters θ_{23} and $|\Delta m^2_{31}|$ emerges from the complementarity of atmospheric and accelerator neutrino data. We find the following best points and 1 σ errors:

$$\sin 2\theta_{23} = 0.50^{+0.07}_{-0.06}, |\Delta m^2_{31}| = 2.40^{+0.12}_{-0.11} \times 10^3 \text{ eV}^2. \tag{2.36}$$

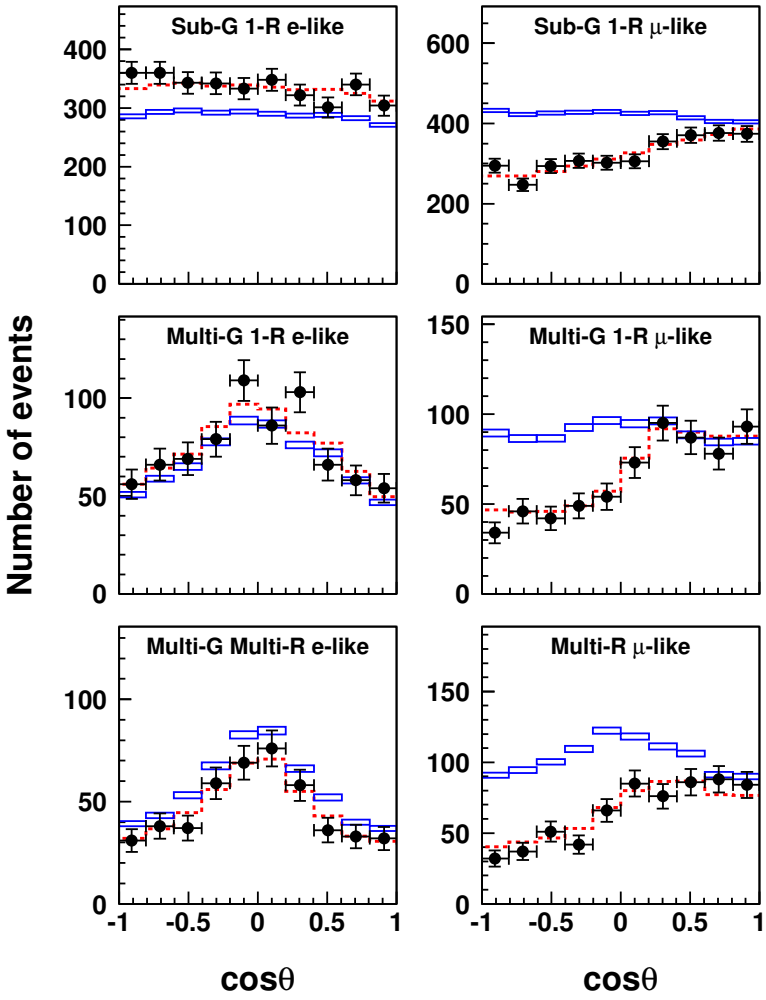

Figure 2.5: Zenith angle distributions of FC e-like, μ-like, PC, and UP μ are shown for data (filled circles with statistical error bars), MC distributions without oscillation (boxes) and best-fit distributions (dashed). The non-oscillated MC shows the distribution without fitting and the box height shows the statistical error [73].

CHOOZ

The CHOOZ experiment measured the neutrino flux at distance of about 1 km from two nuclear reactors in order to detect possible $\bar{\nu}_e \to \bar{\nu}_e$ oscillations. The detector holds 112 tons of scintillator. Neutrinos emitted at reactors have energies below 10 MeV and are detected above the threshold energy of 1.8 MeV using the reaction $\bar{\nu}_e p \to e^+ n$. The CHOOZ experiment is sensitive to $\Delta m^2 \sim 10^{-3}$ eV$^2 \sim |\Delta m^2_{31}|$. Using the fact that $\Delta m^2_{21} \sim 10^{-5}$ eV^2 and $\Delta m^2_{31} \sim 10^{-3}$ eV^2, the oscillation probability in three flavor neutrino at the CHOOZ is

$$P(\bar{\nu}_e \to \bar{\nu}_e) \approx 1 - \sin^2 2\theta_{13} \sin^2 \left(\frac{\Delta m^2_{31}}{4E} L \right). \tag{2.37}$$

Therefore, absence of neutrino oscillations at the CHOOZ experiment constrains the mixing angle θ_{13}.

Figure 2.7 shows that oscillations $\bar{\nu}_e \to \bar{\nu}_{e,\mu,\tau}$ are excluded for $\Delta m^2 = 8 \times 10^4$ eV^2 (90%

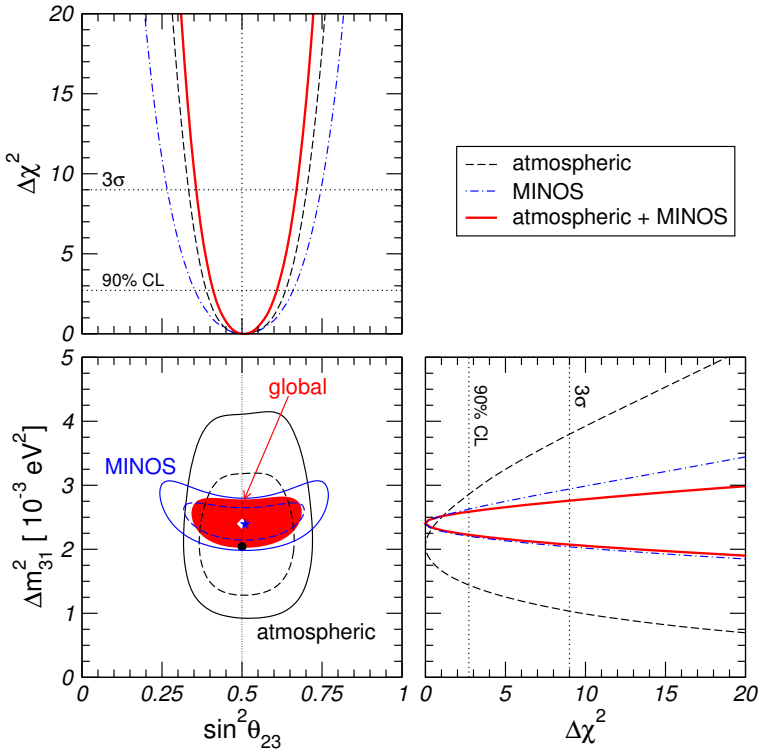

Figure 2.6: Determination of the leading atmospheric oscillation parameters from the interplay of data from artificial and natural neutrino sources. It shows χ^2-profiles and allowed regions at 90% and 99.73% C.L. (2 dof) for atmospheric and MINOS, as well as the 99.73% C.L. region for the combined analysis (including also K2K). The dot, star and diamond indicate the best fit points of atmospheric data, MINOS and global data, respectively. χ^2 minimize with respect to Δm^2_{21}, θ_{12} and θ_{13}, including always solar, KamLAND, and CHOOZ data [3].

C.L.) at the maximum mixing and $\sin^2(2\theta_{13}) = 0.17$ (90% C.L.) at large Δm^2 values.

The bound[1] on θ_{13} using the CHOOZ, atmospheric neutrino, K2K and MINOS data [3] is

$$\sin^2\theta_{13} \leq 0.027\ (0.058) \quad \text{at } 90\%\text{ C.L. } (3\sigma). \tag{2.39}$$

[1] In ref. [10], a global analysis of the neutrino oscillation data has shown hints for a non-vanishing value for θ_{13}, i.e.,

$$\sin^2\theta_{13} = 0.02 \pm 0.01 \quad \text{at } 1\sigma. \tag{2.38}$$

However, this claim has been questioned by ref. [74], and it seems [10] to require the full three flavor analysis of the atmospheric neutrino data by the SK collaboration itself to resolve this dispute. In this thesis, therefore, we use only the conservative bound (2.39).

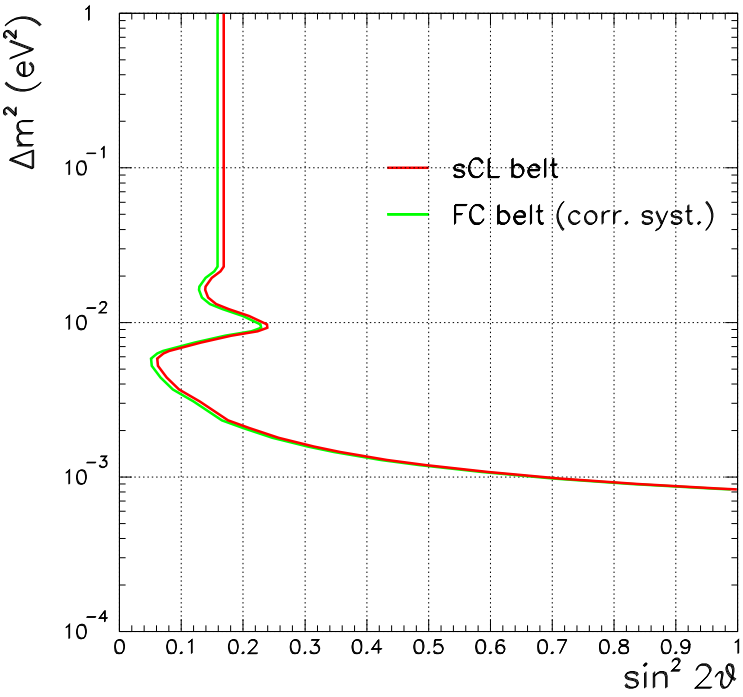

Figure 2.7: The CHOOZ exclusion plot at 90% CL for the oscillation parameters based on the differential energy spectrum; the FC contour, obtained with correct systematics treatment, is also shown [6].

Chapter 3

Resent status of four flavor neutrino oscillations

The values of the mass squared differences and the mixing angles of solar (Δm^2_{21}, θ_{12}) and atmospheric neutrinos (Δm^2_{31}, θ_{23}) are almost determined, as was explained in chapter 2.2.2. As for the other oscillation parameters, the only upper bound on the mixing angle θ_{13} is known and we have no informations of the CP phase δ. In order to precisely measure θ_{13} and δ, long baseline experiments with high intensity are planned. Such precision measurements for the "standard" three family neutrino parameters can discriminate the deviation from the three family neutrino model. On the other hand, as we saw in chapter 2.1, new particles will be required in order to generate neutrino masses. Such new particles may affect neutrino oscillations. For instance, if right handed neutrinos are introduced into the standard model, the left handed neutrinos can be mixed with charge conjugation of the right handed neutrinos; therefore, the right handed neutrinos can contribute neutrino to oscillation as "sterile" neutrinos [1].

A sterile neutrino has attracted much attention mainly in order to explain the result of LSND [27, 28, 29]. In the LSND experiment the neutrino beams are produced from the pion and muon decays mostly at rest:

$$\begin{aligned} \pi^+ &\to \nu_\mu + \mu^+ \\ &\qquad \hookrightarrow\ e^+\ \nu_e\ \bar{\nu}_\mu. \end{aligned}$$

The search for $\bar{\nu}_\mu \to \bar{\nu}_e$ was performed using the detection reaction $\bar{\nu}_e\ p \to e^+\ n$. $\nu_\mu \to \nu_e$ was also searched, but the number of events for this channel was extremely smaller than the one for $\bar{\nu}_\mu \to \bar{\nu}_e$ because of difference of the detection rates. LSND finds an evidence of the $\bar{\nu}_\mu \to \bar{\nu}_e$ transition and the average oscillation probabilities are

$$P(\bar{\nu}_\mu \to \bar{\nu}_e) = (2.6 \pm 0.8) \times 10^{-3}, \quad P(\nu_\mu \to \nu_e) = (1.0 \pm 1.6) \times 10^{-3}. \tag{3.1}$$

In the LSND experiment the neutrinos have energy $E_\nu \approx 10 - 50$ MeV and travel for distance $L \approx 30$m. Thus, the evidence of neutrino oscillations at LSND indicates the mass squared difference larger than $\Delta m^2_{31} \sim 10^{-3}$ eV^2 is required. The allowed region is shown in figure 3.2.

A four family neutrino scheme which consists of one sterile neutrino in addition to the three weakly interacting ones can be classified into two mass schemes. The scheme in

[1] A neutrino which do not couple to W and Z bosons is called a "sterile" neutrino [23].

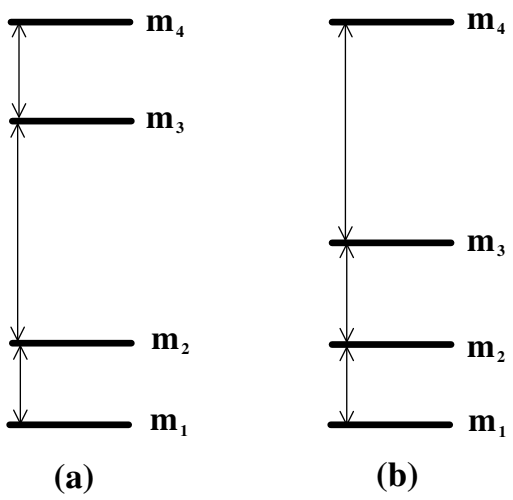

Figure 3.1: The two classes of four–neutrino mass spectra, (a): (2+2) and (b): (3+1).

which two mass eigenvalues are separated from the other is called (2+2) scheme (figure 3.1 (a)) and the scheme in which one mass eigenvalue is separated from the other is called (3+1) scheme (figure 3.1 (b)). These two schemes lead to different phenomenological consequences.

3.1 (2+2) scheme

A characteristic feature of (2+2) schemes is that the extra sterile state cannot simultaneously decouple from both solar and atmospheric oscillations. Because of this feature, (2+2) schemes is ruled out. This feature is explained in this section.

If the origin of the result of the zenith angle analysis of atmospheric neutrino observation is a neutrino oscillation, a muon neutrino must make the transition to a tau neutrino or a sterile one from the point of view of the detection, while the transition probability from a muon neutrino to an electron one must be small because of the CHOOZ data. In the CHOOZ experiment, relevant oscillation probability is as follows:

$$\begin{aligned} P(\bar{\nu}_e \to \bar{\nu}_e) \approx & -4\mathrm{Re}[U_{e3}U_{e3}^*U_{e4}^*U_{e4}]\sin^2\left(\frac{\Delta m_{34}^2}{4E}L\right) \\ & -2\mathrm{Im}[U_{e3}U_{e3}^*U_{e4}^*U_{e4}]\sin\left(\frac{\Delta m_{34}^2}{4E}L\right) \\ & +2|U_{e3}^*U_{e3}+U_{e4}^*U_{e4}|^2. \end{aligned} \tag{3.2}$$

Absence of the oscillation at CHOOZ leads to small values of U_{e3} and U_{e4}. On the other hand, ν_μ to ν_e transition probability for the atmospheric neutrino observations is as follows:

$$\begin{aligned} P(\bar{\nu}_\mu \to \bar{\nu}_e) \approx & -4\mathrm{Re}[\tilde{U}_{\mu3}\tilde{U}_{e3}^*\tilde{U}_{\mu4}^*\tilde{U}_{e4}]\sin^2\left(\frac{\Delta m_{34}^2}{4E}L\right) \\ & -2\mathrm{Im}[\tilde{U}_{\mu3}\tilde{U}_{e3}^*\tilde{U}_{\mu4}^*\tilde{U}_{e4}]\sin\left(\frac{\Delta m_{34}^2}{4E}L\right) \\ & +2|\tilde{U}_{\mu3}^*\tilde{U}_{e3}+\tilde{U}_{\mu4}^*\tilde{U}_{e4}|^2, \end{aligned} \tag{3.3}$$

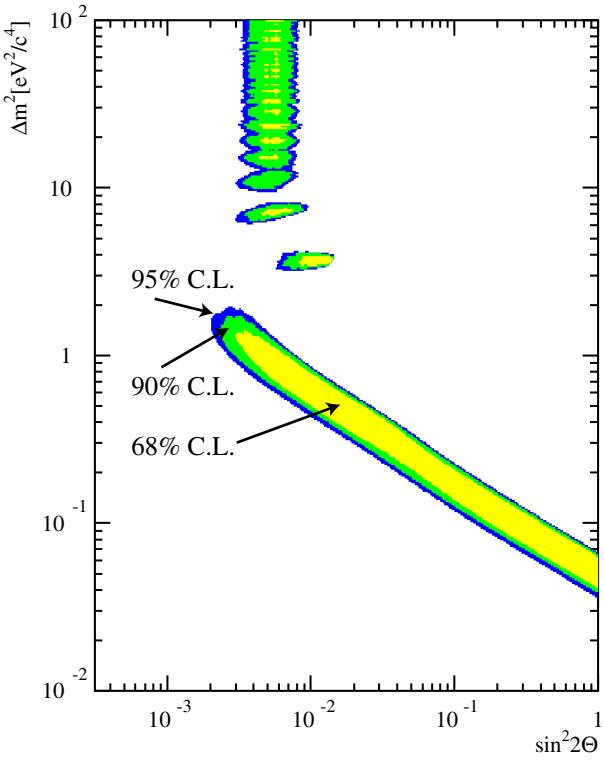

Figure 3.2: The LSND region at various confidence levels [75].

where $\tilde{U}_{e3(4)}$ stands for the mixing matrix element in matter. $\tilde{U}^*_{\mu 3}\tilde{U}_{e3}$ and $\tilde{U}^*_{\mu 4}\tilde{U}_{e4}$ are proportional to U_{e3} or U_{e4}. Hence, the transition probability from a muon neutrino to an electron one for the atmospheric neutrino observations must be small. It turns out that it is difficult to explain the result of the zenith angle analysis using ν_μ to ν_s transition. To explain this difficulty, we will consider it in two flavor neutrinos which are muon and sterile neutrinos and constant matter density, for simplicity. In a two flavor model, the PMNS mixing matrix elements in matter can be parametrized as follows:

$$\begin{aligned} \tilde{U}_{\mu 3} &= \cos\tilde{\theta}, \\ \tilde{U}_{\mu 4} &= \sin\tilde{\theta}, \\ \tilde{U}_{s3} &= -\sin\tilde{\theta}, \\ \tilde{U}_{s4} &= \cos\tilde{\theta}, \end{aligned} \tag{3.4}$$

where $\tilde{\theta}$ stands for the mixing angle in matter. In these parametrization, the ν_μ to ν_s transition probability is as follows:

$$P(\nu_\mu \to \nu_s) \approx \sin^2 2\tilde{\theta} \sin^2\left(\frac{\Delta\tilde{m}^2_{34}}{4E}L\right), \tag{3.5}$$

where

$$\sin 2\tilde{\theta} = \frac{\sin 2\theta}{\sqrt{\left(\frac{A_n}{2\Delta m^2_{34}} + \cos 2\theta\right)^2 + \sin^2 2\theta}}, \tag{3.6}$$

where $A_n = \sqrt{2}G_F E n_n$ and n_n stands for neutron density in matter. Notice that A_n changes its sign for $\bar{\nu}_\mu \to \bar{\nu}_s$. Eq. (3.6) means the mixing angle in matter can not become

the maximum mixing angle for both $\nu_\mu \to \nu_s$ and $\bar{\nu}_\mu \to \bar{\nu}_s$. However, the zenith angle analysis of atmospheric neutrino oscillations at SK (fig.2.6) show that the mixing angle for up-ward muon events including both $\mu^\pm$ is maximum. Thus, the results of the atmospheric neutrino oscillations is due to the flavor transition from ν_μ to ν_τ and the flavor transition from ν_μ to ν_s is extremely small. This means the following transition probability in the four family scheme is small:

$$\begin{aligned} P(\nu_\mu \to \nu_s) &\approx -4\mathrm{Re}[\tilde{U}_{\mu 3}\tilde{U}^*_{s3}\tilde{U}^*_{\mu 4}\tilde{U}_{s4}]\sin^2\left(\frac{\Delta m^2_{34}}{4E}L\right) \\ &\quad +2\mathrm{Im}[\tilde{U}_{\mu 3}\tilde{U}^*_{s3}\tilde{U}^*_{\mu 4}\tilde{U}_{s4}]\sin\left(\frac{\Delta m^2_{34}}{4E}L\right) \\ &\quad +2|\tilde{U}^*_{\mu 3}\tilde{U}_{s3}+\tilde{U}^*_{\mu 4}\tilde{U}_{s4}|^2. \end{aligned} \tag{3.7}$$

Eq. (3.7) have terms which proportional to $U_{\mu 3}U^*_{s3}$ and $U_{\mu 4}U^*_{s4}$ respectively. If the origin of the result of the zenith angle analysis is a $\nu_\mu \to \nu_\tau$ transition whose probability is

$$\begin{aligned} P(\nu_\mu \to \nu_\tau) &\approx -4\mathrm{Re}[\tilde{U}_{\mu 3}\tilde{U}^*_{\tau 3}\tilde{U}^*_{\mu 4}\tilde{U}_{\tau 4}]\sin^2\left(\frac{\Delta m^2_{34}}{4E}L\right) \\ &\quad +2\mathrm{Im}[\tilde{U}_{\mu 3}\tilde{U}^*_{\tau 3}\tilde{U}^*_{\mu 4}\tilde{U}_{\tau 4}]\sin\left(\frac{\Delta m^2_{34}}{4E}L\right) \\ &\quad +2|\tilde{U}^*_{\mu 3}\tilde{U}_{\tau 3}+\tilde{U}^*_{\mu 4}\tilde{U}_{\tau 4}|^2, \end{aligned} \tag{3.8}$$

it indicates $U_{\mu 3} \approx U_{\mu 4} \approx -U_{\tau 3} \approx U_{\tau 4} \approx 1/\sqrt{2}$ which is analogous to the three flavor analysis. Hence, we obtain

$$|U_{s3}|,\ |U_{s4}| \approx \epsilon \ \ (\epsilon \ll 1). \tag{3.9}$$

On the other hand, at Bugey which is a reactor experiment [108], the following oscillation channel is relevant:

$$P(\bar{\nu}_e \to \bar{\nu}_e) = 1 - 4(1-|U_{e3}|^2-|U_{e4}|^2)(|U_{e3}|^2+|U_{e4}|^2)\sin^2\left(\frac{\Delta m^2_{42}}{4E}L\right). \tag{3.10}$$

No evidence of neutrino oscillations at Bugey leads to

$$\begin{aligned} |U_{e3}|^2+|U_{e4}|^2 &\approx \epsilon' \\ &\text{or} \\ |U_{e3}|^2+|U_{e4}|^2 &\approx 1-\epsilon', \end{aligned} \tag{3.11}$$

where ϵ' stands for a small quantity, $\epsilon' \ll 1$. On the other hand, the relevant oscillation probability at KamLAND is

$$\begin{aligned} P(\nu_e \to \nu_e) &\approx 1 - 4|U_{e1}|^2|U_{e2}|^2\sin^2\left(\frac{\Delta m^2_{21}}{4E}L\right) \\ &\quad -2|U_{e3}|^2(1-|U_{e3}|^2-|U_{e4}|^2) \\ &\quad -2|U_{e4}|^2(1-|U_{e4}|^2). \end{aligned} \tag{3.12}$$

$|U_{e3}|^2+|U_{e4}|^2 \approx 1-\epsilon'$ indicate $|U_{e1}|^2 \approx |U_{e2}|^2 \approx \epsilon'$ because of unitarity of PMNS mixing matrix. Thus, energy dependence of neutrino oscillations at KamLAND leads to

$$|U_{e3}|, |U_{e4}| \approx \epsilon'. \tag{3.13}$$

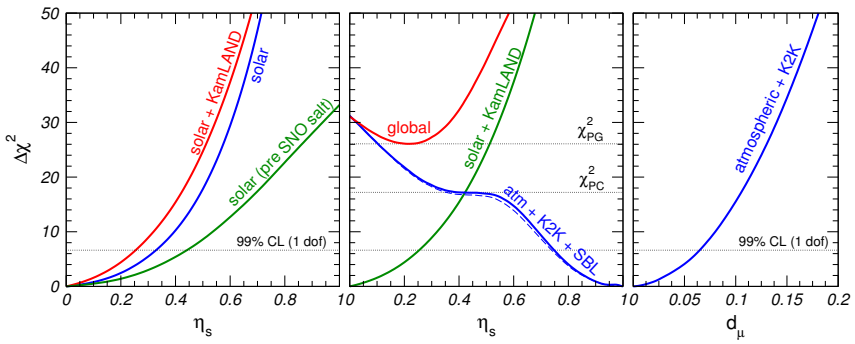

Figure 3.3: Left: $\Delta\chi^2$ as a function of η_s from solar data before the SNO salt-phase results, from current solar data, and from solar + KamLAND data. Middle: $\Delta\chi^2_{SOL}$, $\Delta\chi^2_{ATM+K2K+SBL}$ and $\bar{\chi}^2_{global}$ as a function of η_s in (2 + 2) oscillation schemes. The dashed line corresponds to atmospheric and K2K data only (without SBL data) [104].

Using the standard solar model (SSM), the fluxes of neutrinos produced in the Sun can be predicted. The results of SNO are consistent with the fluxes of neutrinos in the three family scheme. The results of SNO lead to

$$|U_{s1}|,\ |U_{s2}| \approx \epsilon'', \tag{3.14}$$

because the relevant oscillation probability for $\nu_e \to \nu_s$ channel is small and U_{s1} and U_{s2} are the remaining mixing matrix elements by eq. (3.9).

However, eq. (3.9) contradicts eq. (3.14) because of unitarity of PMNS mixing matrix. In particular, in Figure 3.3 we can see that at the 99% C.L. $\eta_s \equiv |U_{s1}|^2 + |U_{s2}|^2 \leq 0.25$ from the solar neutrino and KamLAND data, and $1 - \eta_s = |U_{s3}|^2 + |U_{s4}|^2 \leq 0.25$ from the atmospheric neutrino, K2K and the short baseline experiments, which contradicts the unitarity condition $\sum_{j=1}^{4} |U_{sj}|^2 = 1$. In fact the (2+2)-schemes are excluded at $\Delta\chi^2 = 30.7(1\ dof)\ (5.5\sigma)$ [39]. This conclusion is independent of whether we take the LSND data into consideration or not.

3.2 (3+1) scheme with the LSND constraint

On the other hand, (3+1)-schemes are not affected by the tension between the solar and atmospheric constraints on sterile neutrino oscillations, because as long as the sterile-neutrino mixings are small, then phenomenology of solar and atmospheric oscillations is approximately the same as that of the three family framework. MiniBooNE [30], latest short baseline experiment, is designed to confirm or refute the LSND result with high statistics. The result of MiniBooNE for the reconstructed neutrino-energy range from 475 MeV to 3000 MeV ("MB475") disfavors the LSND result [2]. Furthermore, the (3+1)

[2]At MiniBooNE for the neutrino-energy region from 475 MeV to 3000 MeV, the ν_e event data are consistent with no oscillations [30]. Whereas the number of ν_e events are not consistent with the number of the expected no oscillation events below 475 MeV (300 MeV $< E_\nu <$ 475 MeV) and 96±17±20 excess ν_e events are observed [30]. After this result, the events in the reconstructed neutrino energy range from 200 MeV to 475 MeV had been studied in more detail and in this analysis the excess of 128.8±20.4±38.8 events is observed [31]. Possible scenarios to explain the low energy excess are proposed [32, 39, 33, 34, 35, 36, 37, 46]. However, the result of anti-neutrino oscillation experiment at MiniBooNE give no indication of $\bar{\nu}_e$ excess event [40] and some of the scenarios are difficult to explain both the ν_e event excess and the

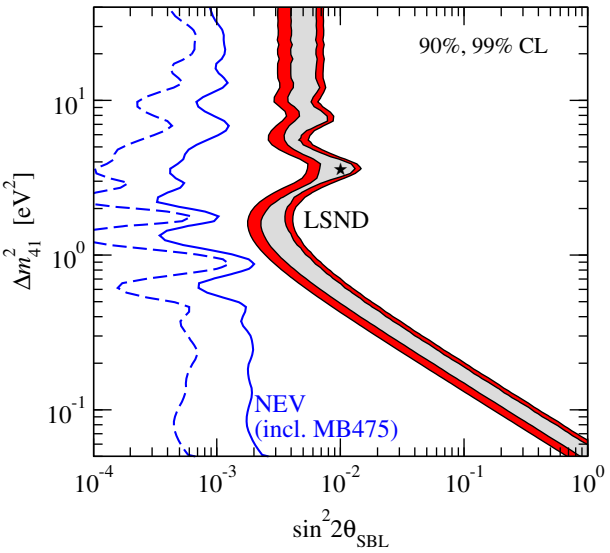

Figure 3.4: Allowed regions in (3+1) schemes from no-evidence (NEV) data at the short baseline experiments including MB475 (solid and dashed curves) and LSND (shaded regions) at 90% and 99% CL (2 dof). [39]

schemes have a problem only when one tries to account for LSND and all other negative results of the short baseline experiments such as Bugey, CDHSW [107]. To explain the LSND data while satisfying the constraints from other disappearance experiments, the oscillation probabilities of the appearance and disappearance channels have to satisfy the following relation [105, 106]:

$$\sin^2 2\theta_{\rm LSND}(\Delta m^2) < \frac{1}{4}\,\sin^2 2\theta_{\rm Bugey}(\Delta m^2)\cdot\sin^2 2\theta_{\rm CDHSW}(\Delta m^2) \tag{3.15}$$

where $\theta_{\rm LSND}(\Delta m^2)$, $\theta_{\rm CDHSW}(\Delta m^2)$, $\theta_{\rm Bugey}(\Delta m^2)$ are the value of the effective two-flavor mixing angle as a function of the mass squared difference Δm^2 in the allowed region for LSND ($\bar{\nu}_\mu \to \bar{\nu}_e$), the CDHSW experiment [107] ($\nu_\mu \to \nu_\mu$), and the Bugey experiment [108] ($\bar{\nu}_e \to \bar{\nu}_e$), respectively. The reason that the (3+1)-scheme to explain LSND is disfavored is basically because Eq. (3.15) is not satisfied for any value of Δm^2. The upper bound on $\sin^2 2\theta_{LSND}$ is shown in figure 3.4 using the negative data at KARMEN, CDHSW, Bugey, CHOOZ and Palo Verde [7], MiniBooNE("MB475") and the zenith angle analysis data of atmospheric neutrinos at SK which imply the mixing angle is maximum for up-ward muon events. We can find that these data are inconsistent with the result of LSND at more than 4 σ. Thus, it would be difficult to account for LSND and all other negative results of the short baseline experiments and the result of atmospheric neutrinos, within the (3+1)-scheme. (3+n)-schemes (n=2, 3) [38, 39] appear to have also difficulty to reconcile the LSND and the all other negative results of the short baseline experiments.

3.3 (3+1)-schemes without the LSND constraint

If we give up our effort to account for the LSND data, on the other hand, we no longer have the tension between LSND and the other short-baseline experiments (figure 3.4).

$\bar{\nu}_e$ event, simultaneously. MicroBooNE Experiment Liquid Argon TPC detector which can address the low-energy excess is approved at Fermilab and will report initial data in 2011 [41].

In this case we have only the upper bound on the extra mixing angles and this scenario satisfies all the experimental constraints (except that of LSND).

The PMNS mixing matrix U can be parametrized in terms of the six independent rotation angles θ_{ij} and the three (in the case of Dirac neutrinos) or six (in the case of Majorana neutrinos) phases, three phases of which are irrelevant to neutrino oscillations as we saw in chapter 2.2.2; Hence, the three phases can affect the phenomena of neutrino oscillations in both cases of Dirac neutrinos and of Majorana neutrinos. We consider the phenomena of neutrino oscillations in the so-called "atmospheric regime", with oscillation driven by the atmospheric mass squared difference, $\Delta m^2_{\rm atm} L/E \sim \mathcal{O}(1)$ in this chapter. In the atmospheric regime it is convenient to take the following parametrization:

$$U = R_{34}(\theta_{34},\, 0)\; R_{24}(\theta_{24},\, 0)\; R_{23}(\theta_{23},\, \delta_3)\; R_{14}(\theta_{14},\, 0)\; R_{13}(\theta_{13},\, \delta_2)\; R_{12}(\theta_{12},\, \delta_1)\,. \quad (3.16)$$

In Eq. (3.16), $R_{ij}(\theta_{ij},\ \delta_l)$ are the complex rotation matrices in the ij-plane defined as:

$$[R_{ij}(\theta_{ij},\ \delta_l)]_{pq} = \begin{cases} \cos\theta_{ij} & p = q = i, j \\ 1 & p = q \neq i, j \\ \sin\theta_{ij}\ e^{-i\delta_l} & p = i; q = j \\ -\sin\theta_{ij}\ e^{i\delta_l} & p = j; q = i \\ 0 & \text{otherwise.} \end{cases} \quad (3.17)$$

It is convenient to put phases in R_{12} and R_{13} so that one automatically drops in the limit $\Delta m^2_{\rm sol} L/E \to 0$ so that the other reduces to the "standard" three-family CP violating phase if sterile neutrinos are decoupled.

The extra mixing angles, θ_{14}, θ_{24} and θ_{34}, are constrained by neutrino oscillation experiments. In this section, we will consider the case that $\Delta m^2_{\rm SBL} \gg \Delta m^2_{\rm atm}$, where Δm^2_{SBL} stands for the mass squared difference probed at short baseline experiments and is identified as Δm^2_{41} here.

$\theta_{13}\theta_{14}$: Bugey constraints the mixing angle θ_{14}. At Bugey, relevant oscillation probability is

$$P(\bar\nu_e \to \bar\nu_e) \approx 1 - \sin^2 2\theta_{14} \sin^2\left(\frac{\Delta m^2_{\rm SBL}}{E} L\right). \quad (3.18)$$

Thus, absence of neutrino oscillations at Bugey imposes an upper bound on θ_{14}. Additionally, CHOOZ also imposes an upper bound on θ_{14}. The relevant oscillation probability is

$$P(\bar\nu_e \to \bar\nu_e) \approx 1 - c^4_{14} \sin^2 2\theta_{13} \sin^2\left(\frac{\Delta m^2_{\rm atm}}{E} L\right) - \sin^2 2\theta_{14} \sin^2\left(\frac{\Delta m^2_{\rm SBL}}{E} L\right). \quad (3.19)$$

Hence, absence of neutrino oscillations at CHOOZ imposes an upper bound on θ_{14} and also θ_{13}. These bounds on θ_{13} and θ_{14} using Bugey and CHOOZ data are shown in the left panel of figure 3.5. The result shows that both θ_{13} and θ_{14} cannot be much greater than 10°.

$\theta_{24}\theta_{34}$: Observation of atmospheric neutrinos can put on bound on the extra mixing angles, θ_{24} and θ_{34}. The oscillation probability for $\nu_\mu \to \nu_\mu$ channel (in vacuum) is

$$\begin{aligned} P(\nu_\mu \to \nu_\mu) \;\approx\; & 1 - 2c^2_{14}s^2_{24}(1 - c^2_{14}s^2_{24}) - 4\left[s^2_{23}c^2_{24}\left\{c^2_{24}(c^2_{23} - s^2_{13}) - s^2_{14}s^2_{24}\right\}\right. \\ & \left. - 2c^3_{24}s_{23}(1 - 2s^2_{23})s_{13}s_{14}s_{24}\cos(\delta_2 - \delta_3)\right] \sin^2\left(\frac{\Delta m^2_{\rm atm}}{4E} L\right). \end{aligned} \quad (3.20)$$

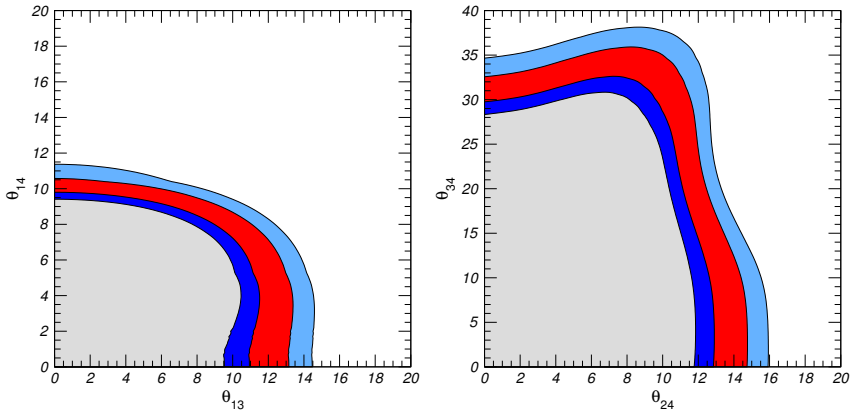

Figure 3.5: Left: Allowed parameter space at 90%, 95% and 99% CL in the $(\theta_{13}, \theta_{14})$ plane from null results at reactor experiments. Right: Allowed parameter space at 90%, 95% and 99% CL in the $(\theta_{24}, \theta_{34})$ plane from null results in atmospheric and LBL experiments [51].

The results of atmospheric neutrino zenith angle analysis at SK and K2K can be very well fitted in terms of three family oscillations, and these put a bound on θ_{24}. A bound on θ_{34} is derived from the atmospheric neutrino zenith angle analysis. Because the sterile neutrino do not feel the weak interaction unlike the standard weak interacted neutrinos, the matter effect in (3+1) scheme differs from the one in the standard three family scheme as we see that in (2+2) scheme. The bounds on θ_{24} and θ_{34} using the zenith angle analysis of atmospheric neutrinos at SK are shown in the right panel of the figure 3.5. The result shows that θ_{24} cannot be much greater than 10° like θ_{13} and θ_{14}; While θ_{34} is allowed up to around 30° because we cannot directly detect sterile neutrinos.

The oscillation probability of $\nu_\mu \to \nu_\tau$ channel in the atmospheric regime is

$$\begin{aligned} P(\nu_\mu \to \nu_\tau) \approx\ & 2s_{24}^2 s_{34}^2 + \left\{ \sin^2 2\theta_{23} \left[c_{13}^4 c_{24}^2 c_{34}^2 - s_{24}^2 s_{34}^2 \right] \right. \\ & -4 \sin 2\theta_{23} s_{13} s_{14} \left[s_{23} s_{34} \cos\delta_2 + c_{23} s_{24} \cos(\delta_2 - \delta_3) \right] \\ & \left. +2 \sin 2\theta_{23} s_{24} s_{34} c_{13}^2 c_{24}^2 c_{34} \left[c_{14}^2 - 2c_{13}^2 s_{23}^2 \right] \cos\delta_3 \right\} \sin^2 \left(\frac{\Delta m^2_{\rm atm}}{4E} L \right) \\ & \mp \sin 2\theta_{23} s_{24} s_{34} c_{13}^2 c_{14}^2 c_{24}^2 \sin\delta_3 \sin \left(\frac{\Delta m^2_{\rm atm}}{2E} L \right), \end{aligned} \tag{3.21}$$

i.e., the difference from oscillation probability in (3+1) scheme to one in the standard three family scheme is

$$\begin{aligned} \delta P(\nu_\mu \to \nu_\tau) &= P^{(4\nu)}(\nu_\mu \to \nu_\tau) - P^{(3\nu)}(\nu_\mu \to \nu_\tau) \\ &\approx \left\{ -(s_{24}^2 + s_{34}^2) \sin^2 2\theta_{23} + 2 \sin 2\theta_{23} (1 - 2s_{13}^2) s_{24} s_{34} \cos\delta_3 \right\} \sin^2 \left(\frac{\Delta m^2_{\rm atm}}{4E} L \right) \\ &\quad \mp \sin 2\theta_{23} s_{24} s_{34} \sin\delta_3 \sin \left(\frac{\Delta m^2_{\rm atm}}{2E} L \right) + 2s_{24}^2 s_{34}^2. \end{aligned} \tag{3.22}$$

We can understand that s_{34} dominantly contributes in the oscillation probability for the $\nu_\mu \to \nu_\tau$ channel from eq. (3.22).

OPERA experiment observes ν_τ transited from ν_μ produced at CERN and travel for distance $L = 730$ km. Mean energy of the neutrino beam is few-ten GeV. Therefore, the

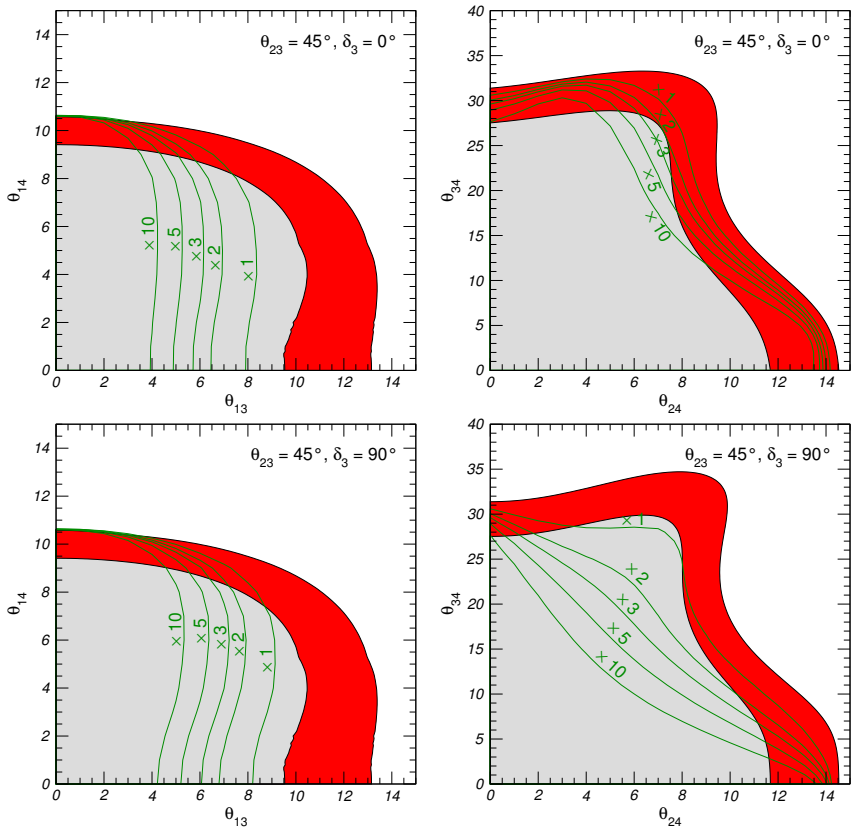

Figure 3.6: Sensitivity limit at 99% CL in the $(\theta_{13}, \theta_{14})$ plane (left) and in the $(\theta_{24}, \theta_{34})$ plane (right) from the combined analysis of present data and a null result of the OPERA experiment, assuming 1, 2, 3, 5 and 10 times the nominal intensity of 4.5×10^{19} pot/year with five year data taking. The colored regions show the present bounds at 90% and 99% CL. We assume $\theta_{23} = 45°$. and $\delta_3 = 0$. (top) or $\delta_3 = 90°$. (bottom). [51]

oscillation probability is eq. (3.21) up to miner corrections due to the earth matter effects and then is sensitive to θ_{34}. The sensitivity limits to θ_{24} and θ_{34} and also θ_{13} and θ_{14} at OPERA experiment using $\nu_\mu \to \nu_\tau$ and $\nu_\mu \to \nu_e$ channels are shown in figure 3.6. The results show that the sensitivity limit to θ_{34} is still allowed up to around 30° in the case of $\delta_3 = 90°$ (For $\delta_3 = 0°$, the bound on θ_{34} is not improved from the present one.).

Chapter 4

Four flavor neutrino oscillations at a neutrino factory

4.1 Oscillation probabilities in the four neutrino scheme

We investigate 3+1 sterile neutrino oscillations at a neutrino factory in this chapter. As explained in the chapter 2.2.2, the $\bar{\nu}_e \to \bar{\nu}_e$, the $\nu_\mu \to \nu_e$ and the $\nu_\mu \to \nu_\mu$ channels do not depend on the mixing angle θ_{34}. Therefore, it is impossible to limit θ_{34} in the leading order in the present approximation. This means that the large active-sterile mixing is allowed. For long baseline experiments such as K2K, MINOS, CNGS/OPERA, T2K and a neutrino factory, neutrinos pass through matter of the earth. For this reason, we should study the analytic formula of the oscillation probabilities in matter. To derive the oscillation probabilities, we adopt the Kimura-Takamura-Yokomakura (KTY) formalism [52, 53] (the details are given in the Appendix A). Furthermore, in order to simplify the forms of the formula, we will expand the probabilities with respect to the following small parameters:

$$\epsilon \equiv s_{34} \sim \sqrt{s_{13}} \sim \sqrt{s_{14}} \sim \sqrt{s_{24}} \sim \sqrt{\delta\theta_{23}} \lesssim 4 \times 10^{-1}.$$

The difference between four family neutrinos with three family neutrinos of the analytic formula of the the oscillation probabilities, $\delta P(\nu_\alpha \to \nu_\beta) = P^{(4)}(\nu_\alpha \to \nu_\beta) - P^{(3)}(\nu_\alpha \to \nu_\beta)$, are as follows:

$$\begin{aligned}
\delta P_{ee} &\sim \mathcal{O}\left(\epsilon^4\right), && (4.1)\\
\delta P_{e\mu} &\sim \delta P_{e\tau} \sim \delta P_{es} \sim \mathcal{O}\left(\epsilon^4\right), && (4.2)\\
\delta P_{\mu\mu} &= -2\left(A_n L\right) s_{24}\, s_{34} \cos\delta_3 \sin\Delta_{31} L + \mathcal{O}\left(\epsilon^4\right), && (4.3)\\
\delta P_{\mu\tau} &= -s_{34}^2 \sin^2 \frac{\Delta_{31} L}{2} + \left\{s_{24}\, s_{34} \sin\delta_3 + 2\left(A_n L\right) s_{24}\, s_{34} \cos\delta_3\right\} \sin\Delta_{31} L \\
&\quad + \mathcal{O}\left(\epsilon^4\right), && (4.4)\\
\delta P_{\mu s} &= s_{34}^2 \sin^2 \frac{\Delta_{31} L}{2} - s_{24}\, s_{34} \sin\delta_3 \sin\Delta_{31} L + \mathcal{O}\left(\epsilon^4\right). && (4.5)
\end{aligned}$$

First of all, we can understand that $\nu_\mu \to \nu_\tau$ channel is sensitive to θ_{34} since the first term in eq. (4.4) is proportional to s_{34}^2. This result is consistent with one in a vacuum. Therefore, we can understand that this channel is the best option to search for the sterile neutrino oscillations. The sensitivity limits to θ_{34} at the CNGS/OPERA is shown in figure 3.6 [51]. The $\nu_\mu \to \nu_\mu$ disappearance channel is a better option to search

for the sterile neutrino oscillations since the dominant term in eq. (4.3) is proportional to $2\,(A_n L)\,s_{24}\,s_{34}\cos\delta_3$ except the case of $\cos\delta_3 \approx 0$. The oscillation probability $P(\nu_\mu \to \nu_e)$ at MINOS, at T2K and at a neutrino factory and $P(\bar{\nu}_\mu \to \bar{\nu}_e)$, $P(\nu_e \to \nu_\mu)$ and $P(\bar{\nu}_e \to \bar{\nu}_\mu)$ at a neutrino factory are small. The reason of this is as follows. If we limit θ_{13} and θ_{14} to zero, the effective Hamiltonian, eq. (2.24), is the following matrix form:

$$U\mathcal{E}U^{-1} + \mathcal{A}(t) = \begin{pmatrix} A_e(t) & 0 & 0 & 0 \\ 0 & * & * & * \\ 0 & * & * & * \\ 0 & * & * & * \end{pmatrix}. \tag{4.6}$$

This means that a electron neutrino state is equal to a mass eigen state, $\mid \nu_e\rangle = \mid \nu_1\rangle$ in this approximation, and the other flavor neutrino states $\mid \nu_\mu\rangle$, $\mid \nu_\tau\rangle$ and $\mid \nu_s\rangle$ consist of the remaining mass eigen states $\mid \nu_2\rangle$, $\mid \nu_3\rangle$ and $\mid \nu_4\rangle$. For this reason, we can understand that $P(\nu_x \to \nu_e)$ and $P(\bar{\nu}_e \to \bar{\nu}_x)$ $(x = e, \mu, \tau, s)$ are proportional to s_{13} and s_{14}. The leading term in $P(\mu_e \to \nu_\mu)$ $(P(\nu_\mu \to \nu_e))$ and also in $P(\bar{\nu}_e \to \bar{\nu}_\mu)$ $(P(\bar{\nu}_\mu \to \bar{\nu}_e))$ at a neutrino factory are actually proportional to s^2_{13}, s^2_{14} and $s_{13}s_{14}$. Therefore, $P(\nu_\mu \to \nu_e)$ and $P(\bar{\nu}_e \to \bar{\nu}_e)$ are small since s_{13} and s_{14} are small, as was shown in the chapter 3. The $\nu_\mu \to \nu_\tau$ channel has not been studied in detail in the framework of neutrino factories studies (with the possible exceptions of refs. [116, 117]), but it is one of the the single most important channels to study new physics [93, 94, 95], if the related experimental problems could be overcome. As we will see below, this channel turns out to play an important role to probe the CP phases which are characteristic to the four neutrino scheme. For these reasons, we will name $\nu_\mu \to \nu_\tau$ throughout this thesis as "*the discovery channel*".

4.2 Neutrino Factory and the Hybrid-MIND detector

In Neutrino Factory [16, 76], muons are first produced with a multi-MW proton source accelerated up to energy of several tens of GeV and finally injected into a storage ring with long straight sections aimed at one or more detectors. The $\mu^+ \to e^+\nu_e\bar{\nu}_\mu$ and $\mu^- \to e^-\bar{\nu}_e\nu_\mu$ provide a very well known two-flavor neutrino flux with energy in the range $0 \leq E_\nu \leq E_\mu$. Neutrino Factory designs have been proposed in Europe [120, 121], US [122, 123, 124, 125] and Japan [126]. The dedicated *International Scoping Study for a future Neutrino Factory and Super-Beam facility* (ISS) showed that provided sufficient resources an accelerator complex capable of providing about 10^{21} muon decays of a given polarity per year can be built. We define the Neutrino Factory setup as follows: muons of both polarities are accelerated up to $E_\nu = 50$ GeV and injected into one storage ring with a geometry that allows to aim at two far detectors; the first located at 3000 km and the second at 7500 km from the neutrino beam source. The longest baseline corresponds to the so-called "magic baseline" where three-family CP-violating effects vanish. An alternative option, considered in the final ISS Accelerator Report [26], is to inject the muon beam into different storage rings, each of them aimed at a single far detector. The number of useful muon decays per year aimed at each detector has been fixed to 2×10^{21}. This number is rather conservative since in the final ISS Physics Report with a similar storage ring(s) geometry 5×10^{21} useful muon decays per year aimed at each detector are considered. Four years of data taking for each muon polarity are envisaged.

The Neutrino Factory fluxes for μ^- accumulated in the storage ring at $L = 3000$ km as a function of the neutrino energy for $E_\mu = 50$ GeV are shown in the left panel of fig.4.1. Two detectors of different technologies have been considered to detect the ν_μ and ν_τ signals. The first one is a magnetized iron calorimeter, that was proposed with a slightly different design in ref.[133] to measure the "golden" $\nu_e \to \nu_\mu$ wrong-sign muons signal. The second detector is a Magnetized Emulsion Cloud Chamber (MECC) [56], an evolution of the ECC modeled after OPERA that was first considered for Neutrino Factory studies in refs.[58, 134] to look for the "silver channel" $\nu_e \to \nu_\tau$ (a channel that can be looked at only in a Neutrino Factory setup). The $\nu_\mu N$ and $\nu_\tau N$ cross-section on iron as a function of the neutrino energy for both neutrinos and anti-neutrinos are shown in the right panel of fig.4.1. Notice that the adopted setup, similar to those proposed in the first Neutrino Factory studies (see, for example, refs. [57, 97]), slightly differs from the setup that was suggested in the final ISS Physics Report [26]. The latter consists in stored muons with energies in the range 20 GeV $\leq E_\mu \leq$ 30 GeV, aim at two detectors located at $L = 4000$ km and $L = 7500$ km from the source. The shortest baseline was optimized in the ISS Physics Report to look for CP-violating three-family signals, finding that a detector with a baseline of $L = 4000$ km performed slightly better than at $L = 3000$ km. This optimization, however, is no longer valid when looking for the (3+1)-neutrino model signals. Therefore, we decided to adopt the $L = 3000$ km baseline used in previous studies, for which possible sites have already been explored. We use a stored muon energy that is larger than the optimal value adopted in the ISS Physics Report, again chosen to maximize the sensitivity to three-family observables such as θ_{13}, the sign of the atmospheric mass difference and the three-family CP-violating phase δ. It is indeed well known from previous studies (see, for example, ref.[129] for an optimization of the muon energy to look for non-standard interaction signals at the Neutrino Factory) that to look for new physics the higher the muon energy the better. An evident motivation for this is that the $\nu_\mu \to \nu_\tau$ channel is very important to look for new physics in neutrino oscillations, and high neutrino energies are required to circumvent the extremely low cross-section in the tens of GeV energy range (see the right panel of fig.4.1). To show that the 50 GeV Neutrino Factory setup proposed above is more suited to look for sterile neutrino signals, we will compare our results with an ISS-inspired Neutrino Factory, defined as follows: muons of both polarities are accelerated up to $E_\nu = 20$ GeV and injected into storage ring(s) with a geometry that allows to aim at two far detectors, the first located at 4000 km and the second at 7500 km from the source. The number of useful muon decays per year aimed at each detector has been fixed in this case to 5×10^{20}, following the final ISS Physics Report. Four years of data taking for each muon polarity are envisaged. When studying the performance of the ISS-inspired 20 GeV setup, we consider the same detectors as in the case of the 50 GeV Neutrino Factory.

4.2.1 The Magnetized Iron Neutrino Detector to search $\nu_e \to \nu_\mu$ and $\nu_\mu \to \nu_\mu$ oscillation

We use the Magnetized Iron Neutrino Detector (MIND) [132] which is a 50 kton magnetized iron calorimeter of the MINOS type to look for the golden channel($\nu_e \to \nu_\mu$ or $\bar{\nu}_e \to \bar{\nu}_\mu$) and the ν_μ disappearance channel ($\nu_\mu \to \nu_\mu$ or $\bar{\nu}_\mu \to \bar{\nu}_\mu$) for both the shorter and longer baselines in this thesis.

Studies of the four-family $\nu_e \to \nu_\mu$ oscillation (still the best channel to measure θ_{13})

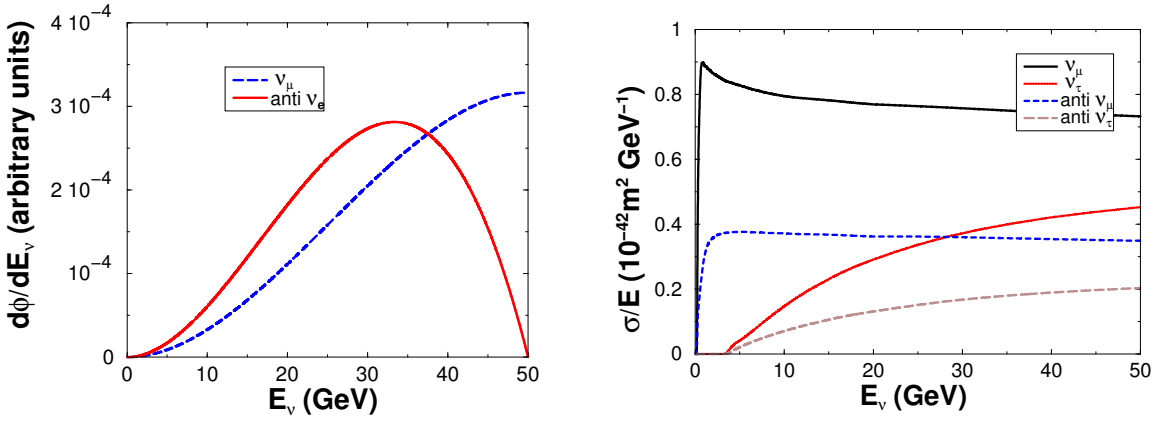

Figure 4.1: Left: 50 GeV Neutrino Factory fluxes at $L = 3000$ km; Right: the $\nu_\mu N$ and $\nu_\tau N$ cross-sections on iron [131]

are not different from those performed in the framework of the three-family model. In particular, no new sources of background are expected. Quite the contrary, those backgrounds induced by wrongly reconstructed $\bar{\nu}_\mu$ are expected to decrease for large values of θ_{34}, due to the increased oscillation into sterile neutrinos, see eq.(4.5). When looking at $\nu_\mu \to \nu_s$ oscillations, we will therefore take advantage of the wrong-sign muon identification efficiency presented in the ISS Detector Report [56]: $\epsilon_{e\mu} = 0.7$ above 10 GeV with the efficiency increasing linearly from $\epsilon_{e\mu} = 0.1$ at 1 GeV.

We can also study the $\nu_\mu \to \nu_\mu$ disappearance channel using the MIND. For the right-sign muon sample there is no need to accurately tell the charge of the muon, since the background induced by misidentified wrong-signs muons is negligible with respect to the signal [139]. We can safely use for this signal the muon identification efficiency of the MINOS experiment [140]: $\epsilon_{\mu\mu} = 0.9$ above 1 GeV. Notice that at the MIND detector it is not possible to single out τ's decaying into muons. We cannot thus use MIND to study the leading $\nu_e \to \nu_\tau$ oscillation and the "silver" channel ($\nu_e \to \nu_\tau$). We have considered as background for the ν_μ disappearance channel 10^{-5} of all neutral current events, all wrong-sign muon events and the right-sign muons coming from $\nu_\mu \to \nu_\tau$ oscillation with τ decaying into muons. The inclusion of this background has no effect on our results for this channel that are remarkably systematic-dominated. Throughout our numerical simulations we have assumed 2% and 5% for the bin-to-bin uncorrelated systematic errors on the golden channel and on the ν_μ disappearance signal. We have also assumed 1% and 5% for normalization and energy spectrum distorsion as the correlated systematic errors for all the channels.

4.2.2 The Magnetized Emulsion Cloud Chamber to search $\nu_e \to \nu_\tau$ and $\nu_\mu \to \nu_\tau$ oscillation

We use a 4 kton Magnetized Emulsion Cloud Chamber (MECC) [56] at a Neutrino Factory to look for the silver channel ($\nu_e \to \nu_\tau$ or $\bar{\nu}_e \to \bar{\nu}_\tau$) and the discovery channel ($\nu_\mu \to \nu_\tau$ or $\bar{\nu}_\mu \to \bar{\nu}_\tau$) have been published in ref.[134]. $\nu_e, \nu_\mu \to \nu_\tau$ ($\bar{\nu}_e, \bar{\nu}_\mu \to \bar{\nu}_\tau$) signal can be tagged looking for right-sign muons in coincidence with a τ decay vertex to distinguish them from ν_μ disappearance muon in an Emulsion Cloud Chamber (ECC) which is used at CNGS/OPERA experiment. In the MECC proposal [56] the lead plates which is used

in the OPERA detector are replaced by iron plates, again interleaved with emulsions layers. Thus, the MECC can be directly magnetized through the iron plates. Emulsion spectrometers (currently in their test phase [143]) are located at the end of the MECC section. The MECC is placed in front of the MIND detector. Such a detector is called "Hybrid-MIND". The efficiency of τ detection in the MECC is much higher than in the case of ECC, because tau decays into electrons and hadrons can be used in addition to $\tau \to \mu$. The expected efficiency is approximately five times larger than one in the ECC [56, 144]. For the silver channel, we will use an energy dependent efficiency $\epsilon_{e\tau}$ taken from ref.[134] multiplying it by a factor five. On the other hand, a detailed study of the efficiency for the discovery channel at the MECC is lacking. We will therefore assume a constant efficiency $\epsilon_{\mu\tau} = 0.65$ above 5 GeV [51].

The backgrounds for the silver and the discovery channels should be also correspondingly increased at the MECC with respect to the ECC ones. At the ECC, the expected signal-to-background ratio (after some kinematical cuts) for $\nu_\mu \to \nu_\tau$ (using the $\tau \to \mu$ decay channel only) is 50:1 or larger [51], the dominant source of background for the process $\nu_\mu \to \nu_\tau \to \tau^- \to \mu^-$ being represented by non-oscillated muons that produce charmed mesons finally decaying into μ^- either through NC or CC in which the muon is not observed. No detailed study of the expected background for $\nu_e \to \nu_\tau$ or $\nu\mu \to \nu_\tau$ signals at the MECC exposed to a Neutrino Factory beam has been performed yet, though. We have thus decided to make the assumption that, using MECC, all τ decay channels should be affected by similar backgrounds. We have therefore consistently multiplied the backgrounds for $\nu_e \to \nu_\tau$ and $\nu_\mu \to \nu_\tau$ computed in refs.[51, 134] by a factor five.

Also in this case, we have grouped events into 10 bins with ΔE_ν=5 GeV constant energy resolution. We have assumed 10% for the bin-to-bin uncorrelated systematic errors, 1% and 5% for normalization and energy spectrum distorsion as the correlated systematic errors throughout the numerical simulations for both $\nu_e \to \nu_\tau$ and $\nu_\mu \to \nu_\tau$ signals.

Tab.4.1 shows the expected number of τ^- from $\nu_\mu \to \nu_\tau$ and τ^+ from $\bar{\nu}_e \to \bar{\nu}_\tau$ for a 1 kton MECC detector with perfect efficiency, exposed to 2×10^{20} $(\nu_\mu, \bar{\nu}_e)$ flux for one year, for different values of $\theta_{13}, \theta_{14}, \theta_{24}$ and θ_{34}. The other parameters are $\theta_{12} = 34^\circ$, $\theta_{23} = 45^\circ$, $\Delta m^2_{21} = 7.9 \times 10^{-5}$ eV^2, $\Delta m^2_{31} = \Delta m^2_{32} = 2.4 \times 10^{-3}$ eV^2, $\Delta m^2_{41} = \Delta m^2_{42} = \Delta m^2_{43} = 1$ eV^2, $\delta_1 = \delta_2 = 0$ and $\delta_3 = 90^\circ$. For comparison, the rates at the CNGS (for the nominal CNGS flux, 4.5×10^{19} pot/year, an active lead target mass of 1.8 kton and 5 years of data taking) and the expected number of events in the three-family model for a 1 kton MECC detector with perfect efficiency are also shown. We can see that the number of expected τ^- events at the 1 kton MECC is $\mathcal{O}(500)$ at the both baselines. The fact that at both baselines we expect a similar number of events is a consequence of the convolution of $\nu_\mu \to \nu_\tau$ oscillation probability with the $\nu_\tau N$ cross-section and the ν_μ neutrino flux; at the the shortest baseline, the probability is maximal below 10 GeV; at the longest baseline, the maximum is located in the 30 GeV bin. The higher cross-section for this energy bin compensates for the decrease in the ν_μ neutrino flux, thus giving a similar number of τ events in the detector.

4.3 Sensitivity to the mixing angles θ_{24} and θ_{34}

In this section, we investigate sensitivities to the angles θ_{24} and θ_{34}. We know that the ν_μ disappearance channel ($\nu_\mu \to \nu_\mu$) and the discovery channel ($\nu_\mu \to \nu_\tau$) are sensitive to θ_{24} and θ_{34} because the contributions of θ_{24} and θ_{34} to the transition probabilities, eq. (4.3)

$(\theta_{13};\theta_{14};\theta_{24};\theta_{34})$	$N_{\tau^-}^{CNGS}$	$N_{\tau^-}^{3000}$	$N_{\tau^+}^{3000}$	$N_{\tau^-}^{7500}$	$N_{\tau^+}^{7500}$
$(5°;5°;5°;20°)$	8.9	559	10	544	2
$(5°;10°;5°;20°)$		557	29	544	5
$(5°;5°;10°;20°)$	8.3	474	11	529	2
$(5°;5°;10°;30°)$	10.5	384	18	454	3
$(5°;10°;5°;30°)$		424	59	441	11
$(5°;5°;10°;30°)$	10.5	384	18	454	3
$(10°;5°;5°;20°)$	8.5	522	22	512	2
$(10°;10°;5°;20°)$		517	42	510	6
$(10°;5°;10°;20°)$	7.9	443	22	498	2
$(10°;5°;5°;30°)$	6.5	397	30	413	4
$(10°;10°;5°;30°)$		389	74	412	11
$(10°;5°;10°;30°)$	10.3	361	30	428	4
3 families, $\theta_{13}=5°$	15.1	797	3	666	0
3 families, $\theta_{13}=10°$	14.4	755	12	632	1

Table 4.1: *Event rates for the $\nu_\mu \to \nu_\tau$ and $\bar{\nu}_e \to \bar{\nu}_\tau$ channels for 1 kton MECC detector, exposed to a 2×10^{20} $(\nu_\mu,\bar{\nu}_e)$ flux for one year, for different values of θ_{14},θ_{24} and θ_{34} in the (3+1) scheme. The other unknown angle, θ_{13} has been fixed to: $\theta_{13}=5°,10°$. The CP-violating phases are: $\delta_1=\delta_2=0$; $\delta_3=90°$. As a reference, rates at the 1.8 kton OPERA detector (exposed to the nominal CNGS beam intensity) and the expected event rates for 1 kton MECC detector in the case of the three-family model (i.e., for $\theta_{i4}=0$ and maximal CP-violating phase δ) are also shown. In all cases, perfect efficiency is assumed.*

and eq. (4.4) , are third order of ϵ in these channels unlike in the other ones. For this reason, we use these two channels to investigate sensitivities to θ_{24} and θ_{34}.

Throughout this subsection, we fix the parameters as follows: $\theta_{12}=34°$, $\theta_{13}=5.74°$, $\theta_{14}=0$, $\Delta m^2_{21}=7.9\times10^{-5}$ eV^2, $\Delta m^2_{31}=2.4\times10^{-3}$ eV^2, $\Delta m^2_{41}=1$ eV^2, where these parameters except Δm^2_{41} are the common values in the three and the four family schemes.

We define the chi squared as follows:

$$\begin{aligned}\Delta\chi^2 \;=\; \min_{marg\ par}\Bigg[\sum_{pol.,chan.,L}\min_{\alpha_{s,b},\beta_{s,b}}\Bigg\{\sum_i\frac{1}{\sigma_i^2}\Big((1+\alpha_s+x_i\beta_s)N_i(4f)+(1+\alpha_b+x_i\beta_b)B_i(4f)\\ -N_i^0-B_i^0\Big)^2+\left(\frac{\alpha_s}{\sigma_{\alpha s}}\right)^2+\left(\frac{\alpha_b}{\sigma_{\alpha b}}\right)^2+\left(\frac{\beta_s}{\sigma_{\beta s}}\right)^2+\left(\frac{\beta_b}{\sigma_{\beta b}}\right)^2\Bigg\}+\Delta\chi^2_{prier}\Bigg],\end{aligned} \tag{4.7}$$

where i stand for the i-th bin grouping events in ten (four) constant energy resolution bins of width $\Delta E_\nu=4$ GeV from 1 GeV to 5 GeV and $\Delta E_\nu=5$ GeV from 5 GeV to 50 GeV (20 GeV) at the 50 GeV (20GeV) Neutrino Factory. $N_i(4f)$ ($B_i(4f)$) stands for number of events (the background) corresponding to the i-th bin in the four family scheme.

We generate number of events which is $N_i(4f)+B_i(4f)$ and then fit number of events $N_i^0+B_i^0$ with $\Delta m^2_{41}=0$ eV^2, $\theta_{23}=45°$, $\theta_{24}=\theta_{34}=\theta_{34}=0$, $\delta_1=\delta_2=\delta_3=0$ in the four family scheme.

In the minimization procedure in eq.(4.7), "marg par" stands for the oscillation parameters to be marginalized over (that can be different for different plots), and $\alpha_s,\alpha_b,\beta_s$ and

β_b are the variables for the correlated systematic errors, which stand for the uncertainties in the overall normalization and in the linear distortion in the spectral shape in the magnitude of signal (s) or background (b) [135], where we have defined $x_i = E_i/(E_{max} - E_{min})$ for neutrino energy E_i for the i-th bin. Following ref.[135], we assume the correlated systematic errors $\sigma_{\alpha s} = \sigma_{\alpha b} = 0.01$ for the normalization and $\sigma_{\beta s} = \sigma_{\beta b} = 0.05$ for the spectrum distortion. In the analysis of the case with single baseline length, we have minimized the χ^2 for each baseline separately, i.e., no sum is performed over L, and in the analysis combining the two baselines, we have minimized the sum of χ^2 for each baseline. Similarly, in the analysis of a single channel, no sum is performed over the channels ("chan."), while in the analysis combining the different channels we have summed over the different channels, i.e., golden and silver in this Section. In all cases we sum up χ^2 for the two possible stored muon polarities ("pol.").

The variance is defined by

$$\sigma_j^2 = N_j^0 + B_j^0 + [f_j N_j^0]^2 + [f_j B_j^0]^2, \tag{4.8}$$

where f_j stands for the uncorrelated bin-to-bin systematic error in the j-th bin; $f_j = 2\%$ for the golden channel, $f_j = 10\%$ for the silver channel, $f_j = 5\%$ for the ν_μ disappearance channel and $f_j = 10\%$ for the discovery channel.

$\Delta\chi^2_{prior}$ are the prior contributed by the solar and the atmosphere neutrino observations and the reactor and the accelerator neutrino experiments which is defined as follows:

$$\begin{aligned}\Delta\chi^2_{prior} &= \frac{(s^2_{23}(4f) - 0.50)^2}{(\sigma^2(s^2_{23}))} + \frac{(|\Delta m^2_{31}(4f)| - 2.4\times 10^{-3}\ \mathrm{eV}^2)^2}{\sigma^2(|\Delta m^2_{31}|)} \\ &+ \frac{(s^2_{13}(4f) - 0.01)^2}{\sigma^2(s^2_{13})} + \frac{s^2_{14}}{\sigma^2(s^2_{14})} + \frac{s^2_{24}}{\sigma^2(s^2_{24})} + \frac{s^2_{34}}{\sigma^2(s^2_{34})}\end{aligned} \tag{4.9}$$

and

$$\begin{aligned}\sigma(s^2_{23}) &= 0.07, \quad \sigma(|\Delta m^2_{atm}|) = 0.12\times 10^{-3}\ \mathrm{eV}^2, \quad \sigma(s^2_{13}) = 0.016 \\ \sigma(s^2_{14}) &= 0.013, \quad \sigma(s^2_{24}) = 0.02, \quad \sigma(s^2_{34}) = 0.12.\end{aligned} \tag{4.10}$$

we have marginalized over $\theta_{24} \in [0, 12^\circ]$, $\theta_{34} \in [0, 35^\circ]$ and δ_2, $\delta_3 \in [0, 360^\circ]$. Matter effects have been included considering a constant matter density $\rho_e = 3.4\mathrm{g/cm}^3$ for the shortest baseline and $\rho_e = 4.3\mathrm{g/cm}^3$ for the longest one, computed averaging over the density profile in the PREM [114] along the neutrino path. We have checked that marginalization over a 10% matter density uncertainty does not modify our results.

The sensitivity limits to θ_{24} and θ_{34} at 90 % CL [1] are shown in fig.4.2. For the 3000 km baseline, the discovery channel is sensitive to θ_{34} and can constrain $\theta_{34} \leq 17^\circ$ which is a half of the present bound ($\theta_{34} \lesssim 30^\circ$). While the ν_μ disappearance channel is sensitive θ_{24} rather than the discovery channel. For the 7500 km baseline, the ν_μ disappearance channel is sensitive to θ_{34} and constrain $\theta_{34} \leq 15^\circ$ in contrast with the 3000 km baseline because of the matter effect. We can understand the reason why the matter effect make changes to the sensitivity to θ_{34} for the ν_μ disappearance channel by eq. (4.3). Eq. (4.3) show that s_{34} term appear if it is impossible to neglect the potential A_n. The sensitivity to θ_{24} at 7500 km is the same at 3000 km.

[1] The contour for which the 2 d.o.f.'s $\Delta\chi^2$ is $\Delta\chi^2 = 4.61$ defines, then, the region of the parameter space of the (3+1)-sterile neutrino model that is non-compatible at 90 % CL with the input data corresponding to vanishing $(\theta_{24}, \theta_{34})$ (to the right of the contour line) and the region that it is still allowed (to the left of the line) at this CL.

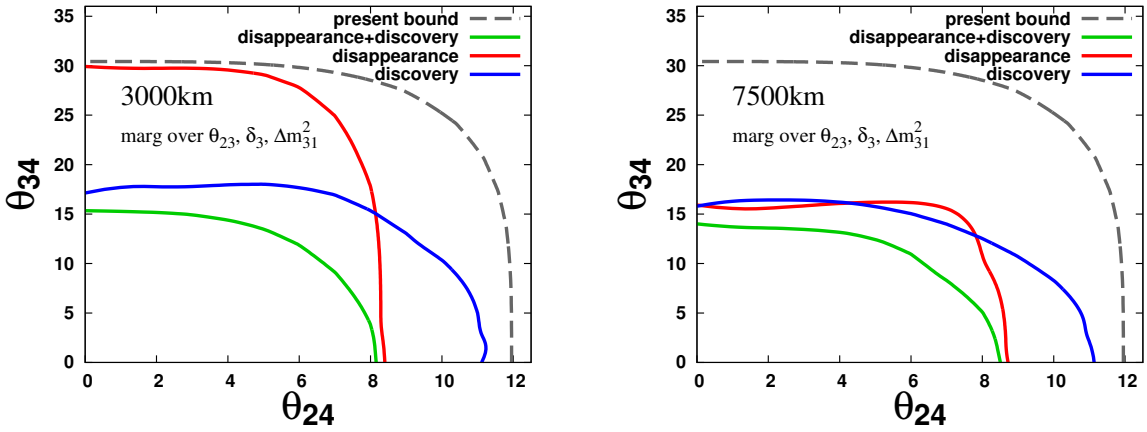

Figure 4.2: The sensitivity limits at 90% C.L. to θ_{24} and θ_{34} for 3000 km baseline (the left panel) and 7500 km baseline (the right panel). The blue lines, the red lines and the green lines stand for the discovery channel, the ν_μ disappearance and the combination of both the channels. The dashed gray line stand for the present bound.

Fig. 4.3 show that the sensitivity limits at 90% C.L. to θ_{24} and θ_{34} for the combination of the two baselines. The combination of both the channels constrain $\theta_{24} \leq 7^\circ$ and $\theta_{34} \leq 12^\circ$. For the 20 GeV Neutrino Factory, the combination of both the channels constrain $\theta_{24} \leq 8^\circ$ and $\theta_{34} \leq 14^\circ$. The sensitivity to θ_{24} at the 20 GeV Neutrino Factory is almost the same as it at the 50 GeV Neutrino Factory. On the other hand, the sensitivity to θ_{34} at the 20 GeV Neutrino Factory is worse rather than it at the 50 GeV Neutrino Factory. Because the smaller tau neutrino-nucleon cross section is, the lower an energy of the tau neutrino beam is (see fig.4.1).

We can understand that the correlated systematic errors affect the sensitivity to θ_{24} for the ν_μ disappearance channel and the sensitivity to θ_{24} and θ_{34} for the discovery channel at the 50 GeV Neutrino Factory. On the other hand, at the 20 GeV Neutrino Factory the correlated systematic errors do not change the sensitivity to θ_{24} and θ_{34}.

4.4 Sensitivity to the mixing angles θ_{13} and θ_{14}

4.4.1 Sensitivity to the mixing angles θ_{13} and θ_{14}

In this section, we investigate the sensitivities to the mixing angles $\theta_{13}^{(4f)}$ and θ_{14}, where the $(4f)$ stands for a parameter in a four family model. We study the ν_μ disappearance and the discovery channels in previous section. From eq. (4.3) and eq. (4.4), we can understand that sensitivities to $\theta_{13}^{(4f)}$ and θ_{14} will be weak in these channels because the leading terms in these channels do not include θ_{13} or θ_{14}. On the other hand, the golden channel ($\nu_e \to \nu_\mu$) and the silver channel ($\nu_e \to \nu_\tau$) have the leading terms including θ_{13} or θ_{14} as we discuss it in section 4.1. Thus, we investigate the sensitivities using the golden and the silver channels.

We use the chi squared eq. (4.7) to investigate the sensitivities to θ_{13} and θ_{14} using the golden ($\nu_e \to \nu_\mu$) and the silver ($\nu_e \to \nu_\tau$) channels. We fix the parameters as follows: $\theta_{12} = 34^\circ$, $\theta_{23} = 45^\circ$, $\theta_{13} = 0$, $\Delta m^2_{21} = 7.9 \times 10^{-5}$ eV^2, $\Delta m^2_{31} = 2.4 \times 10^{-3}$ eV^2, $\Delta m^2_{41} = 1$ eV^2, $\delta_1 = 0$, where these parameters are the common values in the three and the four family scheme except θ_{13} and Δm^2_{41}. We generate number of events which is $N_j(4f)$ and

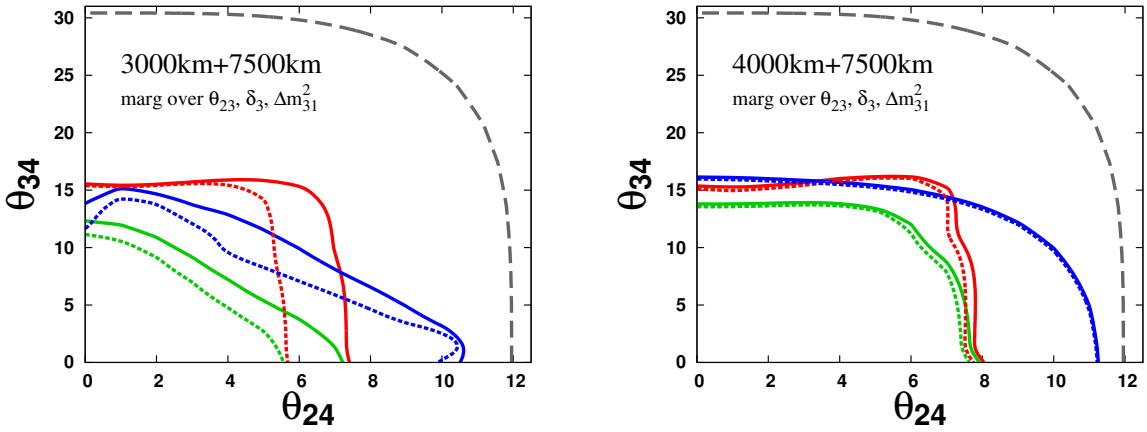

Figure 4.3: The sensitivity limits at 90% C.L. to θ_{24} and θ_{34} for the combination of both the baselines. The blue solid lines, the red solid lines and the green solid lines stand for the discovery channel, the ν_μ disappearance and the combination of both the channels. The dashed gray line stand for the present bound. The dashed lines stand for the sensitivity limits without the correlated systematic errors. The left panel: the 50 GeV Neutrino Factory; The right panel: the 20 GeV Neutrino Factory.

fit number of events N_j^0 with $\Delta m_{41}^2 = 0$ eV^2, $\theta_{13}^{(3f)} = 0$, $\theta_{23} = 45°$, $\theta_{24} = \theta_{34} = \theta_{34} = 0$, $\delta_1 = \delta_2 = \delta_3 = 0$ in the four family scheme.

We marginalize over the active-sterile mixing angles θ_{24} and θ_{34} and obtain the sensitivities to $\theta_{13}^{(4f)}$ and θ_{14} for various fixed values of the CP violating phases.

The fig.4.6 and 4.6 show that differences between the sensitivities to $\theta_{13}^{(4f)}$ and θ_{14} for the baseline length $L = 3000$ km and $L = 7500$ km for only the golden channel and the the combination of the golden and the silver channels. A value of δ_2 which reduces to the three-flavor CP-violating phase in the limit θ_{i4} $(i = 1, 2, 3)$ is fixed to $\delta_2 = 0,\ 90°,\ 180°,\ 270°$. the fig.4.6 and 4.6 show that the sensitivities to $\theta_{13}^{(4f)}$ significantly depend on the CP-violating phase for the shorter baseline. The maximal sensitivity to $\theta_{13}^{(4f)}$ is from $\sin^2 2\theta_{13}^{(4f)} \lesssim 1.5 \times 10^{-5}$ for $\delta_2 = \delta_3 = 0$ to $\sin^2 2\theta_{13}^{(4f)} \lesssim 7 \times 10^{-4}$ for $\delta_2 = \delta_3 = 90°$ with a strong dependence on the value of θ_{14}. For the combination of the golden and the silver channels at $L = 3000$ km baseline, the maximal sensitivity to $\theta_{13}^{(4f)}$ also depends on the CP-violating phases but the dependence on the CP-violating phases for the combination of both the channels is weaker than one for the golden channel only.

The sensitivities to $\theta_{13}^{(4f)}$ and θ_{14} marginalized also over δ_2 and δ_3 are shown in figs.4.6. The fig.4.6 show that the combination of the golden $(\nu_e \to \nu_\mu)$ and the silver $(\nu_e \to \nu_\tau)$ channels constrains $\sin^2 2\theta_{13}^{(4f)} \lesssim 7 \times 10^{-4}$ at the 50 GeV Neutrino Factory for $L = 3000$ km (9×10^{-4} at the 20 GeV Neutrino Factory for $L = 4000$ km). For this baseline length, the correlation errors are important and change the sensitivities. While the combination of these channels constrains $\sin^2 2\theta_{13}^{(4f)} \lesssim 2 \times 10^{-4}$ at the 50 GeV Neutrino Factory (3×10^{-4} at the 20 GeV Neutrino Factory) for $L = 7500$ km. The combination of bath the baselines constrains $\sin^2 2\theta_{13}^{(4f)} \lesssim 7 \times 10^{-5}$ at the 50 GeV Neutrino Factory (2×10^{-4} at the 20 GeV Neutrino Factory).

Figs.4.6 show that these channels are not sensitive to θ_{14}.

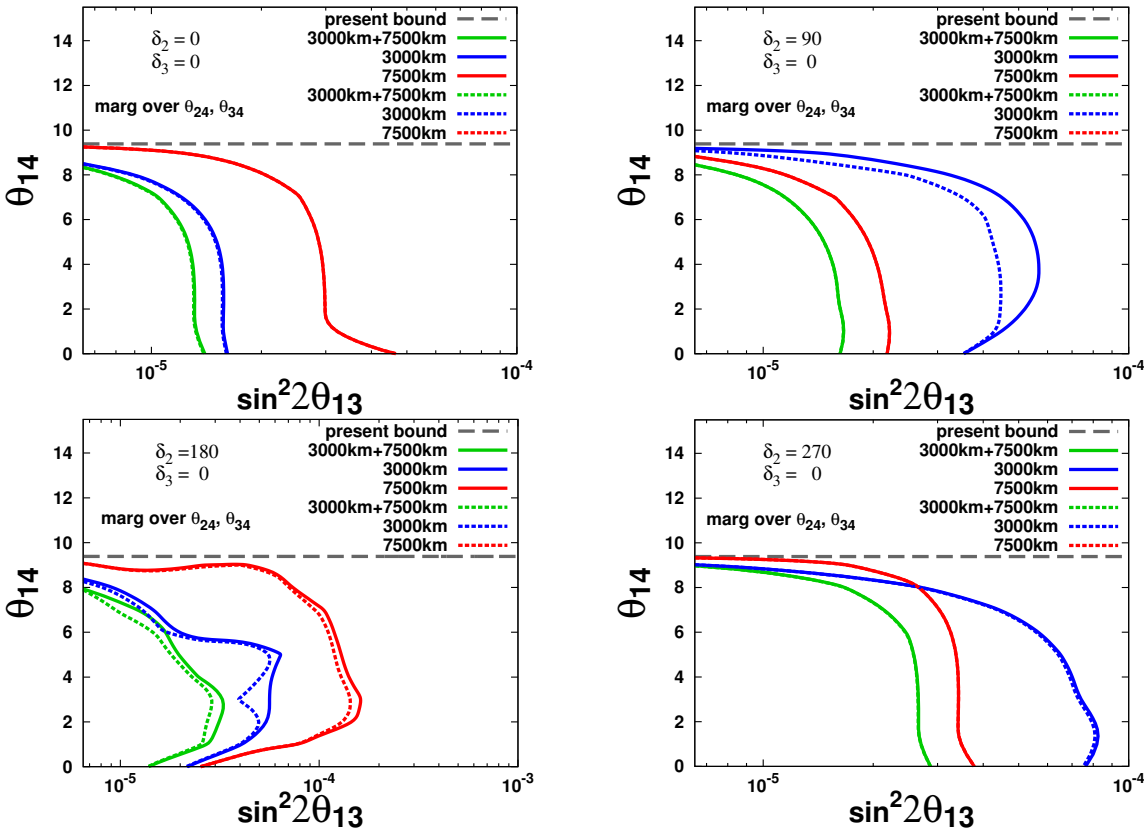

Figure 4.4: Sensitivity limit at 90% CL in the $(\sin^2 2\theta_{13}, \theta_{14})$ plane for $\delta_3 = 0$ and different values of δ_2. The solid lines refer to the golden channel results, only. Dashed lines stand for the sum of golden and silver channel results. The colors are: blue for $L = 3000$ km; red for $L = 7500$ km; green for the combination of the two baselines; the horizontal dashed grey line represents the present bound on θ_{14}.

4.4.2 Sensitivity to $U_{e4}U_{\mu 4}$ and $U_{e4}U_{\tau 4}$

Since sensitivity to θ_{14} at the Neutrino Factory is poor, it is worth investigating whether the Neutrino Factory has sensitivity to other combinations of the mixing matrix elements. From the form of the appearance oscillation probability

$$P(\nu_\alpha \to \nu_\beta) = 4\mathrm{Re}\left[U_{\alpha 3}U^*_{\beta 3}(U^*_{\alpha 3}U_{\beta 3} + U^*_{\alpha 4}U_{\beta 4})\right] \sin^2\left(\frac{\Delta m^2_{31}}{4E}L\right) + \cdots , \tag{4.11}$$

we can expect that the golden and silver channels have some sensitivity to $U_{e4}U_{\mu 4}$ and $U_{e4}U_{\tau 4}$. In the present parametrization (3.16) of the mixing matrix, we have $U_{e4}U_{\mu 4} = s_{14}c_{14}s_{24} = s_{14}s_{24} + \mathcal{O}(\epsilon^6)$ and $U_{e4}U_{\tau 4} = s_{14}c_{14}c_{24}s_{34} = s_{14}s_{34} + \mathcal{O}(\epsilon^5)$, where we have used the fact that s_{14} and s_{24} are small. The sensitivity is defined as in section 4.4.1. The results using the golden and the silver channels are shown in fig.4.7. The right (left) panels show the sensitivities to $U_{e4}U_{\mu 4}$ (upper panel) or $U_{e4}U_{\tau 4}$ (lower panel) at the 50 GeV (20 GeV) Neutrino Factory. They indicate that the combination of the golden and the silver channels has good sensitivity to these variables. Then the upper bound for $\sqrt{U_{e4}U_{\mu 4}}$ by the 50 GeV (20 GeV) Neutrino Factory is 5×10^{-4} (1×10^{-3}) (the current bound $U_{e4}U_{\mu 4} \lesssim 0.02$) and we find that our Neutrino Factory setup can probe the allowed region suggested by the LSND data much more strongly than MiniBooNE does. Similarly, the

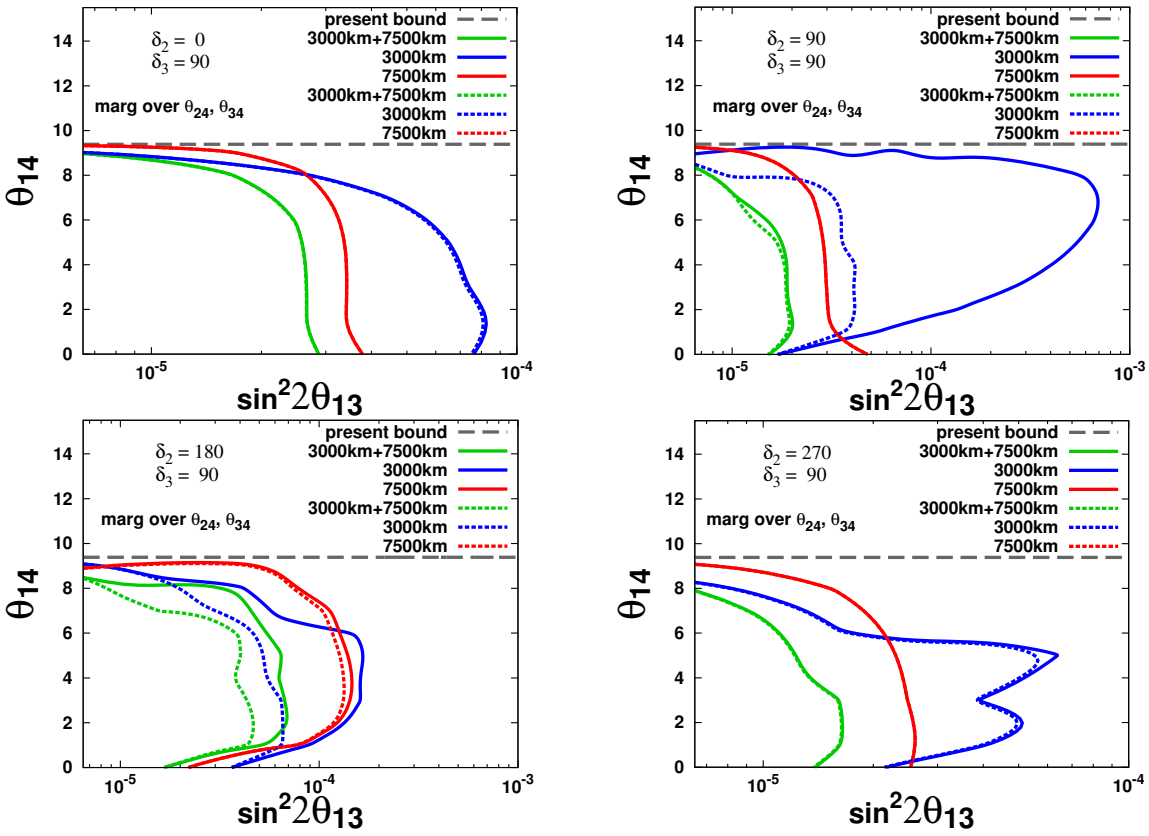

Figure 4.5: Sensitivity limit at 90% CL in the $(\sin^2 2\theta_{13}, \theta_{14})$ plane for $\delta_3 = 90°$ and different values of δ_2. The solid lines refer to the golden channel results, only. Dashed lines stand for the sum of golden and silver channel results. The colors are: blue for $L = 3000$ km; red for $L = 7500$ km; green for the combination of the two baselines; the horizontal dashed grey line represents the present bound on θ_{14}.

upper bound for $U_{e4}U_{\tau 4}$ by both the 50 GeV and the 20 GeV Neutrino Factory is 2×10^{-3} (current bound $U_{e4}U_{\tau 4} \lesssim 0.08$).

For both $U_{e4}U_{\mu 4}$ and $U_{e4}U_{\tau 4}$ plots, we see that both the golden and silver channels play a role in giving the constraints. As it is expected from statistics, the result by the 50 GeV Neutrino Factory is better for $U_{e4}U_{\mu 4}$, but the sensitivity to $U_{e4}U_{\tau 4}$ is almost the same for the two setups (notice that the scale on the vertical axis for the left and right panels are different). For the 20 GeV case, the data at 7500 km perform very well and the combined data of 4000 km and 7500 km give a result almost comparable to that of the 50 GeV case.

It is interesting to note that the golden channel also plays a role in improving sensitivity to $U_{e4}U_{\tau 4}$. We can obtain the analytic formula for the golden channel in matter which is eq.(A.8). We will find that the θ_{34} dependence of the golden channel appears through the matter effect. This explains why the golden channel has some sensitivity to $U_{e4}U_{\tau 4}$.

4.5 Discovery potential of the four family scheme

In the section 4.3 and 4.4.1, we discussed the sensitivity to θ_{13}, θ_{14}, θ_{24} and θ_{34} by looking at statistical significance of deviation from the four family scheme from that with a certain

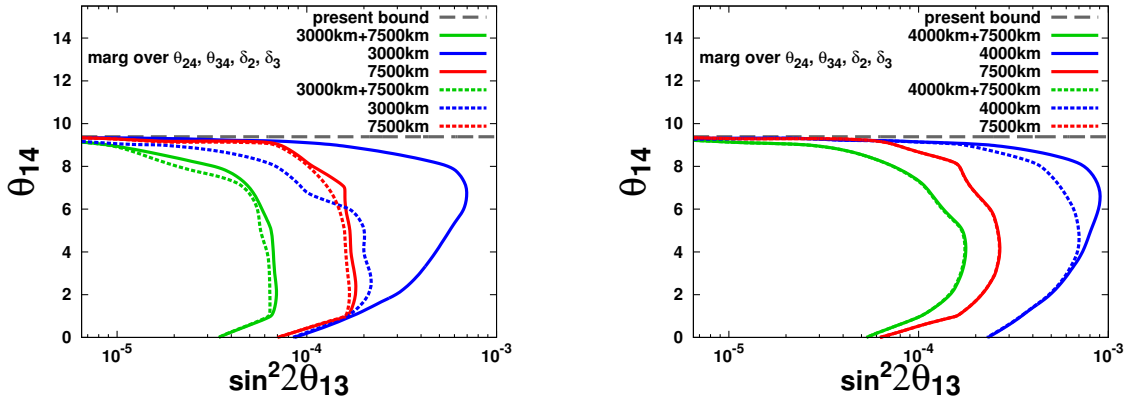

Figure 4.6: Sensitivity limit at 90% CL in the $(\sin^2 2\theta_{13}, \theta_{14})$ plane, marginalizing over $\theta_{24}, \theta_{34}, \delta_2$ and δ_3. The solid lines refer to the golden channel results, only. Dashed lines stand for the sum of golden and silver channel results. The colors are: blue for the shortest baseline; red for longest baseline; green for the combination of the two baselines; the horizontal dashed grey line represents the present bound on θ_{14}. Left panel: 50 GeV Neutrino Factory; Right panel: 20 GeV Neutrino Factory.

parameters. In this section, we will discuss whether the Neutrino Factory setup which is discussed in the section 4.2 can distinguish the four family scheme from the three family scheme.

We define the four family scheme discovery potential as follows:

$$\Delta\chi^2(4f) = \min_{marg\ par}\left[\sum_{pol.,chan.,L}\min_{\alpha_{s,b},\beta_{s,b}}\left\{\sum_i \frac{1}{\sigma_i^2}\Big((1+\alpha_s+x_i\beta_s)N_i(3f)+(1+\alpha_b+x_i\beta_b)B_i(3f) - N_i(4f)-B_i(4f)\Big)^2+\left(\frac{\alpha_s}{\sigma_{\alpha s}}\right)^2+\left(\frac{\alpha_b}{\sigma_{\alpha b}}\right)^2+\left(\frac{\beta_s}{\sigma_{\beta s}}\right)^2+\left(\frac{\beta_b}{\sigma_{\beta b}}\right)^2\right\}+\Delta\chi^2_{prior}\right], \tag{4.12}$$

where the i stand for the i-th bin grouping events in ten (four) constant energy resolution bins of width $\Delta E_\nu = 4$ GeV from 1 GeV to 5 GeV and $\Delta E_\nu = 5$ GeV from 5 GeV to 50 GeV (20 GeV) at the 50 GeV (20GeV) Neutrino Factory. $N_i(4f)$ stands for number of events within i-th bin four family scheme.

We generate number of events which is $N_i(3f) + B_i(3f)$ in the three family scheme and fit the number of events $N_i(4f) + B_i(4f)$ in the four family scheme.

The variance is defined by

$$\sigma_i^2 = N_i(4f) + B_i(4f) + [f_i N_i(4f)]^2 + [f_i B_i(4f)]^2, \tag{4.13}$$

where f_i stands for the uncorrelated bin-to-bin systematic error in the i-th bin; $f_i = 2\%$ for the golden channel, $f_i = 10\%$ for the silver channel, $f_i = 5\%$ for the ν_μ disappearance channel and $f_i = 10\%$ for the discovery channel. $\Delta\chi^2_{prior}$ are the prior contributed by the solar and the atmosphere neutrino observations and the reactor and the accelerator

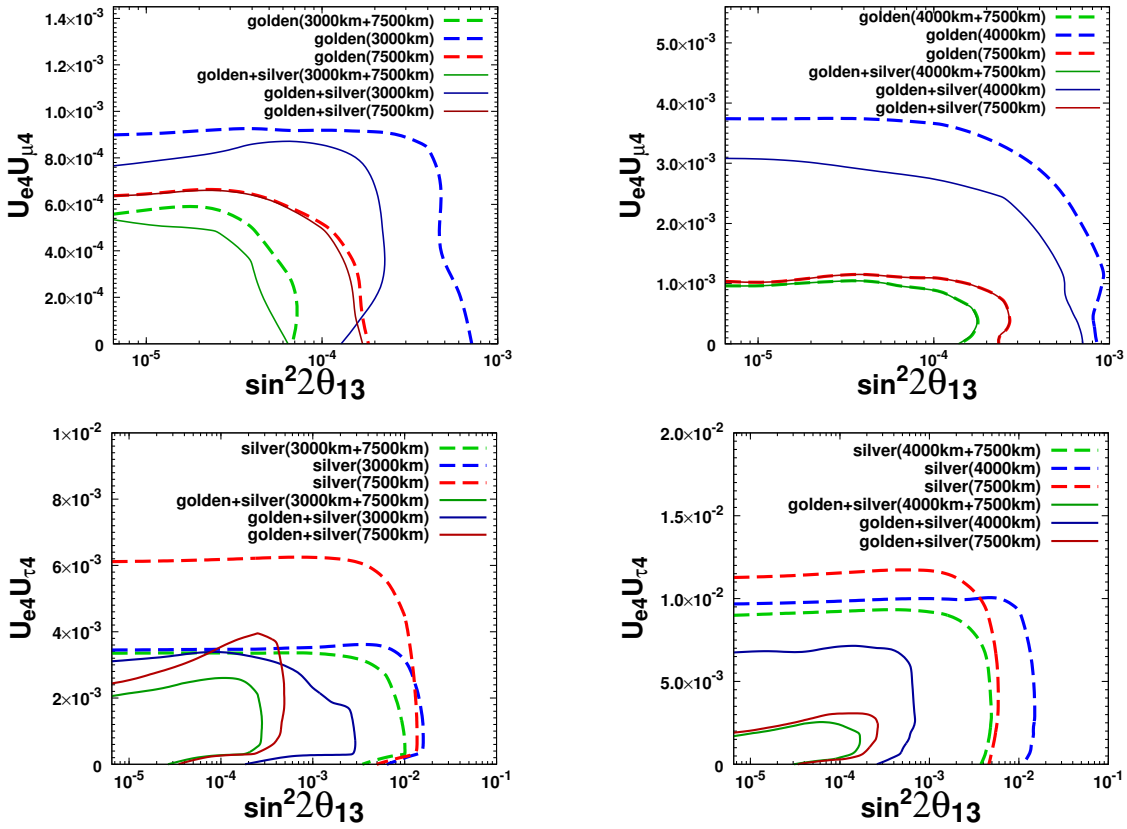

Figure 4.7: Sensitivity limit at 90% CL to $U_{e4}U_{\mu 4}$ and $U_{e4}U_{\tau 4}$. $\Delta\chi^2$ is evaluated for a fixed set of values of $(\sin^2 2\theta_{13}, U_{e4}U_{\mu 4})$ (upper panels) or a fixed set of values of $(\sin^2 2\theta_{13}, U_{e4}U_{\tau 4})$ (lower panels), marginalizing over $s_{14}/s_{24}, \theta_{34}, \delta_2$ and δ_3 (upper panels), or over $s_{14}/s_{34}, \theta_{24}, \delta_2$ and δ_3 (lower panels). Left panels: 50 GeV Neutrino Factory; Right panels: 20 GeV Neutrino Factory. The current bound on $U_{e4}U_{\mu 4}$ ($U_{e4}U_{\tau 4}$) is 0.02 (0.06).

neutrino experiments which is defined as follows:

$$\begin{aligned}\Delta\chi^2_{prior} &= \frac{(s^2_{23}(4f)-0.50)^2}{(\sigma^2(s^2_{23}))}+\frac{(|\Delta m^2_{31}(4f)|-2.4\times10^{-3}\ \mathrm{eV}^2)^2}{\sigma^2(|\Delta m^2_{31}|)}\\ &+\frac{(s^2_{13}(4f)-0.01)^2}{\sigma^2(s^2_{13})}+\frac{s^2_{14}}{\sigma^2(s^2_{14})}+\frac{s^2_{24}}{\sigma^2(s^2_{24})}+\frac{s^2_{34}}{\sigma^2(s^2_{34})}\end{aligned} \tag{4.14}$$

and

$$\begin{aligned}\sigma(s^2_{23}) &= 0.07, \quad \sigma(|\Delta m^2_{atm}|)=0.12\times10^{-3}\ \mathrm{eV}^2, \quad \sigma(s^2_{13})=0.016\\ \sigma(s^2_{14}) &= 0.013, \quad \sigma(s^2_{24})=0.02, \quad \sigma(s^2_{34})=0.12.\end{aligned} \tag{4.15}$$

The definition (4.12) is slightly different from the definition (4.7) although it looks similar. In section 4.3 and 4.4.1, we assume that the minimum of $\chi^2_{min}(4f)$ correspond to the true values of the four-flavor-scheme parameters which means $\chi^2_{min}(4f)=0$. $\Delta\chi^2(4f)$ is then calculated in the same model. In this section, we generate data in the four family model but we try to fit them in the three family model. The minimum of $\Delta\chi^2_{min}(4f)$ in the four family scheme is located at the true values of the parameters and $\chi^2_{min}(4f)=0$.

On the other hand, $\chi^2_{min}(3f)$ will not generally be zero because of a wrong model to fit the data except for the special case defined by $\theta_{i4} = 0$ $(i = 1, 2, 3)$, $\theta^{(4f)}_{ij} = \theta^{(3f)}_{ij}$ $(i, j = 1, 2, 3)$, $\Delta m^{2\ (4f)}_{k1} = \Delta m^{2\ (3f)}_{k1}$ $(k = 2, 3)$ which means that the two model coincide and $\Delta\chi^2 = 0$. In the rest of the four family parameter space, $\Delta\chi^2$ defined in eq.(4.12) corresponds to $\chi^2_{min}(3f) - \chi^2_{min}(4f)$. CL contour define, then, regions in the four parameter space for which a three-flavor fit to the data is worse than a four-flavor fit to the the data of a quantity $\Delta\chi^2$. For example, a point with $\Delta\chi^2 = 4.61$ is a point that is fitted by the four family model much better than by three family model. We will define points outside this contour as points for which the hypothesis that data can be fitted in the three family model is "excluded at 90 % CL". Under these premises, we can use eq.(4.12) to determine regions in which we are able to distinguish four family models from three family ones in the four family parameter space in the same manner as in the section 4.3 and 4.4.1.

Since the excluded region is expected to depend little on the solar neutrino oscillation parameters in the three-flavor scheme, we will not marginalize $\Delta\chi^2$ with respect to $\theta^{(3f)}_{12}$ and $\Delta m^{2\ (3f)}_{21}$ in eq.(4.12). Moreover, while $\Delta\chi^2$ is naively expected to depend on all of the parameters $\theta^{(3f)}_{13}$, $\theta^{(3f)}_{23}$, $|\Delta m^{2\ (3f)}_{31}|, \delta^{(3f)}$ we have found numerically that it suffices to vary some of the parameters and put other parameters to the best-fit values in most analyses. Namely, in the case of the golden and silver (disappearance and discovery) channels, a dominant role is played by $\theta^{(3f)}_{13}$ and $\theta^{(3f)}_{23}$ ($\theta^{(3f)}_{23}$ and $|\Delta m^{2\ (3f)}_{31}|$) which are the only three family parameters that we vary, and the other three family ones are fixed in the analysis.1440

To compare the results with those in the section 4.3 and 4.4.1, we project the excluded region either in $(\theta^{(4f)}_{13}, \theta_{14})$ plane or in $(\theta_{24}, \theta_{34})$ plane. In these projections, we would like to obtain the most conservative excluded region, i.e., the common excluded region in $(\theta_{24}, \theta_{34})$ plane irrespective of the values of $\theta^{(4f)}_{13}$ and θ_{14}, or the common excluded region in $(\theta^{(4f)}_{13}, \theta_{14})$ plane irrespective of the values of θ_{24} and θ_{34}. Notice that the four angles can in principle be measured simultaneously if we use informations from the four channels at the same time. To obtain them, we have to marginalize $\Delta\chi^2$ not only with respect to the three family parameters described above but also with respect to the four family ones, such as $\theta^{(4f)}_{12}$, $\theta^{(4f)}_{23}, \Delta m^{2\ (4f)}_{21}$, $|\Delta m^{2\ (4f)}_{31}|, \delta_1$, δ_2, δ_3 as well as $(\theta_{24}, \theta_{34})$ in the former case and $(\theta^{(4f)}_{13}, \theta_{14})$) in the latter. In marginalizing over the four family parameters, however, we do not have to vary all the parameters for a couple of reasons. First of all, since the excluded region is expected to depend little on the solar neutrino oscillation parameters in the four family scheme, we can fix the solar parameters $\theta^{(4f)}_{12}$, $\Delta m^{2\ (4f)}_{21}$, δ_1. Secondly, because of the prior $\Delta\chi^2_{prior}(4f)$, in practice we can fix the following parameters to the best fit values: $s^{2\ (4f)}_{13} \simeq 0.01$, $s^{2\ (4f)}_{23} \simeq 0.5$, $|\Delta m^{2\ (4f)}_{31}| \simeq 2.4 \times 10^{-3}$ eV^2, $(\theta_{24}, \theta_{34}) \simeq (0, 0)$ in the case of $(\theta^{(4f)}_{13}, \theta_{14})$ plane, and $(\theta^{(4f)}_{13}, \theta_{14}) \simeq (5.7^\circ, 0)$ in the case of $(\theta_{24}, \theta_{34})$ plane. Thus, the only non-trivial four-family parameters to be marginalized over are δ_2 and δ_3 in the case of $(\theta^{(4f)}_{13}, \theta_{14})$ plane, and δ_3 in the case of $(\theta_{24}, \theta_{34})$ plane.

The results are shown in fig.4.8. Upper panels show the sterile neutrinos discovery potential of the combination of the golden and the the silver channels and lower panels the discovery potential of the combination of the ν_μ disappearance and the discovery channels. On the left, we show results obtained for the 50 GeV Neutrino Factory; for the 20 GeV Neutrino Factory on the right. The dashed gray line stands for region which is excluded by the present data of the atmospheric and the reactor experiments. The results show that we can hardly distinguish the four family scheme from the three family one

using the golden and the silver channels if θ_{24} and θ_{34} are small for $\theta_{24} \simeq \theta_{34} \simeq 0$ for both the 50 GeV and the 20 GeV Neutrino Factory. However, if θ_{24} is relatively large, we can search the sterile neutrino using the golden and the silver channels. For example, we can search it down to $\theta_{13}^{(4f)} \simeq 5^\circ$ and $\theta_{14} \approx 0.1^\circ$ for the 50 GeV Neutrino Factory and down to $\theta_{14} \simeq 1^\circ$ for the 20 GeV Neutrino Factory in the case of $\theta_{24} = 10^\circ$ and $\theta_{34} = 0$. On the other hand, the ν_μ disappearance and the discovery channels are useful to search a sterile neutrino because we can distinguish the four family scheme from three family one down to $\theta_{24} \simeq 7^\circ(7.5^\circ)$ and $\theta_{34} \simeq 13^\circ(15^\circ)$ which are half values of the present bound at the 50 GeV (20 GeV) Neutrino Factory for any value of $\theta_{13}^{(3f)} = \theta_{13}^{(4f)}$ and θ_{14}. Thus, we can find that the ν_μ disappearance and the discovery channels are useful to search a sterile neutrino at both the 50 GeV and 20 GeV Neutrino Factories.

4.6 Dependence of the sensitivities on systematic errors

In this section, we will investigate the dependence of the sensitivities on the systematic errors. In the section 4.4.1 and 4.3, we can find that the ν_μ disappearance and the discovery channels are sensitive to the active-sterile mixing angles in contrast with the golden and the silver channels. In section 4.3, the systematic errors are chosen by $f_i = 0.05$ (0.1), $\sigma_\alpha = 0.01$ (0.01) and $\sigma_\beta = 0.05$ (0.05) for the ν_μ disappearance channel (the discovery channel). However, these values are not completely fixed yet and may be changed in future.

The dependence of the sensitivities to θ_{24} and θ_{34} on the systematic errors are shown in fig.4.9. The values of the systematic errors are taken as follows: $f_i \equiv f_{\mu\mu} = 0.05,\ 0.02$, $\sigma_\alpha = 0.1,\ 0.05,\ 0.025,\ 0.01$ for the ν_μ disappearance channel and $f_i \equiv f_{\mu\tau} = 0.1,\ 0.03$, $\sigma_\alpha = 0.1,\ 0.05,\ 0.01$ for the discovery channel. The MECC mass is also taken as 4 kton or 8 kton. Because σ_β dependence of the sensitivities are small, we fix $\sigma_\beta = 0.05$. We can find that the sensitivity to θ_{34} is not significantly changed by a value of $f_{\mu\mu}$ and σ_α for the ν_μ disappearance channel. On the other hand, for the discovery channel, the sensitivity to θ_{34} is changed by the values of the systematic errors and we can find that the discovery channel is more sensitive to θ_{34} than the ν_μ disappearance channel for $f_{\mu\mu} = 0.05$ and $\sigma_\alpha = 0.01$ in the case of $f_{\mu\tau} = 0.1$ and $\sigma_\alpha = 0.01$, or $\mathrm{f}_{\mu\tau} \leq 0.03$ and $\sigma_\alpha \leq 0.05$ at the 50 GeV Neutrino Factory (in the case of $f_{\mu\tau} \leq 0.03$ and $\sigma_\alpha \leq 0.05$ at the 20 GeV Neutrino Factory). However, we can check that the sensitivity to θ_{34} is not significantly changed by a value of σ_α which is less than 0.025 in the case of $f_{\mu\tau} = 0.03$ for 4 kton MECC mass and a value of σ_α which is less than 0.01 in the case of $f_{\mu\tau} = 0.03$ for 8 kton MECC mass. For a lager mass of the MECC, the sensitivities change but do not significantly change. If we take a MECC mass which is greater than 8 kton, can also check that the sensitivities change little.

4.7 CP violation in four flavor neutrinos

In this section, we will present an analysis of the sensitivities to the CP-violating phases in our setup. The eq.(4.3) and the eq.(4.4) show that we can find a CP violation using the ν_μ disappearance and the discovery channels because the CP-violating phase δ_3 which is

not included in the three family scheme may appears in ϵ^3 terms. The discovery channel particularly has both of $\cos\delta_3$ and $\sin\delta_3$ terms, i.e., any value of δ_3 will contribute the transition probability of the discovery channel if θ_{24} or θ_{34} are not small.

We first analyze the sensitivity to the mixing angle θ_{34} and the CP-violating phase δ_3 with two representative values of θ_{24}. Notice that δ_3 terms are proportional to $s_{24}s_{34}$ in the eq.(4.3) and eq.(4.4). We show the sensitivity at 99 % CL for particular input pairs (θ_{34}, δ_3) for fixed non-vanishing values of θ_{24}. We will not address within a comprehensive approach the problem of degeneracies in four-family models. Notice that this problem, extremely severe in the three-family oscillation studies at the Neutrino Factory (see, for example, refs.[97, 137] and [149]), is expected to be even more complicated in a four-neutrino model. In the particular case of the δ_3-dependent CP-violating signal, that can be extracted using the $\nu_\mu \to \nu_\mu$ and $\nu_\mu \to \nu_\tau$. channels, we do expect to observe at least degeneracies due to the (θ_{34}, δ_3)-correlation (the so-called "intrinsic degeneracies", [97]); those dependent on the wrong reconstruction of the sign of the atmospheric mass difference Δm^2_{31} (known as "sign degeneracies", [98]); and those dependent on a wrong reconstruction of the "atmospheric" mixing angle θ_{23} octant (known as "octant degeneracies", [136]).

The $\Delta\chi^2$ to analyze the sensitivity to θ_{34} and δ_3 is defined as follows:

$$\Delta\chi^2 = \sum_i \left[\frac{\left(N_i(\bar{\theta}_{24}, \theta_{34}, \delta_3) - N_i(\bar{\theta}_{24}, \bar{\theta}_{34}, \bar{\delta}_3)\right)^2}{\sigma_i} \right], \tag{4.16}$$

where $\bar{\theta}_{24(34)}$ and $\bar{\delta}_3$ are fixed values. The minimum of the $\Delta\chi^2$ is, trivially, obtained for $\theta_{34} = \bar{\theta}_{34}$. As in previous sections, i runs over the different signals: the ν_μ disappearance and the discovery channels data, divided into 10 energy bins, for the two baselines and the two possible stored muons polarities. The variance σ_i is defined by eq.(4.13), with $f_i = 5\%$ for the ν_μ disappearance channel and 10% for the discovery channel. No correlated systematic errors have been considered in the plots of this section. The region in the (θ_{34}, δ_3)-plane compatible with the input values (θ_{34}, δ_3) at the 2 d.o.f.'s 99% CL is finally defined by drawing the contour line corresponding to $\Delta\chi^2 = 9.21$.

Fig.4.10 show the sensitivity to θ_{34} and δ_3 using the combination of the ν_μ disappearance and the discovery channels, where the two representative value for θ_{24} have been assumed: $\bar{t}_{24} = 3^\circ$ or 5°.

The following parameters in the four family model have been also kept fixed to their central values: $\theta_{12} = 34^\circ$, $\theta_{13} = 0$, $\Delta m^2_{21} = 7.9 \times 10^{-5}$ eV^2, $\Delta m^2_{31} = 2.4 \times 10^{-3}$ eV^2, $\delta_1 = \delta_2 = 0$. For simplicity, we have fixed $\theta_{23} = 45^\circ$. We do not expect any "octant degeneracies". The input values that we have studied to illustrate the discovery potential of our setup are: $\bar{\theta}_{34} = 20^\circ,\ 30^\circ$, $\bar{\delta}_3 = 90^\circ$ (upper panels) and $\delta_3 = 200^\circ$ (lower panels). Matter effects have been included considering, as always, a constant matter density $\rho_e = 3.4$ g/cm^3 for the shortest baseline and $\rho_e = 4.3$ g/cm^3 for the longest one, computed averaging over the density profile in the PREM [114] along the neutrino path. First of all, we can see that the combination of the two channels at the shortest baseline (blue lines) is not enough to solve the sign degeneracies (labeled with "SD" in the plot), that can be observed for all of the choices of the three input parameters $(\bar{\theta}_{24}, \bar{\theta}_{34}, \bar{\delta}_3)$. The sign clones are located at the point $(\theta^{SD}_{34}, \delta^{SD}_3)$, where $\theta^{SD}_{34} = \bar{\theta}_{34}$ and δ^{SD}_3 satisfies the relation $\sin\bar{\delta}_3 \sin(\Delta m^2_{31} L/(4E)) = -\sin\delta^{SD}_3 \sin(\Delta m^2_{31} L/(4E))$ with $\delta^{SD}_3 \sim 90^\circ$ for $\bar{\delta}_3 = 90^\circ$ and $\delta^{SD}_3 \sim 20^\circ$ for $\bar{\delta}_3 = 200^\circ$. The intrinsic degeneracy is also found for one specific choice of the input parameter $(\bar{\theta}_{24} = 3^\circ, \bar{\theta}_{34} = 20^\circ, \bar{\delta}_3 = 200^\circ)$. On the other hand, no intrinsic

or sign degeneracy are found at the longest baseline (red lines). When combining the two baselines we see that the degeneracies are solved and that a very good precision on the simultaneous measurement of θ_{34} and δ_3 is achieved for all the choices of the input parameters that we have considered. In particular, the error in δ_3 at the 99% CL is of the order of a few tens of degrees. At the same time, the mixing angle θ_{34} can be Δm^2_{41} measured for these particular inputs with a precision of a few degrees. We summarize our results for the simultaneous measurement of θ_{34} and δ_3 in fig.4.11, where the 99% CL "δ_3-discovery potential" in the (θ_{34}, δ_3)-plane for different values of $\bar{\theta_{24}}$ is shown. We defined the "δ_3-discovery potential" as the region in the $(\sin^2 2\theta_{34}, \delta_3$-plane for which a given (non-zero) value of the CP-violating phase δ_3 can be distinguished at the 99% CL from the CP-conserving case, i.e., $\delta_3 = 0, \pi$. In the left panel the results using the ν_μ disappearance channel are shown and in the right panel the results using the combination of the ν_μ disappearance and the discovery channels are shown. The upper panels refer to $\bar{\theta}_{24} = 3°$; lower panels refer to $\bar{\theta}_{24} = 5°$. Blue dashed lines stand for the $L = 3000$ km baseline; red dashed lines stand for $L = 7500$ km baseline; Black dashed lines stand for the combination of the two baselines.

We can see from fig.4.11(left) that, using ν_μ disappearance channel only, we are able to measure a non-vanishing δ_3 for values of θ_{34} above $\sin^2 2\theta_{34} \geq 0.4(\theta_{34} \geq 18°)$. The CP-coverage is $\sim 50\%$, with a very smooth dependence on θ_{34}, being a bit larger for larger θ_{24}. We can also see that the detector at $L = 3000$ km have no δ_3-sensitivity whatsoever. The situation is completely different when the discovery channel data are added to the ν_μ disappearance channel, fig.4.11(right). first of all, we see that the $L = 3000$ km detector is no longer useless to measure δ_3; spikes of δ_3-sensitivity for particular values of δ_3 can be observed, in some cases outperforming the far detector results. However, it is in the combination of the two baselines where we can see that a dramatic improvement in the δ_3-discovery potential is achievable. When the $\nu_\mu \to \nu_\tau$ data are included, a non-vanishing δ_3 can be measured for values of θ_{34} as small as $\sin^2 2\theta_{34} = 0.06(\theta_{34} = 7°)$ for $\bar{\theta}_{24} = 5°$ and $\sin^2 2\theta_{34} = 0.10(\theta_{34} = 9°)$ for $\bar{\theta}_{24} = 3°$. For $\sin^2 2\theta_{34} \geq 0.4(\theta_{34} \geq 20°)$, roughly 80% (60%) of CP-coverage is achieved for $\bar{\theta}_{24} = 5°(3°)$. The striking improvement in the δ_3-discovery potential is a consequence of the synergy of the two channels and of the two baselines, whose combination is able to solve most of the correlations that otherwise strongly limits the potential of the ν_μ disappearance channel.

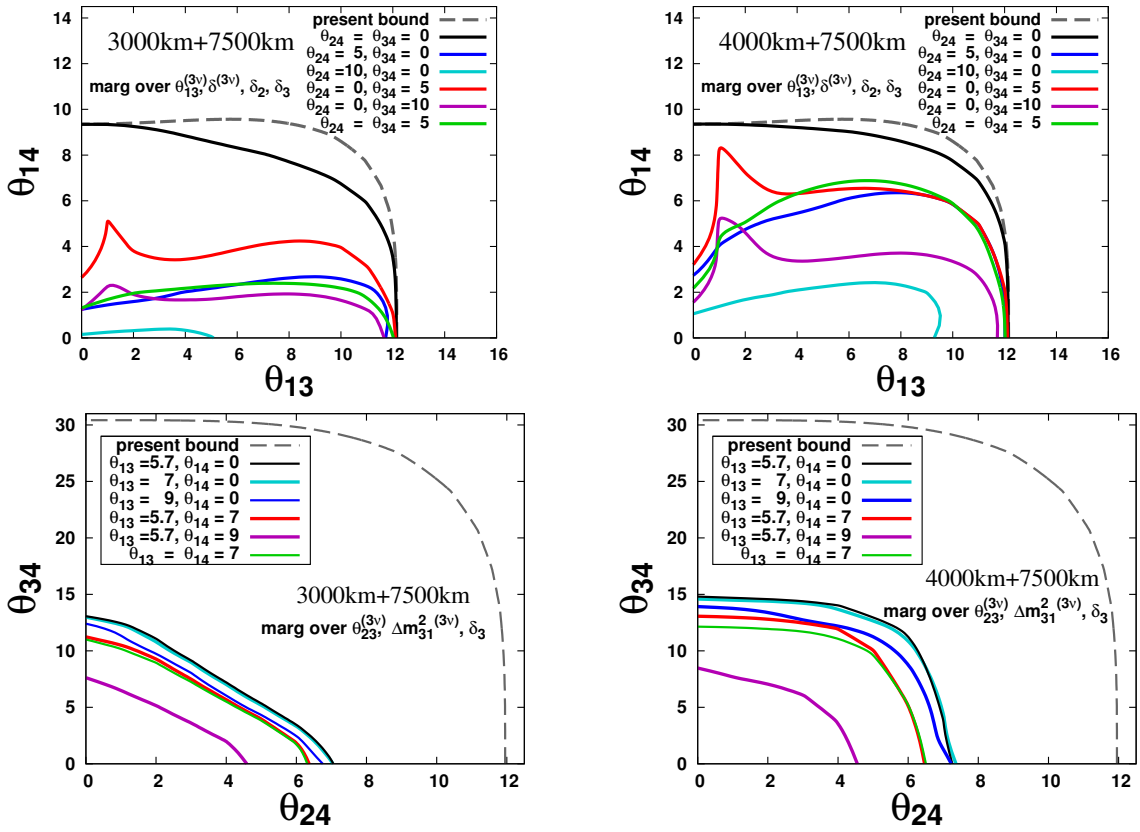

Figure 4.8: Left-upper panel: The right upper part of each line is the region projected onto the $(\theta_{13}, \theta_{14})$ plane, in which the hypothesis of the three flavor scheme is excluded at 90% CL at the 50 GeV Neutrino Factory. It is obtained by marginalizing over $\theta_{13}^{(3f)}$ and $\delta^{(3f)}$ as well as δ_2 and δ_3. The grey dashed lines stand for the excluded region obtained only from the prior $\Delta\chi^2_{prior}$ where terms other than $(s^2_{13}{}^{(4f)} - 0.01)^2/\sigma^2(s^2_{13}) + (s^2_{14})^2/\sigma^2(s^2_{14})$ are assumed to be zero in eq.(4.9). The excluded regions for nonvanishing θ_{24} or θ_{34}, which are always larger than the case for $\theta_{24} = \theta_{34} = 0$, are also depicted for informations. Left- -lower panel: Excluded region at 90% CL projected onto the $(\theta_{24}, \theta_{34})$ plane. It is obtained by marginalizing over $\theta_{23}^{(3f)}$, $|\Delta m^2_{31}{}^{(3f)}|$ as well as δ_3. The grey dashed lines stand for the excluded region obtained only from the prior $\Delta\chi^2_{prior}$ where terms other than $(s^2_{24})^2/\sigma^2(s^2_{24}) + (s^2_{34})^2/\sigma^2(s^2_{34})$ are assumed to be zero in eq.(4.9). Right-upper(lower) panel: The same figure as the left-upper(lower) panel for the 20 GeV ISS-inspired setup.

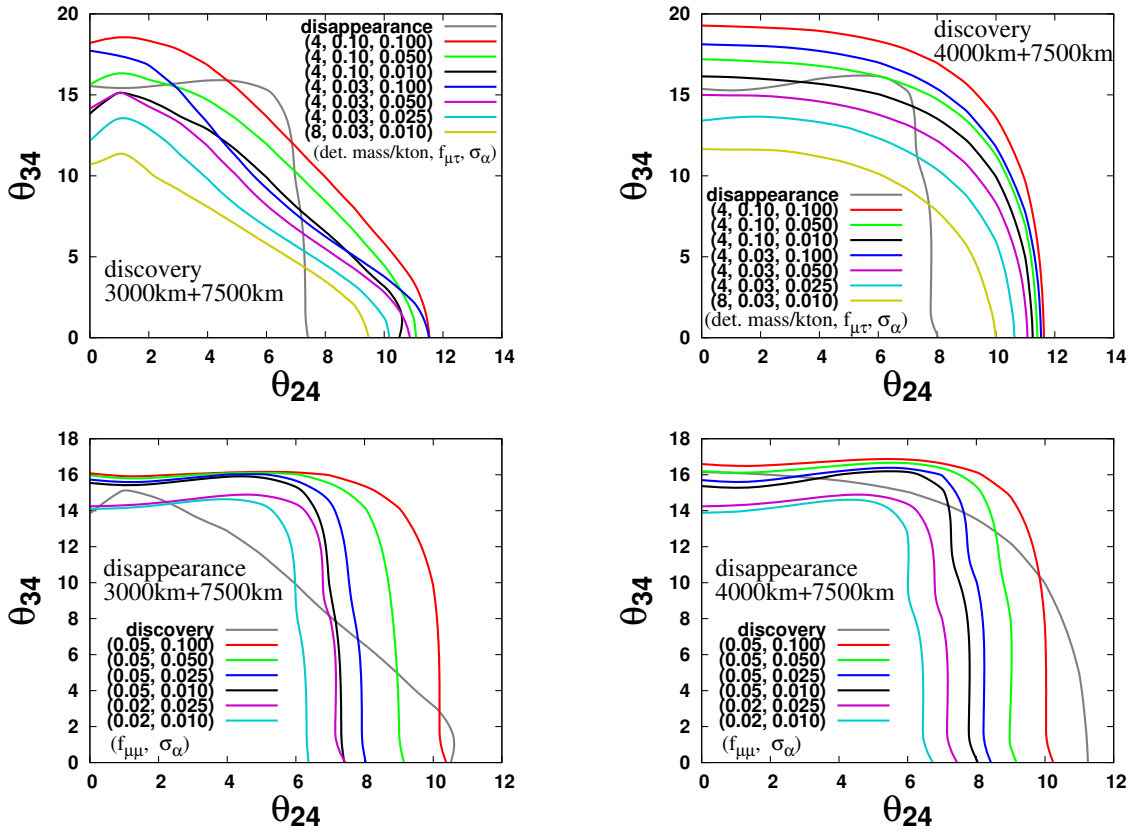

Figure 4.9: The 90%CL sensitivity to $(\theta_{24}, \theta_{34})$ using $\nu_\mu \to \nu_\tau$ (the upper panels) and $\nu_\mu \to \nu_{mu}$ (the lower panels) channels for different values of the uncorrelated bin-to-bin systematic error $f_j \equiv f_{\mu\tau} = 0.1, 0.03$ and $f_j \equiv f_{\mu\mu} = 0.05, 0.02$, of the correlated systematic error on the overall normalization $\sigma_{\alpha_s} = 0.1, 0.05, 0.025, 0.01$ and of the MECC mass (= 4, 8 kton in the case of $\nu_\mu \to \nu_\tau$). Left panels: at the 50 GeV setup; Right panels: at the 20 GeV ISS-inspired setup. In all the figures black lines stand for the excluded region for the reference values used in the calculations in other sections. The grey lines stand for the excluded region using the disappearance (discovery) channel with $f_{\mu\mu} = 0.05,\ \sigma_{\alpha_s} = 0.01$ (with 4 kton, $f_{\mu\tau} = 0.1,\ \sigma_{\alpha_s} = 0.01$).

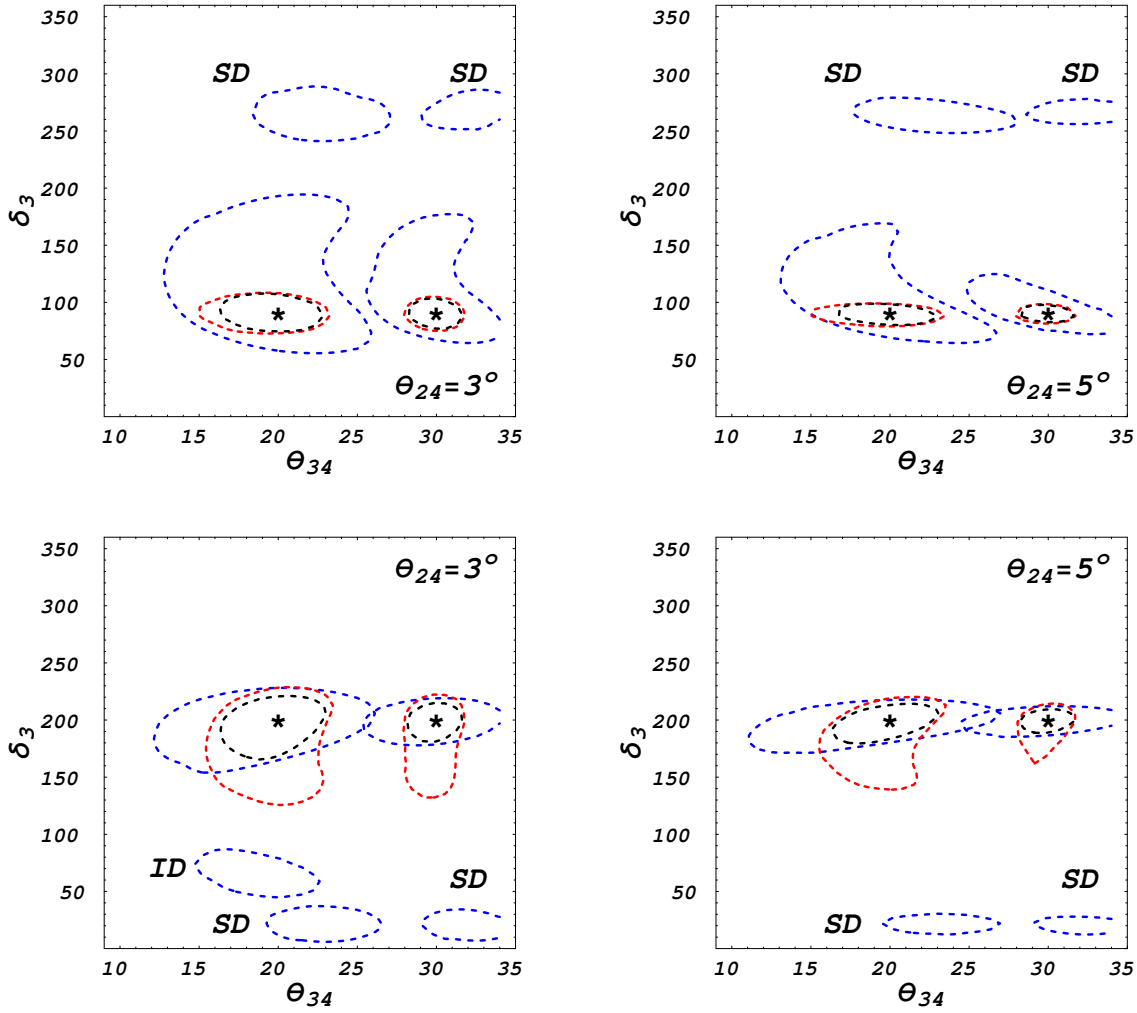

Figure 4.10: 99% CL contours for the simultaneous measurement of θ_{34} and δ_3 using the combined data from the ν_μ disappearance and the $\nu_\mu \to \nu_\tau$ discovery channels. Two different values of θ_{24} have been considered: $\theta_{24} = 3°$ (left panels); $\theta_{24} = 5°$ (right panels). The input pairs $(\bar{\theta}_{34}, \bar{\delta}_3)$, marked by a star in the plots, are: $\bar{\theta}_{34} = 20°, 30°$; $\bar{\delta}_3 = 90°$ (upper panels) and 200° (lower panels). In the plots, "ID " stands for "Intrinsic Degeneracy "; "SD " stands for "Sign Degeneracy ". Blue dashed lines represent the $L = 3000$ km baseline data; red dashed lines the $L = 7500$ km baseline data; black dashed lines stand for the combination of both baselines.

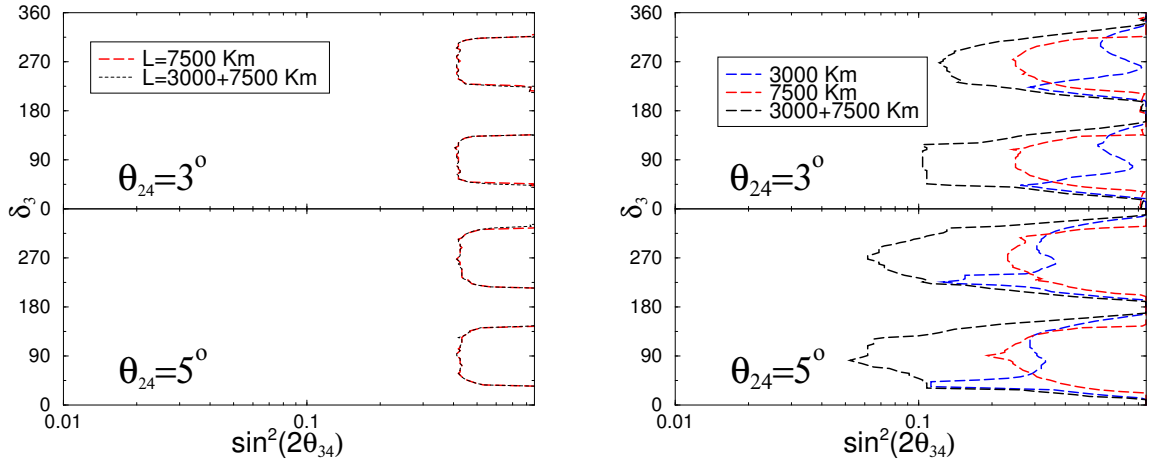

Figure 4.11: The 99 % CL δ_3-discovery potential in the (θ_{34}, δ_3)-plane. Left: only the ν_μ disappearance channel data; Right: combination of the ν_μ disappearance and the $\nu_\mu \to \nu_\tau$ discovery channels data. Upper panels have been obtained for $\bar{\theta}_{24} = 3°$; lower panels for $\bar{\theta}_{24} = 5°$. Blue dashed lines stand for $L = 3000$ km baseline data; red dashed lines stand for $L = 7500$ km baseline data; black dashed lines stand for the combination of the two baselines.

Chapter 5

Conclusion

In this thesis, we reviewed three-family and four-family neutrino neutrino oscillations and discussed phenomenology of (3+1) sterile neutrino models at a Neutrino Factory. As we reviewed in the section 3.3, the current experimental bound of the active-sterile mixing angle θ_{34} is week. On the other hand, as we discussed in the section 4.1, tau neutrino detections at a long baseline oscillation experiment such as a Neutrino Factory give us potential to search for the mixing angle θ_{34}. In the section 4.3, we discussed the sensitivity to θ_{24} and θ_{34} using the ν_μ disappearance ($\nu_\mu \to \nu_\mu$) and the discovery ($\nu_\mu \to \nu_\tau$) channels. We have found that the discovery channel is sensitive to θ_{34} for $L = 3000$ km and $L = 7500$ km baseline length. For $L = 7500$ km baseline length, the ν_μ disappearance channel is also sensitive to θ_{34} through matter potential. We have shown that the combination of both the baselines and of both the ν_μ disappearance and the discovery channels can search the mixing angles θ_{34} down to around 12° (14°) and θ_{24} down to around 7° (8°) at the 50 GeV (20 GeV) Neutrino Factory.

The sensitivity to θ_{13} and θ_{14} using the golden ($\nu_e \to \nu_\mu$) and the silver ($\nu_e \to \nu_\tau$) channels are discussed in the section 4.4.1. The combination of both the baselines and the golden and the silver channels can search the mixing angles $\sin^2 2\theta_{13}$ down to 7×10^{-5} (2×10^{-4}) at the 50 GeV (20 GeV) Neutrino Factory but the both the channels are not sensitive to the active-sterile mixing angle θ_{14}. On the other hand, as we discussed in the section 4.4.2, both the channels are sensitive to the $U_{e4}U_{\mu 4}$ and $U_{e4}U_{\tau 4}$ which are combinations of mixing angles and our Neutrino Factory setup can constrain the allowed region of the neutrino oscillation parameters suggested by the LSND data much more strongly than the present data including MiniBooNE.

In the section 4.5, we have discussed the discovery potential to distinguish a four-family model from the three-family one. The discovery potential using the golden and the silver channels depends on the values of the θ_{24} and θ_{34} and we can hardly distinguish a four-family model from a three-family one in case of $\theta_{24} = \theta_{34} = 0$. On the other hand, the ν_μ disappearance and the discovery channels are useful to search for the a sterile neutrino because we can distinguish the four family scheme from three family one down to $\theta_{24} \simeq 7^\circ(7.5^\circ)$ and $\theta_{34} \simeq 13^\circ(15^\circ)$ which are half the values of the present bound at the 50 GeV (20 GeV) Neutrino Factory for any value of $\theta_{13}(3f) = \theta_{13}(4f)$ and θ_{14}.

In the section 4.6, we have discussed the dependence of the sensitivities on the systematic errors. For the discovery channel, the sensitivity to θ_{34} varies depending on the values of the systematic errors and we have found that the discovery channel is more sensitive to θ_{34} than the ν_μ disappearance channel for $f_{\mu\mu} = 0.05$ and $\sigma_\alpha = 0.01$ in the case of

$f_{\mu\tau} = 0.1$ and $\sigma_\alpha = 0.01$, or $f_{\mu\tau} \leq 0.03$ and $\sigma_\alpha \leq 0.05$ at the 50 GeV Neutrino Factory (in the case of $f_{\mu\tau} \leq 0.03$ and $\sigma_\alpha \leq 0.05$ at the 20 GeV Neutrino Factory).

In the section 4.7, we have discussed a CP violation by the CP-violating phase δ_3 which is not included in a three family model. We have defined δ_3 discovery potential and we have found that, combining the data from the ν_μ disappearance and the discovery channels, a non-vanishing δ_3 can be measured for values of θ_{34} as small as $\sin^2 2\theta_{34} = 0.06(\theta_{34} = 7^\circ)$ for $\bar{\theta}_{24} = 5^\circ$ and $\sin^2 2\theta_{34} = 0.10(\theta_{34} = 9^\circ)$ for $\bar{\theta}_{24} = 3^\circ$. For $\sin^2 2\theta_{34} \geq 0.4(\theta_{34} \geq 20^\circ)$, roughly 80% (60%) of CP-coverage is achieved for $\bar{\theta}_{24} = 5^\circ(3^\circ)$.

We conclude that a Neutrino Factory where we can use the four channels, golden, the silver, the discovery and the ν_μ disappearance channels, is powerful to search a sterile neutrino.

Appendix A

Analytic formula of oscillation probabilities in matter

In this appendix, we derive analytic formulae of flavor transition probabilities for long baseline neutrino oscillation experiments using KTY formula [52, 53, 152].

The evolution equation of four family neutrinos in matter is described as follows:

$$i\frac{d}{dt}\begin{pmatrix}\nu_e\\ \nu_\mu\\ \nu_\tau\\ \nu_s\end{pmatrix} = \left[U\mathcal{E}U^{-1}+\mathcal{A}(t)\right]\begin{pmatrix}\nu_e\\ \nu_\mu\\ \nu_\tau\\ \nu_s\end{pmatrix}, \tag{A.1}$$

where

$$\mathcal{A}(t) = \sqrt{2}G_F\mathrm{diag}(n_e(t)-\frac{n_n(t)}{2},-\frac{n_n(t)}{2},-\frac{n_n(t)}{2},0)$$

is the potential by the interaction with matter, G_F is the Fermi constant, $n_e(t)$ is the electron density in matter and n_n(t) is the neutron density in matter. Because sterile neutrinos do not interact with matter, the fourth elements of the potential $\mathcal{A}(t)$ are zeros. The effective Hamiltonian $U\mathcal{E}U^{-1}+\mathcal{A}(t)$ can be diagonalized using a unitary matrix $\tilde{U}(t)$:

$$\tilde{U}(t)\tilde{\mathcal{E}}(t)\tilde{U}^{-1}(t) = U\mathcal{E}U^{-1}+\mathcal{A}(t), \tag{A.2}$$

where

$$\tilde{\mathcal{E}}(t) = \mathrm{diag}(\ \tilde{E}_1(t),\quad \tilde{E}_2(t),\quad \tilde{E}_3(t)\ ) \tag{A.3}$$

and $\tilde{E}_{1,2,3}(t)$ is the eigenvalue of $U\mathcal{E}U^{-1}+\mathcal{A}(t)$. Using eq. (2.24), we can derive the transition probabilities of neutrino flavors in matter:

$$\begin{aligned} P(\nu_\alpha\to\nu_\beta) &= \left|\sum_{j,k}\tilde{U}_{\alpha j}\exp\left(-i\tilde{E}_{ij}L\right)\tilde{U}^*_{\beta k}\right|^2 \\ &= \delta_{\alpha\beta}-4\sum_{j>k}\mathrm{Re}\left[\tilde{X}_i^{\alpha\beta}\tilde{X}_j^{\alpha\beta *}\right]\sin^2\left(\frac{\tilde{E}_{ij}}{2}L\right) \\ &\quad -2\sum_{j>k}\mathrm{Im}\left[\tilde{X}_i^{\alpha\beta}\tilde{X}_j^{\alpha\beta *}\right]\sin\left(\tilde{E}_{ij}L\right), \end{aligned} \tag{A.4}$$

where $\tilde{X}_i^{\alpha\beta} = \tilde{U}_{\alpha i}\tilde{U}^*_{\beta i}$ $(i = 1, 2, 3, 4;\ \alpha, \beta = e, \mu, \tau, s)$, $\tilde{E}_{ij} = \tilde{E}_i - \tilde{E}_j$ and we assume that the electron density n_e and the neutron density n_n are constants.

We will obtain the following relations from eq.(A.2) and unitarity of $\tilde{U}_{\alpha i}$:

$$\begin{pmatrix} 1 & 1 & 1 & 1 \\ \tilde{E}_1 & \tilde{E}_2 & \tilde{E}_3 & \tilde{E}_4 \\ \tilde{E}_1^2 & \tilde{E}_2^2 & \tilde{E}_3^2 & \tilde{E}_4^2 \\ \tilde{E}_1^3 & \tilde{E}_2^3 & \tilde{E}_3^3 & \tilde{E}_4^3 \end{pmatrix} \begin{pmatrix} \tilde{X}_1^{\alpha\beta} \\ \tilde{X}_2^{\alpha\beta} \\ \tilde{X}_3^{\alpha\beta} \\ \tilde{X}_4^{\alpha\beta} \end{pmatrix} = \begin{pmatrix} \delta_{\alpha\beta} \\ U\mathcal{E}U^{-1} + \mathcal{A}(t) \\ (U\mathcal{E}U^{-1} + \mathcal{A}(t))^2 \\ (U\mathcal{E}U^{-1} + \mathcal{A}(t))^3 \end{pmatrix}. \tag{A.5}$$

We can then derive the following equations of $\tilde{X}_i^{\alpha\beta}$ from eq.(A.5):

$$\begin{pmatrix} \tilde{X}_1^{\alpha\beta} \\ \tilde{X}_2^{\alpha\beta} \\ \tilde{X}_3^{\alpha\beta} \\ \tilde{X}_4^{\alpha\beta} \end{pmatrix} = V \begin{pmatrix} \delta_{\alpha\beta} \\ (U\mathcal{E}U^{-1} + \mathcal{A}(t)) \\ (U\mathcal{E}U^{-1} + \mathcal{A}(t))^2 \\ (U\mathcal{E}U^{-1} + \mathcal{A}(t))^3 \end{pmatrix} \tag{A.6}$$

where

$$V = \begin{pmatrix} \frac{1}{\Delta\tilde{E}_{21}\Delta\tilde{E}_{31}\Delta\tilde{E}_{41}} \left(\tilde{E}_2\tilde{E}_3\tilde{E}_4,\ -(\tilde{E}_3\tilde{E}_4 + \tilde{E}_2\tilde{E}_4 + \tilde{E}_2\tilde{E}_3),\ \tilde{E}_2 + \tilde{E}_3 + \tilde{E}_4,\ -1\right) \\ \frac{-1}{\Delta\tilde{E}_{21}\Delta\tilde{E}_{32}\Delta\tilde{E}_{42}} \left(\tilde{E}_1\tilde{E}_3\tilde{E}_4,\ -(\tilde{E}_3\tilde{E}_4 + \tilde{E}_1\tilde{E}_4 + \tilde{E}_1\tilde{E}_3),\ \tilde{E}_1 + \tilde{E}_3 + \tilde{E}_4,\ -1\right) \\ \frac{1}{\Delta\tilde{E}_{31}\Delta\tilde{E}_{32}\Delta\tilde{E}_{43}} \left(\tilde{E}_1\tilde{E}_2\tilde{E}_4,\ -(\tilde{E}_2\tilde{E}_4 + \tilde{E}_1\tilde{E}_4 + \tilde{E}_1\tilde{E}_2),\ \tilde{E}_1 + \tilde{E}_2 + \tilde{E}_4,\ -1\right) \\ \frac{-1}{\Delta\tilde{E}_{41}\Delta\tilde{E}_{42}\Delta\tilde{E}_{43}} \left(\tilde{E}_1\tilde{E}_2\tilde{E}_3,\ -(\tilde{E}_2\tilde{E}_3 + \tilde{E}_1\tilde{E}_3 + \tilde{E}_1\tilde{E}_2),\ \tilde{E}_1 + \tilde{E}_2 + \tilde{E}_3,\ -1\right) \end{pmatrix}. \tag{A.7}$$

Considering the present constraints from [51] in the standard and sterile small parameters, we see that $\theta_{13},\ \theta_{14}$ and θ_{24} cannot be much larger than 10° while the third active-sterile mixing angle, θ_{34}, can be as large as $\theta_{34} \sim 35^\circ$. Notice also that the present constraint on the deviation of θ_{23} from the maximal mixing, $\delta\theta_{23} \equiv \theta_{23} - \pi/4$ is of the same order as those on $\theta_{13},\ \theta_{14}$ and θ_{24}. On the other hand, the solar and atmospheric mass differences, $\Delta m^2_{21},\ \Delta m^2_{31} \approx \Delta m^2_{32}$, are much smaller than $\Delta m^2_{41} \approx \Delta m^2_{42} \approx \Delta m^2_{43}$. In what follows, therefore, we expand all the quantities in power of a small parameter ϵ, and keep terms of cubic order in ϵ, where the small parameter is defined by

$$\begin{aligned} \epsilon &\equiv \theta_{34} \sim \sqrt{\theta_{13}} \sim \sqrt{\theta_{14}} \sim \sqrt{\theta_{24}} \sim \sqrt{\delta\theta_{23}} \lesssim 4 \times 10^{-1}, \\ \eta_2 &\equiv \Delta m^2_{21}/\Delta m^2_{41} \lesssim 10^{-4}, \\ \eta_3 &\equiv \Delta m^2_{31}/\Delta m^2_{41} \lesssim 10^{-3}, \\ \eta_{e(n)} &\equiv A_{e(n)}/\Delta E_{41} \lesssim 10^{-3}. \end{aligned}$$

Up to third order in ϵ in the expansion in the probabilities we can neglect $\eta_{e,n,2,3}$ and, then, eq.(A.6) which has the four components will reduce to a equation which has three components because of decoupling of ν_e as we discussed in the section 4.1. Although this can be a rather rough approximation, as we have seen before, it is very useful in order to understand the different physics potential of the various oscillation channels. Thus we have the following flavor transition probabilities to third order in ϵ:

$$
\begin{aligned}
P_{ee} &\sim 1 + O\left(\epsilon^4\right), \\
P_{e\mu} &\sim P_{e\tau} \sim P_{es} \sim O\left(\epsilon^4\right), \\
P_{\mu\mu} &= 1 - \sin^2 \frac{\Delta_{31} L}{2} - 2\left(A_n L\right) s_{24}\, s_{34} \cos\delta_3 \sin\Delta_{31} L + O\left(\epsilon^4\right) \ , \\
P_{\mu\tau} &= \left(1 - s_{34}^2\right) \sin^2 \frac{\Delta_{31} L}{2} + \left\{ s_{24}\, s_{34} \sin\delta_3 + 2\left(A_n L\right) s_{24}\, s_{34} \cos\delta_3 \right\} \sin\Delta_{31} L \\
&\quad + O\left(\epsilon^4\right), \\
P_{\mu s} &= s_{34}^2 \sin^2 \frac{\Delta_{31} L}{2} - s_{24}\, s_{34} \sin\delta_3 \sin\Delta_{31} L + O\left(\epsilon^4\right) \ .
\end{aligned}
$$

Furthermore, as we discussed in the section 4.4.2, the following transition probability

of the golden channel in matter to fourth order in ϵ is useful:

$$
\begin{aligned}
P_{e\mu} \;=\; & \frac{(\Delta m^2_{31})^4}{\Delta\tilde{E}^2_{21}\Delta\tilde{E}_{31}\Delta\tilde{E}_{32}}\Bigg[x s^2_{13}s^2_{23}\Big\{(s^2_{34}-1)(1+\frac{s^2_{34}x}{2}+\sqrt{1+\frac{s^4_{34}x^2}{4}}) \\
& \quad -2s^2_{34}+4\Big\} \\
& \quad +\frac{1}{2}\cos\delta_2 s_{13}s_{14}s_{23}\sin 2\theta_{23}\sin 2\theta_{34}x\Big\{\frac{3s^2_{34}x}{4}+\frac{\sqrt{1+s_3 4^4x^2/4}}{2}-x-\frac{1}{2}\Big\} \\
& +\frac{1}{16}s^2_{14}\sin^2 2\theta_{23}\sin^2 2\theta_{34}x^2\Bigg]\sin^2\left(\frac{\Delta m^2_{31}(1+s^2_{34}x/2-\sqrt{1+s^4_{34}x^2/4}-2x)}{8E}L\right) \\
& -\frac{(\Delta m^2_{31})^4}{\Delta\tilde{E}_{21}\Delta\tilde{E}^2_{31}\Delta\tilde{E}_{32}}\Bigg[x s^2_{13}s^2_{23}\Big\{(s^2_{34}-2)(1+\frac{s^2_{34}x}{2}-\sqrt{1+\frac{s^4_{34}x^2}{4}}) \\
& \quad -2s^2_{34}+4\Big\} \\
& \quad +\frac{1}{2}\cos\delta_2 s_{13}s_{14}s_{23}\sin 2\theta_{23}\sin 2\theta_{34}x\Big\{\frac{3s^2_{34}x}{4}-\frac{\sqrt{1+s_3 4^4x^2/4}}{2}-x-\frac{1}{2}\Big\} \\
& +\frac{1}{16}s^2_{14}\sin^2 2\theta_{23}\sin^2 2\theta_{34}x^2\Bigg]\sin^2\left(\frac{\Delta m^2_{31}(1+s^2_{34}x/2+\sqrt{1+s^4_{34}x^2/4}-2x)}{8E}L\right) \\
& +\frac{(\Delta m^2_{31})^4}{\Delta\tilde{E}^2_{21}\Delta\tilde{E}_{31}\Delta\tilde{E}_{32}}\Bigg[\frac{1}{2}\cos\delta_2 s_{13}s_{14}s_{23}\sin 2\theta_{23}\sin 2\theta_{34}x\Big\{\frac{s^2_{34}x}{2}-1\Big\} \\
& +\frac{1}{16}s^2_{14}\sin^2 2\theta_{23}\sin^2 2\theta_{34}x^2\Bigg]\sin^2\left(\frac{\Delta m^2_{31}\sqrt{1+s^4_{34}x^2/4})}{4E}L\right) \\
& -\frac{(\Delta m^2_{31})^4}{\Delta\tilde{E}_{21}\Delta\tilde{E}^2_{31}\Delta\tilde{E}_{32}}\Bigg[\frac{1}{4}\sin\delta_2 s_{13}s_{14}s_{23}\sin 2\theta_{23}\sin 2\theta_{34}x\Big\{\frac{1}{2}+\frac{s^2_{34}x}{4} \\
& \quad +\frac{\sqrt{1+s^4_{34}x^2/4}}{2}-x\Big\}\Bigg]\sin\left(\frac{\Delta m^2_{31}(1+s^2_{34}x/2+\sqrt{1+s^4_{34}x^2/4}-2x)}{4E}L\right) \\
& +\frac{(\Delta m^2_{31})^4}{\Delta\tilde{E}^2_{21}\Delta\tilde{E}_{31}\Delta\tilde{E}_{32}}\Bigg[\frac{1}{4}\sin\delta_2 s_{13}s_{14}s_{23}\sin 2\theta_{23}\sin 2\theta_{34}x\Big\{\frac{1}{2}+\frac{s^2_{34}x}{4} \\
& \quad +\frac{\sqrt{1+s^4_{34}x^2/4}}{2}-x\Big\}\Bigg]\sin\left(\frac{\Delta m^2_{31}(1+s^2_{34}x/2-\sqrt{1+s^4_{34}x^2/4}-2x)}{4E}L\right)\,,
\end{aligned}
\tag{A.8}
$$

where

$$x = \frac{2\sqrt{2}G_F n_e E}{\Delta m^2_{31}} \tag{A.9}$$

$$\Delta\tilde{E}_{21} = \frac{\Delta m^2_{31}}{2}(1+\frac{s^2_{34}x}{2}-\sqrt{1+s^4_{34}x^2/4}-2x) \tag{A.10}$$

$$\Delta\tilde{E}_{31} = \frac{\Delta m^2_{31}}{2}(1+\frac{s^2_{34}x}{2}+\sqrt{1+s^4_{34}x^2/4}-2x) \tag{A.11}$$

$$\Delta\tilde{E}_{32} = \Delta m^2_{31}\sqrt{1+s^4_{34}x^2/4}\,. \tag{A.12}$$

Bibliography

[1] C. Amsler *et al.* [Particle Data Group], Phys. Lett. B **667** (2008) 1.

[2] LEP Collaborations (ALEPH, DELPHI, OPAL, L3) *et al.*, Phys. Rept. **427** (2006) 257 [arXiv:hep-ex/0509008].

[3] T. Schwetz, M. Tortola and J. W. F. Valle, New J. Phys. **10** (2008) 113011 [arXiv:0808.2016 [hep-ph]].

[4] G. L. Fogli, E. Lisi, A. Marrone, A. Palazzo and A. M. Rotunno, arXiv:0809.2936 [hep-ph].

[5] M. Apollonio *et al.* [CHOOZ Collaboration], Phys. Lett. B **466** (1999) 415 [arXiv:hep-ex/9907037].

[6] M. Apollonio *et al.* [CHOOZ Collaboration], Eur. Phys. J. C **27**, 331 (2003) [arXiv:hep-ex/0301017].

[7] F. Boehm *et al.*, Phys. Rev. D **64** (2001) 112001 [arXiv:hep-ex/0107009].

[8] G. L. Fogli, E. Lisi, A. Marrone, A. Palazzo and A. M. Rotunno, Phys. Rev. Lett. **101** (2008) 141801 [arXiv:0806.2649 [hep-ph]].

[9] H. L. Ge, C. Giunti and Q. Y. Liu, arXiv:0810.5443 [hep-ph].

[10] G. L. Fogli, E. Lisi, A. Marrone, A. Palazzo and A. M. Rotunno, arXiv:0905.3549 [hep-ph].

[11] Y. Itow *et al.* [The T2K Collaboration], arXiv:hep-ex/0106019.

[12] D. S. Ayres *et al.* [NOvA Collaboration], arXiv:hep-ex/0503053.

[13] M. Ishitsuka, T. Kajita, H. Minakata and H. Nunokawa, Phys. Rev. D **72** (2005) 033003 [arXiv:hep-ph/0504026].

[14] K. Hagiwara, N. Okamura and K. i. Senda, Phys. Lett. B **637** (2006) 266 [Erratum-ibid. B **641** (2006) 486] [arXiv:hep-ph/0504061].

[15] M. V. Diwan *et al.*, Phys. Rev. D **68** (2003) 012002 [arXiv:hep-ph/0303081].

[16] S. Geer, Phys. Rev. D **57** (1998) 6989 [Erratum-ibid. D **59** (1999) 039903] [arXiv:hep-ph/9712290].

[17] P. Zucchelli, Phys. Lett. B **532** (2002) 166.

[18] Belle experiment, `http://belle.kek.jp/`.

[19] Babar experiment, `http://www-public.slac.stanford.edu/babar/`.

[20] Y. Grossman, Phys. Lett. B **359** (1995) 141 [arXiv:hep-ph/9507344].

[21] M. M. Guzzo, A. Masiero and S. T. Petcov, Phys. Lett. B **260** (1991) 154.

[22] E. Roulet, Phys. Rev. D **44** (1991) 935.

[23] B. Pontecorvo, Sov. Phys. JETP **26**, 984 (1968) [Zh. Eksp. Teor. Fiz. **53**, 1717 (1967)].

[24] S. Antusch, C. Biggio, E. Fernandez-Martinez, M. B. Gavela and J. Lopez-Pavon, JHEP **0610** (2006) 084 [arXiv:hep-ph/0607020].

[25] A. Abada, C. Biggio, F. Bonnet, M. B. Gavela and T. Hambye, JHEP **0712** (2007) 061 [arXiv:0707.4058 [hep-ph]].

[26] The ISS Physics Working Group, arXiv:0710.4947 [hep-ph].

[27] C. Athanassopoulos *et al.* [LSND Collaboration], Phys. Rev. Lett. **77**, 3082 (1996) [arXiv:nucl-ex/9605003].

[28] C. Athanassopoulos *et al.* [LSND Collaboration], Phys. Rev. Lett. **81** (1998) 1774 [arXiv:nucl-ex/9709006].

[29] A. Aguilar *et al.* [LSND Collaboration], Phys. Rev. D **64** (2001) 112007 [arXiv:hep-ex/0104049].

[30] A. A. Aguilar-Arevalo *et al.* [The MiniBooNE Collaboration], Phys. Rev. Lett. **98** (2007) 231801 [arXiv:0704.1500 [hep-ex]].

[31] A. A. Aguilar-Arevalo *et al.* [MiniBooNE Collaboration], Phys. Rev. Lett. **102**, 101802 (2009) [arXiv:0812.2243 [hep-ex]].

[32] J. Jenkins and T. Goldman, arXiv:0906.0984 [hep-ph].

[33] J. T. Goldman, G. J. . Stephenson and B. H. J. McKellar, Phys. Rev. D **75**, 091301 (2007) [arXiv:nucl-th/0703023].

[34] T. Katori, V. A. Kostelecky and R. Tayloe, Phys. Rev. D **74**, 105009 (2006) [arXiv:hep-ph/0606154].

[35] H. Pas, S. Pakvasa and T. J. Weiler, Phys. Rev. D **72**, 095017 (2005) [arXiv:hep-ph/0504096].

[36] V. Barger, D. Marfatia and K. Whisnant, Phys. Lett. B **576**, 303 (2003) [arXiv:hep-ph/0308299].

[37] C. Giunti and M. Laveder, Phys. Rev. D **80**, 013005 (2009) [arXiv:0902.1992 [hep-ph]].

[38] M. Sorel, J. M. Conrad and M. Shaevitz, Phys. Rev. D **70** (2004) 073004 [arXiv:hep-ph/0305255].

[39] M. Maltoni and T. Schwetz, Phys. Rev. D **76**, 093005 (2007) [arXiv:0705.0107 [hep-ph]].

[40] A. A. Aguilar-Arevalo *et al.* [MiniBooNE Collaboration], arXiv:0904.1958 [hep-ex].

[41] M. H. Shaevitz, The eleventh international conference on Topics in Astroparticle and Underground Physics (TAUP2009), Italy, on July 1st-5th, 2009. http://taup2009.lngs.infn.it/

[42] V. Barger, D. Marfatia and K. Whisnant, Phys. Rev. D **73**, 013005 (2006) [arXiv:hep-ph/0509163].

[43] S. Palomares-Ruiz, S. Pascoli and T. Schwetz, JHEP **0509** (2005) 048 [arXiv:hep-ph/0505216].

[44] A. de Gouvea and Y. Grossman, Phys. Rev. D **74**, 093008 (2006) [arXiv:hep-ph/0602237].

[45] T. Schwetz, JHEP **0802**, 011 (2008) [arXiv:0710.2985 [hep-ph]].

[46] A. E. Nelson and J. Walsh, Phys. Rev. D **77**, 033001 (2008) [arXiv:0711.1363 [hep-ph]].

[47] A. de Gouvea, J. Jenkins and N. Vasudevan, Phys. Rev. D **75**, 013003 (2007) [arXiv:hep-ph/0608147].

[48]

[48] G. C. McLaughlin, J. M. Fetter, A. B. Balantekin and G. M. Fuller, Phys. Rev. C **59**, 2873 (1999) [arXiv:astro-ph/9902106]; D. O. Caldwell, G. M. Fuller and Y. Z. Qian, Phys. Rev. D **61**, 123005 (2000) [arXiv:astro-ph/9910175]; J. Fetter, G. C. McLaughlin, A. B. Balantekin and G. M. Fuller, Astropart. Phys. **18**, 433 (2003) [arXiv:hep-ph/0205029].

[49] E. K. Akhmedov, V. A. Rubakov and A. Y. Smirnov, Phys. Rev. Lett. **81**, 1359 (1998) [arXiv:hep-ph/9803255].

[50] A. Kusenko, arXiv:0906.2968 [hep-ph].

[51] A. Donini, M. Maltoni, D. Meloni, P. Migliozzi and F. Terranova, JHEP **0712**, 013 (2007) [arXiv:0704.0388 [hep-ph]].

[52] K. Kimura, A. Takamura and H. Yokomakura, Phys. Lett. B **537**, 86 (2002) [arXiv:hep-ph/0203099].

[53] K. Kimura, A. Takamura and H. Yokomakura, Phys. Rev. D **66**, 073005 (2002) [arXiv:hep-ph/0205295].

[54] A. Donini and D. Meloni, Eur. Phys. J. C **22** (2001) 179 [arXiv:hep-ph/0105089].

[55] A. Donini, M. Lusignoli and D. Meloni, Nucl. Phys. B **624** (2002) 405 [arXiv:hep-ph/0107231].

[56] T. Abe *et al.* [ISS Detector Working Group], arXiv:0712.4129 [physics.ins-det].

[57] A. Cervera, A. Donini, M. B. Gavela, J. J. Gomez Cadenas, P. Hernandez, O. Mena and S. Rigolin, Nucl. Phys. B **579**, 17 (2000) [Erratum-ibid. B **593**, 731 (2001)] [arXiv:hep-ph/0002108].

[58] A. Donini, D. Meloni and P. Migliozzi, Nucl. Phys. B **646** (2002) 321 [arXiv:hep-ph/0206034].

[59] A. Donini, K. i. Fuki, J. Lopez-Pavon, D. Meloni and O. Yasuda, JHEP **08** (2009) 041 , arXiv:0812.3703 [hep-ph].

[60] P. Minkowski Phys. Lett. B **67**, 421 (1977); T. Yanagida, in *Proceedings of the Workshop on Unified Theory and the Baryon Number of the Universe*, edited by O. Sawada and A. Sugamoto (KEK, Tsukuba, 1979), p95; M. Gell-Mann, P. Ramond, and R. Slansky, in *Supergravity*, edited by P. van Nieuwenhuizen and D. Freedman (North Holland, Amsterdam, 1979), p315.

[61] A. Zee, Phys. Lett. B **93**, 389 (1980) [Erratum-ibid. B **95**, 461 (1980)].

[62] Z. Maki, M. Nakagawa and S. Sakata, Prog. Theor. Phys. **28**, 870 (1962).

[63] T. Araki *et al.* [KamLAND Collaboration], Phys. Rev. Lett. **94**, 081801 (2005) [arXiv:hep-ex/0406035].

[64] J. N. Bahcall, A. M. Serenelli and S. Basu, Astrophys. J. **621**, L85 (2005) [arXiv:astro-ph/0412440].

[65] A. Strumia and F. Vissani, arXiv:hep-ph/0606054.

[66] R. Davis, Phys. Rev. Lett. 12 (1964) 302; B. T. Cleveland *et al.*, Astrophys. J. **496**, 505 (1998); see also ref. [4] in A. Strumia and F. Vissani, arXiv:hep-ph/0606054.

[67] P. Anselmann *et al.* [GALLEX Collaboration.], Phys. Lett. B **342**, 440 (1995); M. Altmann *et al.* [GNO COLLABORATION Collaboration], Phys. Lett. B **616**, 174 (2005) [arXiv:hep-ex/0504037]; see also ref. [8] in A. Strumia and F. Vissani, arXiv:hep-ph/0606054.

[68] J. Hosaka *et al.* [Super-Kamkiokande Collaboration], Phys. Rev. D **73**, 112001 (2006) [arXiv:hep-ex/0508053]; see also ref. [9] in A. Strumia and F. Vissani, arXiv:hep-ph/0606054.

[69] Q. R. Ahmad *et al.* [SNO Collaboration], Phys. Rev. Lett. **87**, 071301 (2001) [arXiv:nucl-ex/0106015]; B. Aharmim *et al.* [SNO Collaboration], Phys. Rev. C **72**, 055502 (2005) [arXiv:nucl-ex/0502021]; see also ref. [10] in A. Strumia and F. Vissani, arXiv:hep-ph/0606054.

[70] J. F. Amsbaugh *et al.*, Nucl. Instrum. Meth. A **579**, 1054 (2007) [arXiv:0705.3665 [nucl-ex]].

[71] C. Arpesella *et al.* [Borexino Collaboration], Phys. Lett. B **658**, 101 (2008) [arXiv:0708.2251 [astro-ph]]; C. Arpesella *et al.* [The Borexino Collaboration], Phys. Rev. Lett. **101**, 091302 (2008) [arXiv:0805.3843 [astro-ph]].

[72] K. Eguchi *et al.* [KamLAND Collaboration], Phys. Rev. Lett. **90**, 021802 (2003) [arXiv:hep-ex/0212021]; S. Abe *et al.* [KamLAND Collaboration], Phys. Rev. Lett. **100**, 221803 (2008) [arXiv:0801.4589 [hep-ex]]; see also ref. [10] in A. Strumia and F. Vissani, arXiv:hep-ph/0606054.

[73] J. Hosaka *et al.* [Super-Kamiokande Collaboration], Phys. Rev. D **74**, 032002 (2006) [arXiv:hep-ex/0604011].

[74] M. Maltoni and T. Schwetz, arXiv:0812.3161 [hep-ph].

[75] E. D. Church, K. Eitel, G. B. Mills and M. Steidl, Phys. Rev. D **66**, 013001 (2002) [arXiv:hep-ex/0203023].

[76] A. De Rujula, M. B. Gavela and P. Hernandez, Nucl. Phys. B **547** (1999) 21 [arXiv:hep-ph/9811390].

[77] J. N. Abdurashitov *et al.* [SAGE Collaboration], Phys. Rev. C **60** (1999) 055801 [arXiv:astro-ph/9907113].

[78] W. Hampel *et al.* [GALLEX Collaboration], Phys. Lett. B **447** (1999) 127.

[79] S. Fukuda *et al.* [Super-Kamiokande Collaboration], Phys. Rev. Lett. **86** (2001) 5651 [arXiv:hep-ex/0103032].

[80] J. P. Cravens *et al.* [Super-Kamiokande Collaboration], Phys. Rev. D **78** (2008) 032002 [arXiv:0803.4312 [hep-ex]].

[81] S. N. Ahmed *et al.* [SNO Collaboration], Phys. Rev. Lett. **92** (2004) 181301 [arXiv:nucl-ex/0309004].

[82] B. Aharmim *et al.* [SNO Collaboration], Phys. Rev. Lett. **101** (2008) 111301 [arXiv:0806.0989 [nucl-ex]].

[83] Y. Fukuda *et al.* [Super-Kamiokande Collaboration], Phys. Rev. Lett. **81** (1998) 1562 [arXiv:hep-ex/9807003].

[84] M. Ambrosio *et al.* [MACRO Collaboration], Phys. Lett. B **517** (2001) 59 [arXiv:hep-ex/0106049].

[85] K. Eguchi *et al.* [KamLAND Collaboration], Phys. Rev. Lett. **90** (2003) 021802 [arXiv:hep-ex/0212021].

[86] M. H. Ahn *et al.* [K2K Collaboration], Phys. Rev. Lett. **90** (2003) 041801 [arXiv:hep-ex/0212007].

[87] E. Aliu *et al.* [K2K Collaboration], Phys. Rev. Lett. **94** (2005) 081802 [arXiv:hep-ex/0411038].

[88] D. G. Michael *et al.* [MINOS Collaboration], Phys. Rev. Lett. **97** (2006) 191801 [arXiv:hep-ex/0607088].

[89] P. Adamson *et al.* [MINOS Collaboration], Phys. Rev. Lett. **101** (2008) 131802 [arXiv:0806.2237 [hep-ex]].

[90] B. Pontecorvo, Sov. Phys. JETP **6** (1957) 429 [Zh. Eksp. Teor. Fiz. **33** (1957) 549].

[91] V. N. Gribov and B. Pontecorvo, Phys. Lett. B **28** (1969) 493.

[92] M. C. Gonzalez-Garcia and M. Maltoni, arXiv:0704.1800 [hep-ph].

[93] T. Ota and J. Sato, Phys. Lett. B **545**, 367 (2002) [arXiv:hep-ph/0202145].

[94] E. Fernandez-Martinez, M. B. Gavela, J. Lopez-Pavon and O. Yasuda, Phys. Lett. B **649** (2007) 427 [arXiv:hep-ph/0703098];

[95] G. Altarelli and D. Meloni, Nucl. Phys. B **809** (2009) 158 [arXiv:0809.1041 [hep-ph]].

[96] CNGS experiment, `http://proj-cngs.web.cern.ch/proj-cngs/`.

[97] J. Burguet-Castell *et al.*, Nucl. Phys. B **608** (2001) 301 [arXiv:hep-ph/0103258];

[98] H. Minakata and H. Nunokawa, JHEP **0110** (2001) 001 [arXiv:hep-ph/0108085];

[99] A. Donini, M. B. Gavela, P. Hernandez and S. Rigolin, Nucl. Phys. B **574** (2000) 23 [arXiv:hep-ph/9909254].

[100] A. Donini, M. B. Gavela, P. Hernandez and S. Rigolin, Nucl. Instrum. Meth. A **451** (2000) 58 [arXiv:hep-ph/9910516].

[101] A. Kalliomaki, J. Maalampi and M. Tanimoto, Phys. Lett. B **469** (1999) 179 [arXiv:hep-ph/9909301].

[102] A. Dighe and S. Ray, Phys. Rev. D **76**, 113001 (2007) [arXiv:0709.0383 [hep-ph]].

[103] A. Boyarsky, A. Neronov, O. Ruchayskiy and M. Shaposhnikov, Mon. Not. Roy. Astron. Soc. **370** (2006) 213 [arXiv:astro-ph/0512509].

[104] M. Maltoni, T. Schwetz, M. A. Tortola and J. W. F. Valle, New J. Phys. **6** (2004) 122 [arXiv:hep-ph/0405172v6].

[105] N. Okada and O. Yasuda, Int. J. Mod. Phys. A **12** (1997) 3669 [arXiv:hep-ph/9606411].

[106] S. M. Bilenky, C. Giunti and W. Grimus, Eur. Phys. J. C **1** (1998) 247 [arXiv:hep-ph/9607372].

[107] F. Dydak *et al.*, Phys. Lett. B **134** (1984) 281.

[108] Y. Declais *et al.*, Nucl. Phys. B **434** (1995) 503.

[109] G. Karagiorgi, A. Aguilar-Arevalo, J. M. Conrad, M. H. Shaevitz, K. Whisnant, M. Sorel and V. Barger, Phys. Rev. D **75**, 013011 (2007) [arXiv:hep-ph/0609177].

[110] S. M. Bilenky, C. Giunti, W. Grimus and T. Schwetz, Astropart. Phys. **11**, 413 (1999) [arXiv:hep-ph/9804421].

[111] R. Foot and R. R. Volkas, Phys. Rev. D **55**, 5147 (1997) [arXiv:hep-ph/9610229].

[112] M. Cirelli, G. Marandella, A. Strumia and F. Vissani, Nucl. Phys. B **708**, 215 (2005) [arXiv:hep-ph/0403158].

[113] A. De Rujula, M. Lusignoli, L. Maiani, S. T. Petcov and R. Petronzio, Nucl. Phys. B **168** (1980) 54.

[114] A. M. Dziewonski and D.L. Anderson, Phys. Earth Planet. Int. **25** (1981) 297.

[115] S. K. Agarwalla, S. Choubey and A. Raychaudhuri, Nucl. Phys. B **771** (2007) 1 [arXiv:hep-ph/0610333].

[116] A. Bueno, M. Campanelli and A. Rubbia, Nucl. Phys. B **589** (2000) 577 [arXiv:hep-ph/0005007].

[117] M. Campanelli, A. Bueno and A. Rubbia, Nucl. Instrum. Meth. A **451** (2000) 176.

[118] A. De Rujula, M. B. Gavela and P. Hernandez, Nucl. Phys. B **547** (1999) 21 [arXiv:hep-ph/9811390].

[119] A. Broncano and O. Mena, Eur. Phys. J. C **29** (2003) 197 [arXiv:hep-ph/0203052].

[120] B. Autin, A. Blondel and J. R. Ellis, "Prospective study of muon storage rings at CERN,"

[121] P. Gruber *et al.*, "The study of a European Neutrino Factory complex."

[122] D. Finley and N. Holtkamp, Nucl. Instrum. Meth. A **472**, 388 (2000).

[123] S. Ozaki *et al.*, BNL-52623, "Feasibility study 2 of a muon based neutrino source."

[124] M. M. Alsharoa *et al.* [Muon Collider/Neutrino Factory Collaboration], Phys. Rev. ST Accel. Beams **6**, 081001 (2003) [arXiv:hep-ex/0207031].

[125] M. S. Zisman, Nucl. Instrum. Meth. A **503**, 384 (2003).

[126] Y. Kuno, Y. Mori, S. Machida, T. Yokoi, Y. Iwashita, J. Sato and O. Yasuda, "A feasibility study of a neutrino factory in Japan," `http://www.slac.stanford.edu/spires/find/hep/www?irn=4623622`.

[127] M. S. Zisman, J. Phys. Conf. Ser. **110** (2008) 112006.

[128] P. Huber and W. Winter, Phys. Rev. D **68** (2003) 037301 [arXiv:hep-ph/0301257].

[129] J. Kopp, T. Ota and W. Winter, Phys. Rev. D **78** (2008) 053007 [arXiv:0804.2261 [hep-ph]].

[130] P. Lipari, private communication.

[131] P. Lipari, M. Lusignoli and F. Sartogo, Phys. Rev. Lett. **74** (1995) 4384 [arXiv:hep-ph/9411341].

[132] A. Cervera-Villanueva, AIP Conf. Proc. **981** (2008) 178.

[133] A. Cervera, F. Dydak and J. Gomez Cadenas, Nucl. Instrum. Meth. A **451**, 123 (2000).

[134] D. Autiero *et al.*, Eur. Phys. J. C **33** (2004) 243 [arXiv:hep-ph/0305185].

[135] P. Huber, M. Lindner and W. Winter, Nucl. Phys. B **645** (2002) 3 [arXiv:hep-ph/0204352].

[136] G. L. Fogli and E. Lisi, Phys. Rev. D **54** (1996) 3667 [arXiv:hep-ph/9604415];

[137] V. Barger, D. Marfatia and K. Whisnant, Phys. Rev. D **65** (2002) 073023 [arXiv:hep-ph/0112119].

[138] A. Donini, E. Fernandez-Martinez, D. Meloni and S. Rigolin, Nucl. Phys. B **743** (2006) 41 [arXiv:hep-ph/0512038].

[139] P. Huber and T. Schwetz, Phys. Lett. B **669** (2008) 294 [arXiv:0805.2019 [hep-ph]].

[140] E. Ables *et al.* [MINOS Collaboration],

[141] P. Huber, M. Lindner, M. Rolinec and W. Winter, Phys. Rev. D **74** (2006) 073003 [arXiv:hep-ph/0606119].

[142] D. Indumathi [INO Collaboration], Pramana **63**, 1283 (2004).

[143] C. Fukushima *et al.*, Nucl. Instrum. Meth. A **592** (2008) 56.

[144] D. Meloni, Phys. Lett. B **664** (2008) 279 [arXiv:0802.0086 [hep-ph]].

[145] P. Migliozzi, private communication.

[146] L. Scotto Lavina, talk at the NuFact'08 Workshop, Valencia, `http://indico.ific.uv.es/indico/materialDisplay.py?contribId=132&sessionId=23&materialId=slides&confId=71`.

[147] K. Fuki, poster at the NuFact'08 Workshop, Valencia, `http://indico.ific.uv.es/indico/materialDisplay.py?contribId=166&sessionId=38&materialId=poster&confId=71`.

[148] D. Meloni, arXiv:0812.3555v1 [hep-ph].

D. Meloni, talk at the NOW'08 Workshop, Otranto,

[149] A. Donini, D. Meloni and S. Rigolin, JHEP **0406** (2004) 011 [arXiv:hep-ph/0312072].

[150] A. Laing and F. J. P. Soler, AIP Conf. Proc. **981** (2008) 166.

[151] Z. z. Xing and H. Zhang, Phys. Lett. B **618** (2005) 131 [arXiv:hep-ph/0503118].

[152] O. Yasuda, arXiv:0704.1531 [hep-ph].

[153] H. Zhang, Mod. Phys. Lett. A **22**, 1341 (2007) [arXiv:hep-ph/0606040].

[154] S. Goswami and T. Ota, Phys. Rev. D **78**, 033012 (2008) [arXiv:0802.1434 [hep-ph]].